Alma Mater Studiorum · University of Bologna

Department of Physics and Astronomy
Master Degree Programme in Astrophysics and Cosmology

Probing the Nature of FR0 Radio Galaxies: Compactness and jet extension

Master's thesis

Submitted by:
Leonardo Penna

Supervisor: **Prof. Myriam Gitti**
Co-supervisors: **Dr. Ranieri D. Baldi**
Dr. Marisa Brienza

Academic Year 2024/2025 Graduation Date: July 18, 2025

Abstract

Accreting supermassive black holes (SMBHs) are among the most energetic phenomena in the Universe, capable of profoundly impacting their surroundings, regulating the star formation of the host galaxies and influencing their evolution. These sources are referred to as Active Galactic Nuclei (AGN), and approximately 10% of them are classified as radio-loud (RL), a designation based on the presence of relativistic collimated jets.

Over the past decade, a new class of RLAGN in the local Universe ($z<0.1$) has emerged: the Fanaroff–Riley type 0 (FR 0) radio galaxies, which are the focus of this thesis. These sources are compact radio galaxies typically found in red massive early-type galaxies and display low-excitation signatures consistent with radiatively inefficient accretion flows. Their miniature-scale jets may play an important role in regulating star formation through jet-driven mechanical feedback on the scale of the host galaxy. However, the reason why FR0s lack large-scale jets, contrary to the classical FR I/FR II radio galaxies, is still unclear.

In this thesis I address this open question by analysing 32 FR 0s drawn from the FR0CAT catalogue compiled by Baldi et al. I investigate the origin of their nuclear features and the properties of the large-scale jetted emission (tens-hundreds of kpc) when present using complementary multi-frequency observations. The sample is divided into two groups: the first comprises five sources previously selected for showing large-scale emission in LOw Frequency Array (LOFAR) images at 0.144 GHz, which were re-observed with the C-configuration of the Very Large Array (VLA) at 3 GHz in order to study the spectral properties of their extended radio structures. The second group includes 27 FR 0s targeted with the A-configuration of the VLA at 1.4, 4.5, and 7.5 GHz to investigate their nuclear radio properties at high resolution. To complement these observations, additional public images from large-area surveys from 145 MHz to 1.4 GHz were incorporated.

These datasets provided additional frequency coverage and spatial information, enabling the construction of more complete spectral energy distributions for the sources.

The analysis reveals that most FR 0s are unresolved on sub-kiloparsec scales and dominated by an optically thick, self-absorbed core. Only about one-third show extended steep-spectrum emission of few kiloparsec. Even in these cases the total emission remains highly core dominated, tens of times higher than the FR Is, and is not related to any physical condition of the AGN or the environment. Only two sources show very steep radio spectra on scales of tens of kpc, possibly indicating the signature of past jet activity.

A possible young radio phase may explain the morphological compactness of only $\sim$10% of FR 0s, which could potentially be classified as Giga-Hertz Peaked Spectrum sources, genuine young radio galaxies. However, flux variability observed on timescales of years complicates a reliable determination of this fraction. A lower accretion rate onto the SMBHs compared to that observed in ordinary FR I radio galaxies may also explain their limited capability of launching extended jets. We examined the accretion-ejection mechanisms by studying the link between the radio core luminosity and the [O III] line luminosity, used as proxy of the AGN bolometric power and the jet brightness distribution, as proxy of the jet bulk speed. Our results confirm that FR 0s are consistent with the low-luminosity tail of the FR I population, with a mildly-relativistic jet speed.

Based on our results, we conclude that FR 0s constitute the low-power tail of the local radio galaxy population. Their compact jets are not the result of either young or recurrent radio activity, but rather of a combination of several factors (some not directly observable at present), including BH spin and magnetic field strength. These parameters play a significant role in setting the jet production efficiency, thus creating a broad population of low-power radio galaxies complementary to the most powerful FR Is.

Contents

1

Introduction

1.1 Active Galactic Nuclei

Amidst the continuously expanding, seemingly infinite and mostly out of reach Universe, lie some of the most outstanding and extreme objects ever discovered. Although most galaxies appear relatively quiescent, it is common knowledge that nearly every massive galaxy hosts a supermassive black hole (SMBH) with a mass $10^6 - 10^{10}$ times the mass of our Sun[1], according to a NASA Hubble census (see e.g. NASA Science 2022). Most of these SMBHs are quiescent, but about 1-10% actively accrete surrounding matter and release enormous amounts of energy. For this reason, a galaxy with an accreting SMBH at its center is named *Active Galactic Nucleus (AGN)*.

This thesis mostly discusses the emission from AGN in the radio band, which is just a portion of the whole electromagnetic spectrum on more than twenty orders of magnitude in frequency (see Figure 1.1); with an energy output that can reach up to 10^{48} erg s^{-1} for the most distant and powerful quasars, whose emission can outshine the host galaxy by several orders of magnitude in the optical band (Padovani et al. 2017).

The first observational evidence of AGN dates back to the work of Seyfert (1943), who identified spiral galaxies that host a compact, quasar-like nucleus with prominent high-excitation emission lines in their optical spectra. However, his work received the deserved recognition only a decade later, when Baade and Minkowski (1954) spotted the striking similarity of the strong emission lines between the optical counterpart of Cygnus A[2] and the forgotten Seyfert galaxies. This connection helped revive interest in these peculiar objects and further analysis on their spectra allowed Woltjer (1959) to correctly estimate the nuclear emitting region around 100 pc. The final piece regarding the backbone of the Seyfert galaxies was advanced by Khachikian and Weedman (1974), who divided them into *Type 1 Seyferts*, which exhibit both narrow and broad emission lines, and *Type 2 Seyferts* which feature only narrow lines.

A major step forward was made in 1963, when Schmidt (1963) expanded the AGN class by classifying a star-looking object, 3C 273[3], as a quasi-stellar object (QSO, later simply quasar) in sight of the different processes that should originate its powerful energy output, with respect to stellar objects. This is an important distinction that we are going

[1]The mass of the Sun is $M_\odot = 1.9891 \times 10^{30}$ kg.
[2]Powerful radio AGN in the local universe at redshift ≈ 0.056.
[3]Redshift of the source is z=0.158.

to briefly demonstrate in the following Section 1.1.1, which concludes this brief historical (optical) overview.

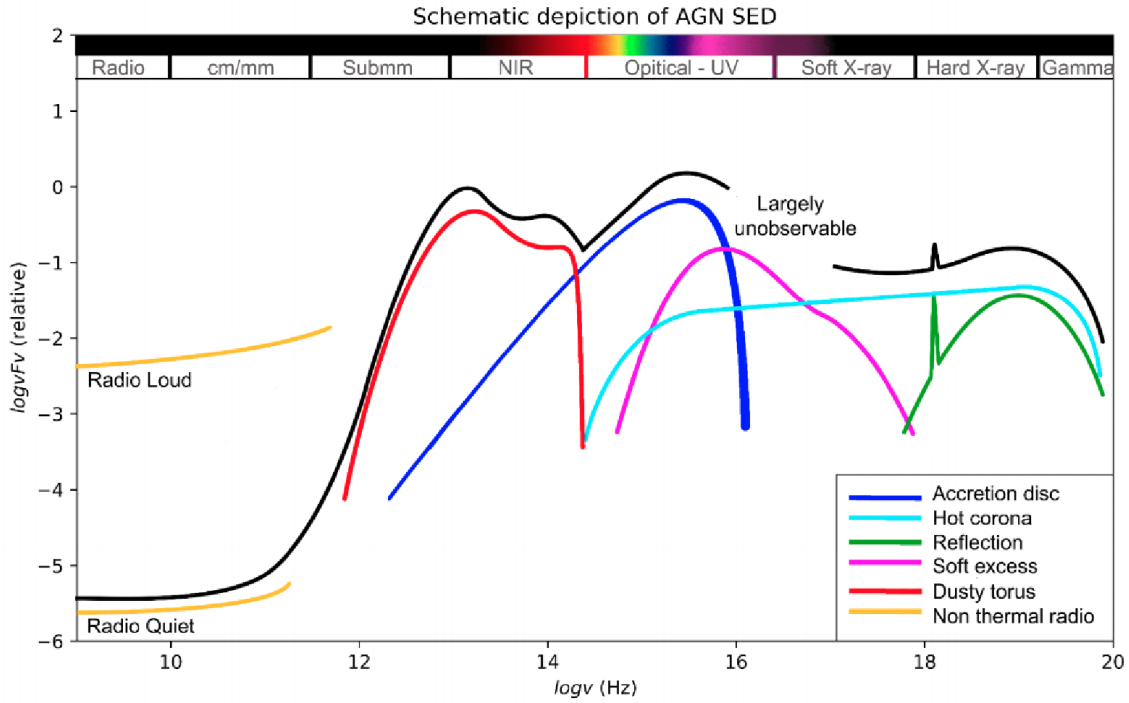

Figure 1.1: The panchromatic view of an *AGN SED* (black curve), separated into the main physical components, as indicated by the colored curves (e.g. accretion disc, corona and non-thermal radio emission from ejection). Image courtesy of F. Shankar for the Academic notes of P. Monaco 'Radiative processes Active Galactic Nuclei (2018-19)'.

1.1.1 Accretion

To further underline the point that the mechanism at work at the centre of an AGN is not of stellar origin, it is possible to evaluate the luminosity of an accreting SMBH by employing a simple but effective model. Let us assume an isotropically radiating point at distance r with bolometric luminosity L, the radiation pressure is:

$$P_{\rm rad} = \frac{L}{4\pi r^2 c} \tag{1.1}$$

The outward force on a single electron is obtained multiplying $P_{\rm rad}$ for the Thomson cross-section σ_e:

$$F_{\rm rad} = \sigma_e \frac{L}{4\pi r^2 c} \tag{1.2}$$

Considering the magnitude of the gravitational force exerted by a mass M on a mass m at a distance r to be $F_{\rm grav} = -(GMm)/r^2$, the mass m can be accreted onto the mass M when $F_{\rm rad} \lesssim -F_{\rm grav}$, which is the same as writing:

$$L \lesssim \frac{4\pi G M c m_p}{\sigma_e} \simeq 1.26 \times 10^{38} \frac{M}{M_\odot} \text{ erg s}^{-1} \tag{1.3}$$

The luminosity given by Equation (1.3) is known as the *Eddington limit* $L_{\rm edd}$, which sets the maximum luminosity that an AGN can sustain before radiation pressure halts further isotropic accretion onto the black hole. For a typical quasar $L = 10^{46}$ erg s^{-1} and therefore the Eddington mass, that is the minimum mass for a system to be gravitationally bound, is:

$$M_{\rm Edd} \sim 8 \times 10^5 \left(\frac{L}{10^{44}\,{\rm erg/s}} \right) M_\odot \tag{1.4}$$

Assuming a mass falling from infinity in a radius r onto a black hole of mass $M_{\rm BH}$ in a Newtonian approximation, there is a conversion of potential energy into kinetic energy and therefore the luminosity L of the AGN can be related to the gravitational potential U by the equation:

$$L \approx \frac{dU}{dt} = \frac{1}{2}\frac{GM_{\rm BH}}{r}\frac{dm}{dt} = \frac{1}{2}\frac{GM_{\rm BH}\dot{m}}{r} \tag{1.5}$$

where G is the gravitational constant and $\dot{m}$ is the mass accretion rate. For an accreting system, the luminosity can also be expressed as follows:

$$L = \eta \dot{m} c^2 \;\Rightarrow\; \dot{m} = \frac{L}{\eta c^2} \tag{1.6}$$

where c is the speed of light and η the efficiency of the process, which can therefore be expressed, from the equations above, as:

$$\eta \approx \frac{GM_{\rm BH}}{2rc^2} \tag{1.7}$$

with $R_s = \frac{2GM}{c^2}$ being the Schwarzschild radius of the black hole. If we assume r to be the radius of innermost circular stable orbit (ISCO), then it will depend on the angular momentum spin $J \propto aM_{BH}$, where $-1 < a < 1$ is the dimensionless angular momentum, and it is useful to explicit the connection between the ISCO and the radiative efficiency, which is:

$$r = R_{ISCO} = \zeta \frac{GM_{\rm BH}}{c^2} \qquad \text{with } \eta = 1 - \left[1 - \frac{2}{3\zeta}\right]^{0.5} \tag{1.8}$$

Depending on the magnitude and sign of the angular momentum a, we can have different radiative efficiencies, as shown in Table 1.1 and Figure 1.2.

Even when considering a non-rotating (Schwarzschild) BH ($a = 0$), the radiation output η is at least around 6% (Table 1.1) and cannot be explained by ordinary stellar processes, since the energy budget far exceeds what the star radiative efficiency $\eta_\star \sim 0.7\%$ produces through nuclear fusion. Since we will deal with rotating (Kerr) black holes, this argument becomes even more compelling, as the associated radiative output is expected to be higher. In fact, the most efficient way to convert mass into energy is through accretion of gas onto a compact object.

1.1.2 AGN feedback and SMBH-host co-evolution

To date, we know that through this process AGN can deposit a large fraction of energy in their surroundings, and in this way they shape the host galaxy and even the intergalactic medium up to distances of hundreds of Mpc. This effect is known as *AGN feedback*

a	$\zeta = \frac{R_{\mathbf{ISCO}}}{R_g}$	η
−1.0	9.00	0.038
0.0	6.00	0.057
0.1	5.67	0.061
0.5	4.23	0.082
0.9	2.32	0.156
0.998	1.24	0.321
1.0	1.00	0.423

Table 1.1: Radiative efficiency η and coefficient ζ according to different BH spin a. The gravitational radius R_g is assumed as $R_g = 0.5R_S$.

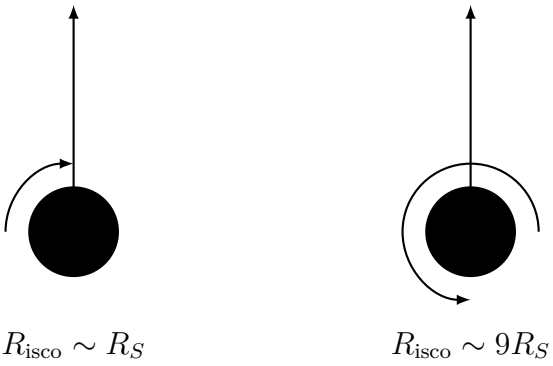

Figure 1.2: Maximum prograde (left) and maximum retrograde (right) spin for a BH in case of a clockwise angular momentum of the accretion disk.

(Fabian 2012), and essentially can be grouped into two modes: the radio/jet and the radiative/quasar mode. Large optical-radio surveys, like those performed by Best and Heckman (2012) and Heckman and Best (2014), show that 'jet-mode' AGN are preferentially hosted by massive, gas-poor ellipticals fuelled at a low accretion rate, whereas 'radiative-mode' AGN reside in quasar-like AGN, hosted by bluer galaxies with a large availability of cold gas. Both types of feedback are required to explain the star-formation shutdown in galaxies in the local Universe and the empirical relations observed between the host and the SMBH (Ciotti et al. 2009, 2010). This mechanism plays a crucial role in the life of the host galaxy, establishing a symbiotic link with the central active supermassive black hole in the form of SMBH–host coevolution. Active galactic nuclei regulate the bulge formation by heating and expelling gas, which subsequently falls back onto the SMBH, thereby influencing its accretion. One of the most important empirical relations demonstrating this coevolution is the Magorrian relation (Magorrian et al., 1998), but see also more recent studies such as Kormendy and Ho 2013; Gebhardt et al. 2000; Ferrarese and Merritt 2000, which shows the proportionality between the SMBH mass and the stellar velocity dispersion $\sigma_\star$ ($M_{BH} \propto \sigma_\star^{4-5}$), the latter being a tracer of the mass of the galaxy.

A quantification of this link between the host galaxy and the SMBH can be expressed by the following expression, showing the ratio between the energy output due to SMBH accretion $\mathrm{E_{BH}}$ and the host galaxy binding energy $\mathrm{E_{gal}}$:

$$\frac{\eta \mathrm{M_{BH}} c^2}{\mathrm{M_{gal}} \sigma_\star^2} \sim \frac{0.1 \mathrm{M_{BH}} \mathrm{c}^2}{10^3 \mathrm{M_{BH}} \sigma_\star^2} = 10^{-4} \left(\frac{c}{\sigma_\star}\right)^2 \tag{1.9}$$

where we have assumed $\eta \sim 10\%$ and the mass of the galaxy $\mathrm{M_{gal}} \sim \mathrm{M_{bulge}}$ is inferred from the Magorrian relation and can be written as $\mathrm{M_{gal}} \sim 10^3 \mathrm{M_{BH}}$. From Equation 1.9 emerges $\mathrm{E_{BH}} \gg \mathrm{E_{gal}}$, which shows that the energy produced by the growth of the black hole can exceed the binding energy of the galaxy by a large factor. If even a small fraction of the energy is transferred to the gas, then an AGN can have a profound effect on the evolution of its galaxy.

1.1.3 Ejection

As described in the previous section AGN release large amounts of energy in their external medium and this can happen through different mechanisms, i.e. radiation, winds and jets. Among these, in this project we have focussed on jets (Figure 1.3), which are highly-collimated outflows of relativistic plasma and magnetic fields launched from the vicinity of the SMBH, which can transport substantial amounts of energy, momentum, and angular momentum to the surrounding medium (Blandford and Rees, 1974). The most powerful and spatially extended jets are generally found in the most massive elliptical galaxies (Capetti, A. et al., 2022), but they can span a long range, from the sub-kiloparsec to megaparsec scales. Because they consist of charged particles moving into magnetic fields, jets emit synchrotron radiation, which we will discuss in more detail in Section 1.1.4.

Despite more than five decades of dedicated investigation, the formation and evolution of the jets are still not fully understood. Many open questions remain, such as the mechanism that drives the jet formation, its full life-cycle, and how it interacts with the ambient environment. Addressing these issues is essential to also improve our understanding of the SMBHs dynamics and their role in shaping galaxies and larger structures.

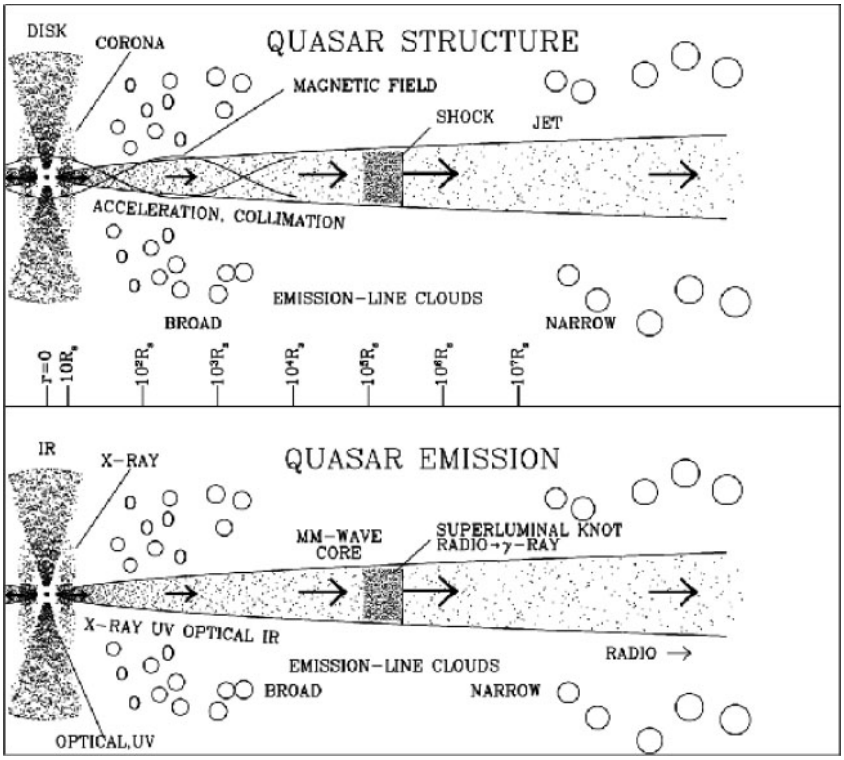

Figure 1.3: Illustration of the central part of a radio-loud AGN. The density of the dots in the disk, corona, and jet very roughly indicates the density of plasma (top panel) or intensity of emission (bottom panel) in a reference frame in which there is no beaming. Note the logarithmic length scale beyond 10 Rs, where Rs is the Schwarzschild radius. Only a single superluminal knot is shown; usually there are several. Image credit: Marscher (2005).

In particular, the origin of relativistic jets remains an unresolved challenge in astrophysics. Two of the most widely discussed theoretical mechanisms are those proposed by Blandford and Payne (1982) and Blandford and Znajek (1977). The former suggests that jets are launched as outflows from a magnetised accretion disk, whereas the latter involves extracting rotational energy directly from a spinning black hole via magnetic coupling with the surrounding plasma. The key distinction between the two models lies in the primary energy reservoir: the disk in the Blandford–Payne mechanism versus the BH spin in the Blandford–Znajek model. Despite this difference, both models fundamentally rely on the presence of large-scale magnetic fields; either as drivers of energy extraction or as a facilitating medium.

It is clear that the jet-launching efficiency depends on the geometry and strength of the magnetic field and on black hole spin. Some major insight comes from the two models just described, but there seems to be no unification yet on this matter, as in practice both effects may coexist in the same system: the inner disk launches a mildly relativistic wind (BP) while the black hole spin powers the highly relativistic spine[4] (BZ). More specifically: low-Eddington, hot (RIAF) flows favour BZ-jets, while higher-accretion (optically thick) disks can also launch BP-driven sheath winds.

1.1.4 Synchrotron emission in astrophysical sources

As mentioned earlier, synchrotron radiation is one of the most prominent non-thermal emission mechanisms in astrophysics, and by far the most dominant in jets. It occurs when charged particles are accelerated to relativistic speeds, pushed by the *Lorentz force*, and spiral along magnetic field lines, emitting electromagnetic radiation. This process is central for the interpretation of various astrophysical observations and occurs across a wide range of environments and spatial scales, from compact stellar remnants to large-scale structures like galaxy clusters.

The emission from a single relativistic charged particle spiraling in a magnetic field is governed by the *Larmor formula:*

$$\frac{d\varepsilon}{dt}(t) = \frac{1}{6\pi\varepsilon_0}\frac{e^2}{m_0^2 c^3}\gamma^2\left(\frac{d\vec{p}}{dt}\right)^2 \tag{1.10}$$

where e is the electron charge, ε_0 the vacuum permittivity ($\approx 8.85 \cdot 10^{-12}$ F/m), m_o the rest-frame mass of the particle, c the speed of light, $\gamma = 1/\sqrt{1-(v/c)^2}$ is the Lorentz factor, v and $\vec{a} = d\vec{p}/dt$ the speed and acceleration of the particle, respectively. Equation 1.10 refers to a generic charged particle; however, since $m_p/m_e \approx 1836$, the proton population is shadowed by the electrons when it comes to synchrotron emission, henceforth we will consider only the electrons. Moreover, only the velocity component perpendicular to the magnetic field $\vec{B}$ contributes to the acceleration, since $\vec{F}_L = e(\vec{v} \times \vec{B})$ vanishes when $\vec{v} \parallel \vec{B}$. Thus, only the perpendicular component radiates in the Larmor formula, with most of the emission occurring in a conical region of semi-aperture $1/\gamma$. This preferential distribution is due to the relativistic effects that produce the *beaming effect* in Figure 1.4, which is therefore absent in the sub-relativistic regime (i.e., cyclotron emission).

[4] In the spine-sheath stratified jet model, the *spine* refers to the fast, inner relativistic flow—likely powered by black hole spin—while the *sheath* is a slower outer layer, possibly launched from the accretion disk (Ghisellini et al., 2005).

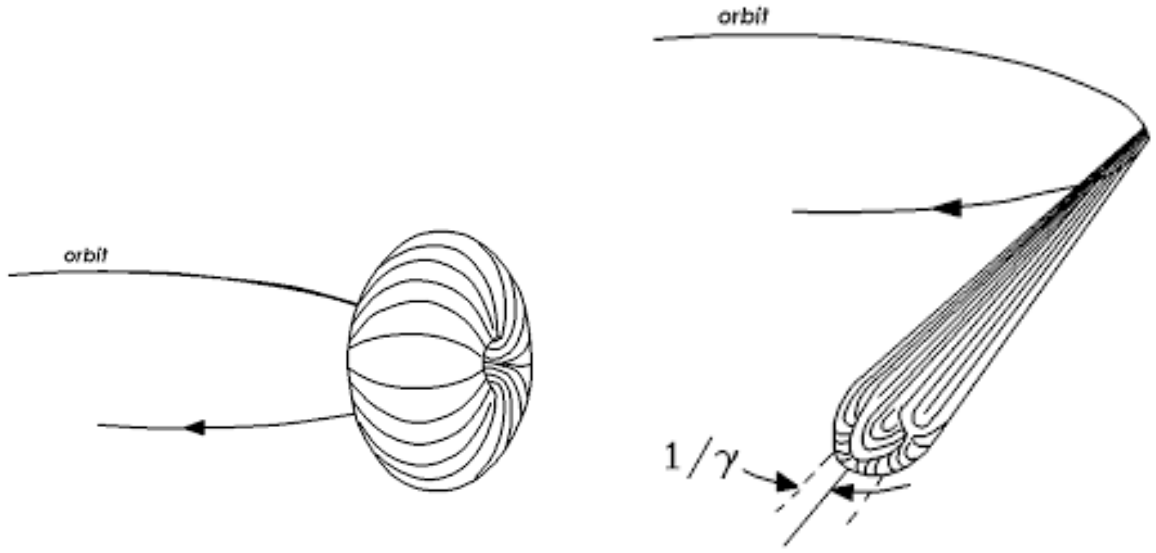

Figure 1.4: Left: At low electron velocity (non-relativistic case $v/c \ll 1$) the radiation is emitted in a non-directional isotropic pattern. Right: when the electron velocity approaches the speed of light $v/c \approx 1$, most of the emission pattern is beamed in the direction of motion of the electron (mostly in a cone with semi-aperture γ^{-1}.) due to the effects of relativistic aberration between his instantaneous rest frame and the observer frame of reference. Image credit: Grandsaert (2021).

When considering a population of electrons, which is a far more practical astrophysical instance, the synchrotron emissivity is the result of the superposition of individual contributions (Figure 1.5), assuming that no absorption mechanism is present within the source. In particular, jets are thought to accelerate particles through the *Fermi II acceleration* mechanism, which produces a population of particles with a power-law energy distribution of this type

$$N(\varepsilon)d\varepsilon \propto N_0 \varepsilon^{-\delta} d\varepsilon \tag{1.11}$$

with N_0 being the normalisation constant. To solve this, we need to find an expression that describes how the emissivity profile varies with time, by putting $a_\perp$ into the Larmor equation (Equation 1.10) and integrating over an isotropic distribution of pitch angles, one gets

$$\frac{d\varepsilon}{dt} = \frac{4}{3}\sigma_T \, c \, U_{\text{mag}} \, \gamma^2, \tag{1.12}$$

where $\sigma_T = e^4/6\pi\varepsilon_0^2 m_e^2 c^4$ is the Thomson cross-section and $U_{\text{mag}} = B^2/2\mu_0$ is the magnetic energy density. The synchrotron frequency is $\nu_s \propto \varepsilon^2 B$, which can be obtained by Fourier analysis. By combining all the terms inside Equation 1.11 it results in the total power per unit frequency $F(\nu)$:

$$F(\nu)d\nu \sim N_0 B^{(\delta+1)/2} \nu^{-\alpha} \tag{1.13}$$

with

$$\alpha = \frac{\delta - 1}{2} \tag{1.14}$$

being the *spectral index*, which is intimately related to the energy distribution. By measuring α, it is possible to infer the properties of the acceleration mechanism. Typical values are in the range α=0.5-0.7. An immediate consequence of this formulation is that lower frequencies tend to dominate the observed emission, as shown in the left plot of Figure 1.5. This is because there are typically far more low-energy electrons than high-energy ones in a power-law distribution.

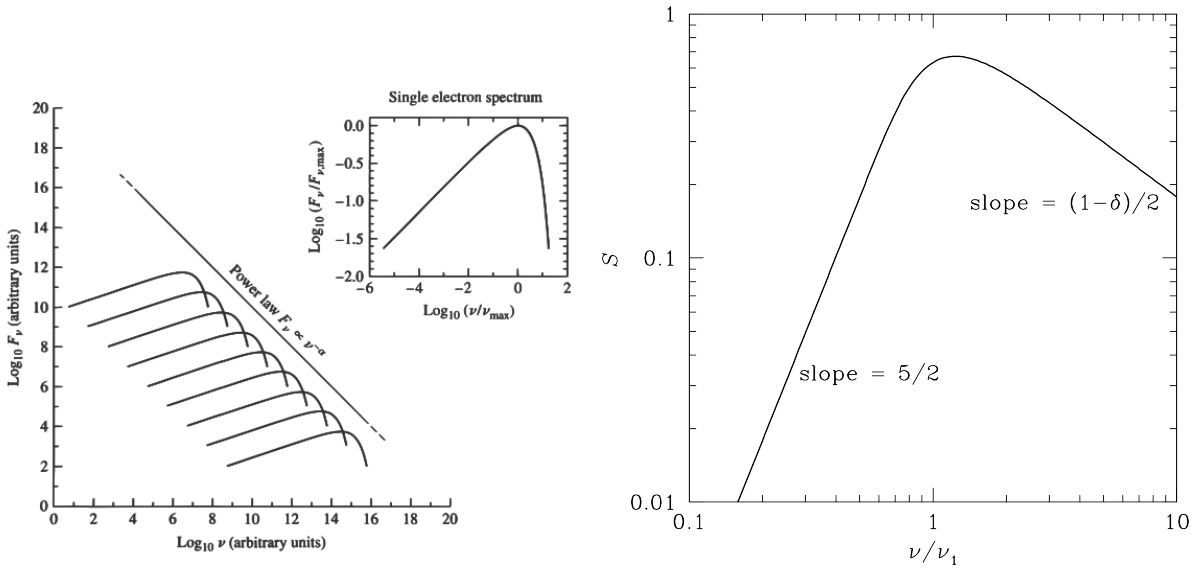

Figure 1.5: (Left) Logarithmic synchrotron radiation spectrum, seen as a superposition of many individual electrons as they spiral around magnetic field lines. The spectrum of a single electron is at the upper right. Image credit: Carroll and Ostlie (2017). (Right) Ideal spectrum of a self-absorbed synchrotron source, where S is the flux density F for us. Image credit: Condon and Ransom (2016).

However, real astrophysical sources often exhibit synchrotron spectra that deviate from the idealised power-law behaviour. These deviations can arise from a range of physical processes, including spectral ageing, particle re-acceleration, thermal absorption, or magnetic field inhomogeneities.

Here, we briefly discuss *synchrotron self-absorption* (SSA) and *spectral ageing*.

Self-absorbed synchrotron spectra

The power-law spectrum $F(\nu) \propto \nu^{-\alpha}$ in Equation 1.13 results from the superposition of radiation emitted by individual relativistic electrons, under the assumption that the source is optically thin to its own radiation. However, this assumption breaks down as the brightness temperature of the source approaches the kinetic temperature of the emitting electrons. In this regime, radiative self-absorption becomes significant, and the energy from incoming photons is efficiently reabsorbed by the plasma, preventing any further rise in temperature and consequently reducing the observable radio power.

As a power-law energy distribution is a typical characteristic of non-thermal sources, such as synchrotron-emitting plasmas, the absorption coefficient cannot be directly derived from Kirchhoff's law due to the lack of thermal equilibrium. Nonetheless, the

emission from a single relativistic electron is nearly monochromatic[5], which allows the emission of an ensemble of electrons to be approximated as a superposition of narrow spectral features resembling a Maxwellian distribution. Under this approximation, the brightness temperature T_b can be estimated as:

$$T_b \approx \left(\frac{m_e c^2}{3k}\right)\left(\frac{\nu_s}{\nu_L}\right)^{1/2}, \tag{1.15}$$

where k is the Boltzmann constant, m_e is the electron mass, ν_s is the observing frequency, and ν_L is the Larmor frequency. This expression reflects the balance between the radiation energy density and the kinetic energy of the radiating electrons.

At low frequencies, where SSA dominates, the plasma becomes optically thick and the brightness temperature saturates. Solving the radiative transfer equation in this regime yields the following expression for the observed flux density:

$$F_\nu = 2kT_b\frac{\nu^2}{c^2}\,\Omega \approx \frac{2m_e}{3}\left(\frac{\nu_L^{1/2}}{\nu^{5/2}}\right)\Omega \propto \frac{\theta^2\nu^{5/2}}{B^{1/2}} \tag{1.16}$$

where Ω is the solid angle subtended by the source, θ is its angular size, and B is the magnetic field strength. The dependence $F_\nu \propto \theta^2\nu^{5/2}$ is the distinguishing characteristic of the low-frequency optically thick regime of SSA, which is particularly significant for compact radio sources (lower θ). The SSA spectrum exhibits two characteristic regimes (right plot in Figure 1.5), governed by the optical depth τ:

$$\text{optically thick}: \quad \tau \gg 1 \quad \Rightarrow \quad B_\nu \sim \nu^{5/2}B_\perp^{-1/2} \tag{1.17}$$

$$\text{optically thin}: \quad \tau \ll 1 \quad \Rightarrow \quad B_\nu \sim \nu^{-\alpha}B_\perp^{(\delta+1)/2} \tag{1.18}$$

The transition between these regimes defines a critical frequency, the *synchrotron peak frequency* ν_p, which marks the maximum of the observed flux density F_p. This frequency depends on the angular size of the emitting region and the strength of the local magnetic field. It is approximately given by:

$$\nu_{s,\mathrm{peak}} \propto F_p^{2/5}\theta^{-4/5}B_\perp^{1/5}(1+z)^{1/5} \tag{1.19}$$

If F is expressed in Jy (10^{-26} W Hz^{-1}m^{-2}), θ in milliarcseconds (mas), $B_\perp$ in milligauss (mG), and the frequency in GHz, the constant in Eq. 1.19 takes the value ~ 2, with a moderate dependence on the spectral index. As an example, for $z = 1$, $B = 1$ mG, $\theta = 5$ mas, $F = 1$ Jy, one finds $\nu_\mathrm{max} \approx 1.1$ GHz.

The brightness temperature of Eq. 1.15, at the frequency ν_max, becomes:

$$T_{B,\mathrm{max}} \approx 3 \times 10^{10}\,\nu_\mathrm{max}^{0.5}\,B^{-0.5}$$

Finally, we observe that by measuring the angular diameter of a radio source θ, for which the spectral peak is known, it is possible, from Eq. 1.17, to estimate the magnetic field of the radio source:

$$B \propto \mathrm{const} \times \nu_\mathrm{max}^5 F_\mathrm{max}^{-2}\theta^4(1+z)^{-1}$$

[5]Because it is mostly emitted around the critical frequency $\nu_c \sim \gamma^2\nu_L$, with $\nu_L = (eB)/(2\pi m_e c)$ being the Larmor frequency.

In reality, this determination is generally quite uncertain because the magnetic field B depends on high powers of the observational quantities, so even small uncertainties lead to large errors on B, which is therefore usually determined only within an order of magnitude (Fanti and Fanti, 2012).

Spectral ageing

We close the overview on the synchrotron emission by briefly presenting the effect that, complementary to SSA, is happening in the high frequency range of the radio spectrum.

In fact, one of the main signatures of particle ageing in radio sources is a spectral break at high frequencies, which arises due to energy losses experienced by the most energetic electrons. As these particles lose energy over time, their emission shifts from higher to lower frequencies, leading to a deviation from the original power-law shape of the synchrotron spectrum. The frequency at which this transition occurs is known as the *break frequency* (ν_b), and it marks the point where the spectrum becomes steeper due to radiative ageing. The accumulation of the energy losses results in a practical way to date back the plasma, and they can be fitted with theoretical models that numerically simulate the deviation from the power-law. Alternatively, the spectral age can be analytically derived with the approach described in Slee et al. (2001); Brienza et al. (2020):

$$t_s = 1590 \cdot \frac{B^{0.5}}{(B^2 + B^2_{\rm CMB}) \cdot \sqrt{\nu_b (1+z)}} \tag{1.20}$$

where t_s is the synchrotron age in Myr, B is the magnetic field in μG, $B_{\rm CMB} = 3.25(1+z)^2$ is the equivalent magnetic field of the cosmic microwave background (CMB), ν_b is the spectral break frequency in GHz, and z is the redshift.

1.2 Unified Model

The classification of AGN is a never-ending evolving scheme that started around 80 years ago based on the different band used, from radio to the high-energy (optical/X-ray and Gamma). In fact, the criteria that are applied to identify and categorize the vast number of AGN are tied to the technological limit of the epoch, as well as the features of the object we are observing: that could be the waveband, the spectrum, the morphology or any other feature that highlights and adds some extra detail to these multi-facets objects.

The merging of data from various frequencies, each presenting a unique view of AGN physics, led to the identification of a shared framework known as the *Unified Model* (UM, Antonucci 1993; Urry and Padovani 1995; Padovani et al. 2017), which tries to answer the pressing question on whether all these distinct appearances of AGN can be explained by a common underlying model, or whether the different classes are intrinsically distinct.

The basic UM predicts different flavours of AGN by considering only different viewing angles, as shown in Figure 1.6. The whole system is built upon the SMBH, the engine that sits in the innermost ($\sim 10^{-7} - 10^{-3}$ pc) nuclear region of the galaxy, accreting the surrounding material and producing the multi-component SED of Figure 1.1.

According to the classical model by Shakura and Sunyaev (1973), the accretion disk is optically thick with a geometrically thin structure that extends from $\gtrsim 10^{-7}$ to 1 pc. It

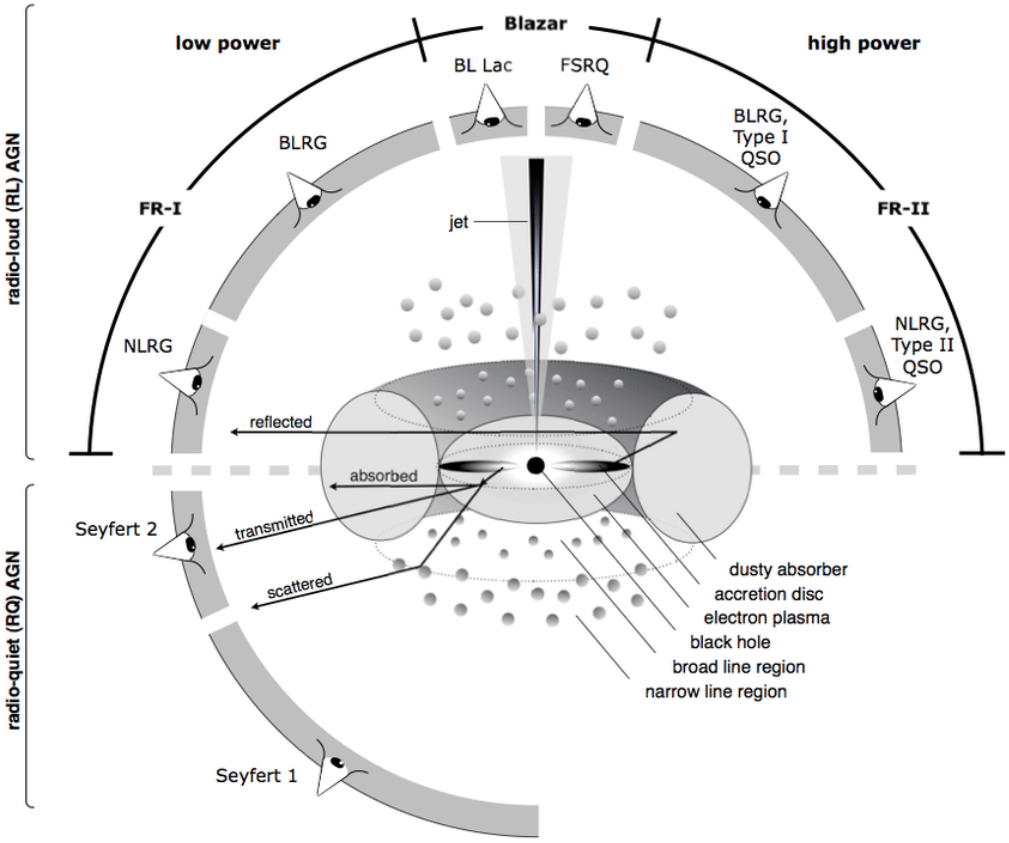

Figure 1.6: Schematic representation of the AGN phenomenon in the unified scheme. The type of object we see depends on the viewing angle and on the power of the central engine. Image Credit: Beckmann and Shrader (2012), graphic by Marie-Luise Menzel.

is composed of concentric rings of gas at increasing temperatures[6] as one approaches the black hole, reaching up to $\sim 10^6$ K. This temperature gradient results in a multicolour blackbody spectrum peaking in the optical to ultraviolet (UV) range, called *Big Blue Bump* (BBP, blue curve in Fig. 1.1). Surrounding the innermost regions of the disk lies a hot ($T \sim 10^8$–10^9 K) plasma known as the *corona* (Raginski and Laor, 2016; Laha et al., 2025).

Although its exact geometry and origin remain debated, the corona is thought to be responsible for the power-law emission observed in the X-ray band (light blue curve in Fig. 1.1). Soft thermal photons emitted by the disk are upscattered via inverse Compton processes in the corona, producing high-energy photons, and some of them interact again with the disk, generating a *reflection component* (green curve in Fig. 1.1), including the prominent Fe Kα fluorescence line around 6.4 keV, particularly useful for probing the ionisation state of the disc. The usefulness of the iron line does not end there, as the relativistic effects featured in the line profile can be used to infer some of the disc geometrical details (especially for unobscured type 1 Seyfert), including the inner radius ($\simeq$ ISCO) and thus BH spin, inclination, and emissivity profile.

Another frequently observed X-ray feature is the *soft excess* (pink curve in Fig. 1.1), an excess of emission below $\sim$ 2 keV that could be produced by a "warm corona," an optically thick layer of cooler electrons ($T \sim 10^6$–10^7 K) upscattering disk photons

[6] A useful relationship link the temperature of the disc to the BH mass: $T_{disc} \propto M_{BH}^{-0.25}$.

(Petrucci et al., 2018). This region may act as an intermediate Comptonization layer between the accretion disk and the hot corona. Within $10^{-2} - 10^{-3}$ pc, several gas clouds form the so-called *Broad Line Region* (BLR), which emits broad optical-UV emission lines with typical widths on the order of several thousands km·s^{-1}. Surrounding the BLR, from about 1 to 10 pc, lies a clumpy toroidal structure of gas and dust at temperatures around 10^3 K. This *dusty torus* plays a key role in reprocessing the optical/UV light from the disk into infrared (IR) emission (red curve in Fig. 1.1). Its geometry and orientation explain the obscuration observed in Type 2 AGN, but its geometry is still under debate. Outside the torus, extended (kpc-scale) gas clouds produce narrow emission lines with widths of the order of several hundred km·s^{-1}, by which the name of *Narrow Line Regions* (NLR). Finally, *relativistic radio-jets* can be produced and expand up to even Mpc scales, contributing with the non-thermal synchrotron emission (yellow curve in Fig. 1.1), but also to IR, optical, X-ray, and even γ-ray frequencies (Blandford and Königl, 1979; Baldi, 2023) and can be aligned to the line of sights or not, showing different classes, Blazars and radio galaxies, respectively.

We note that this orientation-based unification has been remarkably successful in matching many properties of Type 1 and Type 2 objects, however, modern literature (e.g. Padovani et al. 2017) emphasises that orientation alone cannot account for all differences. Several additional physical and evolutionary factors have been increasingly acknowledged as essential components of a more complete picture, which may include: accretion rate, host galaxy properties, BH mass and spin, torus structure and covering factor, surrounding environment, and also the evolutionary phase.

1.3 Radio-loud AGN

Radio-loud AGNs represent a subclass of the AGN population where the radio emission is dominant. To quantify this, the *radio-loudness parameter* was historically introduced, defined as $R = F_5/F_B$, where F_5 is the flux density at 5 GHz and F_B the optical flux in the B band (Kellermann et al., 1989). AGNs with $R \geq 10$ are considered radio-loud and account for about 10-20% of the of the overall AGN population.

In opposition to these are radio-quiet (RQ) AGN, which are $\sim 10^3 - 10^4$ times less luminous at radio wavelength than RL AGN. In these sources the radio emission is thought to originate from a combination of different processes including jets, winds and star formation. While RL AGN are usually associated with the most massive, early type galaxies, RQ are generally associated with Seyfert galaxies. We note that the traditional RQ/RL dichotomy is in fact now considered somewhat outdated, and recent literature, e.g. Padovani et al. (2017), prefers a more physically motivated terminology, distinguishing AGN as *jetted* (for RL) and *non-jetted* (for RQ[7]), to better reflect the underlying presence or absence of relativistic jets, rather than relying solely on a radio luminosity threshold.

Among radio-loud AGN, which are the subject of this thesis, are radio galaxies (RG), which show collimated relativistic jets mostly oriented on the plane of the sky. The morphology of a RG is not uniquely defined, but some of the main components (see Figure 1.7) are:

[7]Although, evidence for jetted RQ AGN have been found, with sub-relativistic jet-like structures at the pc-scale (Padovani 2016.

- *the core:* the nuclear emission, usually displaying a flat spectrum ($|\alpha| < 0.5$) and small sizes, it is the site where the jets are formed and launched;

- *the jets:* collimated beams of relativistic particles, which can assume various shapes due to the interplay with the ambient medium, displaying regions of higher brightness called knots;

- *the lobes:* radio structures surrounding the jets and inflated by their expansion;

- *the hot-spots*: bright regions located at the end of the jets, originating from the shocks produced by the jet impacting the external medium.

This first morphological classification of radio galaxies was made by Fanaroff and Riley (1974), who arranged RGs into *FR I* and *FR II* by looking at the brightness distribution along the resolved extended structures (jets, lobe) as observed in radio surveys like the 3C catalogue:

- **FR I:** exhibit *edge-darkened* morphologies, with radio emission that is brighter near the core and fades outward along the jets and lobes (Figure 1.7, right) . They typically have radio luminosities below $2 \times 10^{25}\,\mathrm{W\,Hz^{-1}sr^{-1}}$ at 178 MHz (Zirbel and Baum, 1995). They are prevalent in dense cluster environments, where their jets can be rapidly decelerated;

- **FR II:** show *edge-brightened* morphologies, with radio emission peaking at the lobe edges (Figure 1.7, left) where bright *hotspots* are located. FR IIs, with respect to FR Is, are more luminous (luminosities higher than $2 \times 10^{25}\,\mathrm{W\,Hz^{-1}sr^{-1}}$ at 178 MHz), host more powerful and collimated jets and are often observed at higher redshifts.

Complementary to this morphological classification, an optical spectroscopic classification was proposed for radio galaxies by Laing et al. (1994) to reflect differences in accretion, namely the *Low Excitation Radio Galaxies (LERG or LEG)* and *High Excitation Radio Galaxies (HERG or HEG)*. The latter is associated with bluer star-forming galaxies with radiatively efficient Shakura-Sunyaev accretion discs (Eddington ratio $\lambda_{\mathrm{Edd}} \sim 1{-}10\%$). LERGs, on the other hand, show weak or no emission lines, indicative of radiatively inefficient ($\lambda_{\mathrm{Edd}} \lesssim 1\%$) accretion from hot gas in massive, quiescent red early-type galaxies (ETGs, i.e. ellipticals).

Although both HERGs and LERGs can exhibit FR I or FR II morphologies, there is a statistical tendency for LERGs to correspond to FR Is and HERGs to FR IIs. This suggests a coupling between the accretion mode and jet power, possibly modulated by black hole spin or magnetic flux. However, the delineation is ambiguous; for example, FR IIs are easily associated with both HERGs and LERGs.

When the jet is closely aligned with the line of sight (angles smaller than 5°), RGs are called *blazars*, and are further subdivided into *flat-spectrum radio quasars* (FSRQs) and *BL Lacertae objects* (BL Lacs), depending on the presence or absence of strong broad emission lines ($EW > 5\,\text{Å}$), respectively. The multi-band properties of these sources are generally morphologically compact and very variable.

Moreover, relativistic beaming significantly enhances the non-thermal emission from the jet in these sources. In fact, the observed flux can be significantly affected by Doppler boosting, which is quantified by the *Doppler factor* δ as:

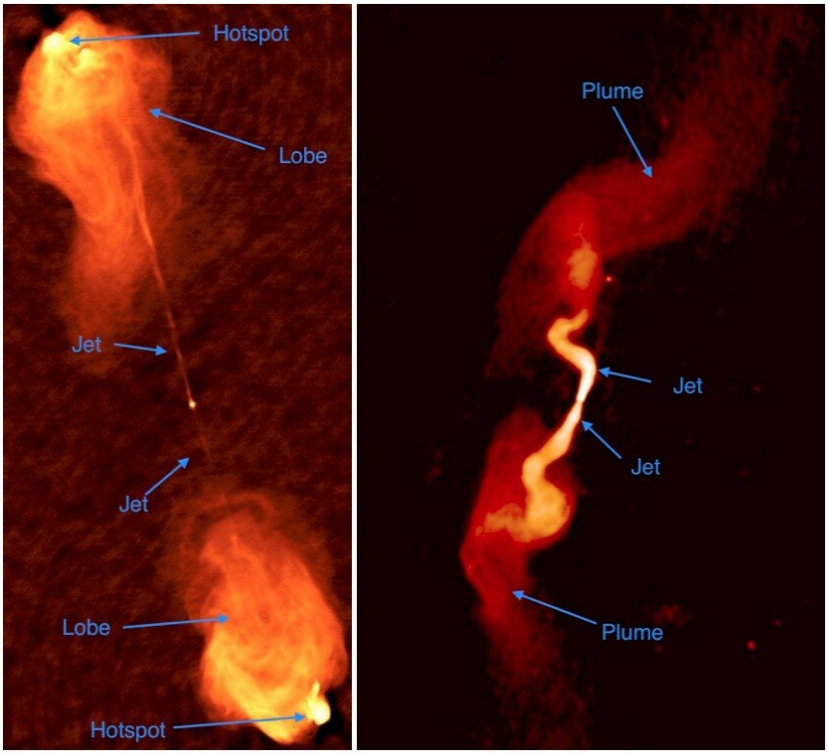

Figure 1.7: Powerful FR II radio jets in CygnusA (left) and the weak FR I jets in 3C 31 (right) from the Very Large Array (VLA) radio maps. Credit: NRAO/AUI.

$$\delta = [\gamma(1 - \beta \cos\theta)]^{-1} \tag{1.21}$$

where $\beta = v/c$, and $\gamma = (1 - \beta^2)^{-1/2}$ is the Lorentz factor. The angle θ represents the orientation between the jet axis and the observer's line of sight (LOS):

- $\theta = 0°$ (aligned with LOS), $\delta = (1 + \beta) \,/\, (1 - \beta) = \delta_{\max}$
- $\theta = 90°$ (perpendicular to LOS), $\delta = (1 - \beta^2)^{-1/2} = \delta_{\min}$

Finally, sources with intermediate viewing angles exhibit a mixture of characteristics: the relativistic jet is less boosted, allowing both the BLR and accretion disk emissions to contribute to the observed spectrum. Such objects are typically classified as steep-spectrum radio quasars (SSRQs), and, at lower luminosities, as broad line radio galaxies (BLRGs). Overall, also within the RL AGN population the viewing angle represents a critical parameter for defining the observable properties of the sources as proposed by the Unification model.

When radio galaxies are seen at angles smaller than 5° with respect to the line of sight, their properties significantly change as their jets point directly towards us. These sources are called **Blazars**, and their multi-band properties are generally morphologically compact and very variable.

Hence, depending on the jet orientation, relativistic beaming can serve as a powerful amplifier of the observed flux, as illustrated in Figure 1.8. This effect underpins the empirical division between radio galaxies and radio quasars, typically occurring at viewing angles greater than 45° and less than 45°, respectively (Urry and Padovani 1995).

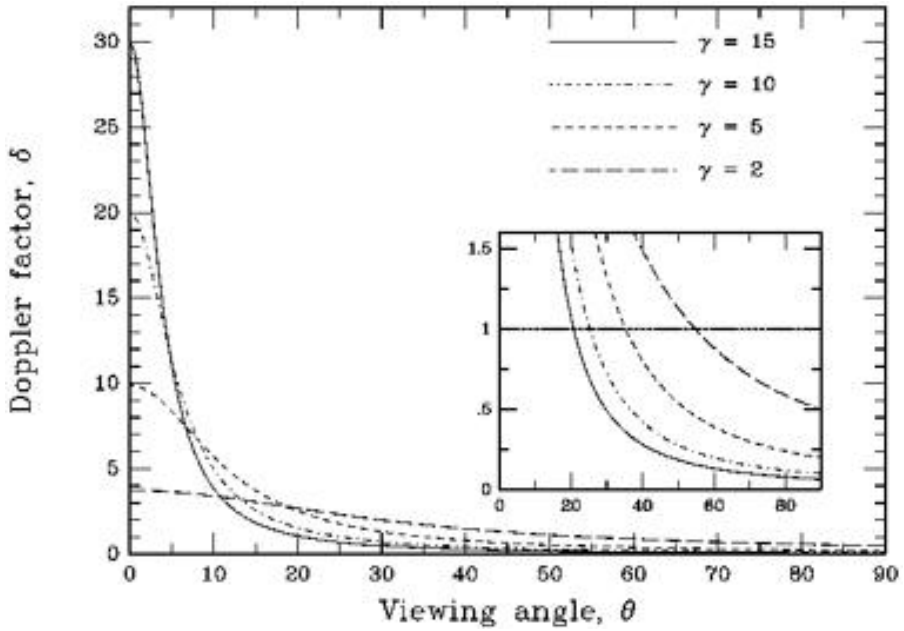

Figure 1.8: Doppler factor δ as a function of viewing angles θ for different values of Lorentz factor γ. The inset shows a zoom-in on the Doppler factor in the range between 0 and 1. Image credit: NASA/IPAC.

However, RL-AGNs constitute a heterogeneous class encompassing various types of sources. According to the unified scheme proposed by Urry and Padovani (1995), the observed characteristics of a RL source are primarily determined by the angle between the jet axis and the line of sight of the observer. When the observer's viewpoint is nearly perpendicular to the jet axis, the dusty torus effectively obscures the accretion disk and the BLR. In such cases, the optical spectrum is dominated by narrow emission lines, and the source is classified as a *Narrow Line Radio Galaxy* (NLRG). In contrast, when the jet is closely aligned with the line of sight, relativistic beaming significantly enhances the non-thermal emission from the jet. These objects are observed as *blazars*, which are further subdivided into *flat-spectrum radio quasars* (FSRQs) and *BL Lacertae objects* (BL Lacs), depending on the presence or absence of strong broad emission lines ($EW > 5\,\text{Å}$), respectively. Sources with intermediate viewing angles exhibit a mixture of characteristics: the relativistic jet is less boosted, allowing both the BLR and accretion disk emissions to contribute to the observed spectrum. Such objects are typically classified as steep-spectrum radio quasars (SSRQs), and, at lower luminosities, as broad line radio galaxies (BLRGs).

1.3.1 Compact radio galaxies and FR 0s

Among the various morphologies displayed by radio-emitting AGNs in the local Universe, the most prevalent is that of a compact, unresolved radio core (Baldi and Capetti 2010). This became evident with the advent of deep, wide-area radio surveys, which provided a more complete census compared to earlier high-flux-limited samples such as the 3C, 2Jy, B2 samples (Bennett 1962b; Wall and Peacock 1985; Colla et al. 1975). These earlier surveys mainly detected large-scale radio galaxies, typically associated with FR I and

FR II morphologies, extending over tens to hundreds of kpc. However, combining optical and radio data (e.g., Best et al. 2005; Best and Heckman 2012) revealed a significant population of unresolved RGs with sizes smaller than 20 kpc, up to z = 0.3.

Compact radio sources (CRSs) were historically viewed as misaligned RL-AGN in early evolutionary stages, often showing peaked spectra due to synchrotron self-absorption (SSA) below 1 GHz. These can exhibit flat, inverted, or complex spectral shapes due to overlapping emission regions. While CRSs appear across a wide range of galaxy types, applying morphological filters to select ETGs helps reduce contamination, as RL-AGN are mostly found in evolved galaxies with stellar masses exceeding $10^{11}\,M_{\odot}$ (Best et al. 2005; Ho 2008; Best and Heckman 2012; Kozieł-Wierzbowska et al. 2017; Magliocchetti 2022).

Baldi and Capetti (2010) found that ∼80% of SDSS/NVSS compact sources were low-excitation radio galaxies (LERGs) with jet powers ∼1000 times lower than classical FR I RGs of comparable AGN luminosity, suggesting a large population of low-luminosity CRSs had been missed. To address this, Ghisellini (2011) introduced the term FR 0 to describe compact, core-dominated RL-AGNs with weak or absent extended emission (Figure 1.9), such as Core galaxies (CoreG[8].), despite having bolometric luminosities similar to FR Is (e.g. M87).

FR 0s typically fail to develop large-scale jets, possibly due to intrinsic properties of their accretion–ejection mechanisms. While initially thought to be young RGs, their high space density, as shown by Baldi et al. (2018, 2019a), rules out the idea that all FR 0s evolve into extended FR Is/IIs. Instead, they seem to form a distinct, numerous RL-AGN population in the local Universe.

Detecting FR 0s remains challenging, particularly at mJy flux densities ($z \lesssim 0.3$), where contamination by RQ-AGNs, star-forming galaxies, and blazars is more likely, and standard diagnostics often fail. Nonetheless, Baldi et al. (2018) compiled FR0CAT, a dedicated sample of 104 compact RL-AGNs for further study.

FR 0s hold astrophysical importance for several reasons (Baldi, 2023): (i) they offer insights into inefficient AGN accretion–ejection mechanisms; (ii) despite compact morphology, they can efficiently impact host galaxies via mechanical feedback; and (iii) they are 4.5 times more common than FR Is in the local Universe, making them the dominant RL-AGN class.

Multi-wavelength observations show FR 0s share nuclear properties with FR Is, but differ in radio morphology and power. Their broadband radio spectra (150 MHz–22 GHz; Capetti et al. 2020a; Baldi et al. 2019a, Baldi et al in prep.) are flat ($-0.01 < \alpha < 0.025$), consistent with self-absorbed cores rather than extended lobes. Classical RL-AGNs typically show steeper spectra ($\alpha \sim$ –0.6). VLBI studies confirm flat-spectrum cores and, when present, pc-scale jets with steep spectra ($\alpha \sim$ –1 to –2), suggesting most radio emission originates from compact cores (Cheng and An, 2018; Cheng et al., 2021; Baldi et al., 2021; Giovannini et al., 2023).

Optically, FR 0s are mostly massive ETGs ($-23 \lesssim M_r \lesssim -21$; $M_{\star} \approx 10^{10}-10^{11}\,\mathrm{M}_{\odot}$), but nuclear accretion signatures remain poorly constrained. Their radio-loudness ($R > 11$) confirms their RL-AGN classification. The [O III]λ5007 line traces AGN power and correlates with core radio luminosity, but FR 0s show total radio power ∼100–1000 times

[8]The Core Galaxy nomenclature comes from the (core-type) optical flat surface brightness profile in innermost region of an elliptical (e.g. Faber et al. 1997) and host genuine 'miniature' radio galaxy with LERG-like nuclei, which extend the nuclear luminosity correlations reported for FR Is by a factor of ∼1000 toward lower luminosities (Balmaverde and Capetti, 2006; Baldi and Capetti, 2010)

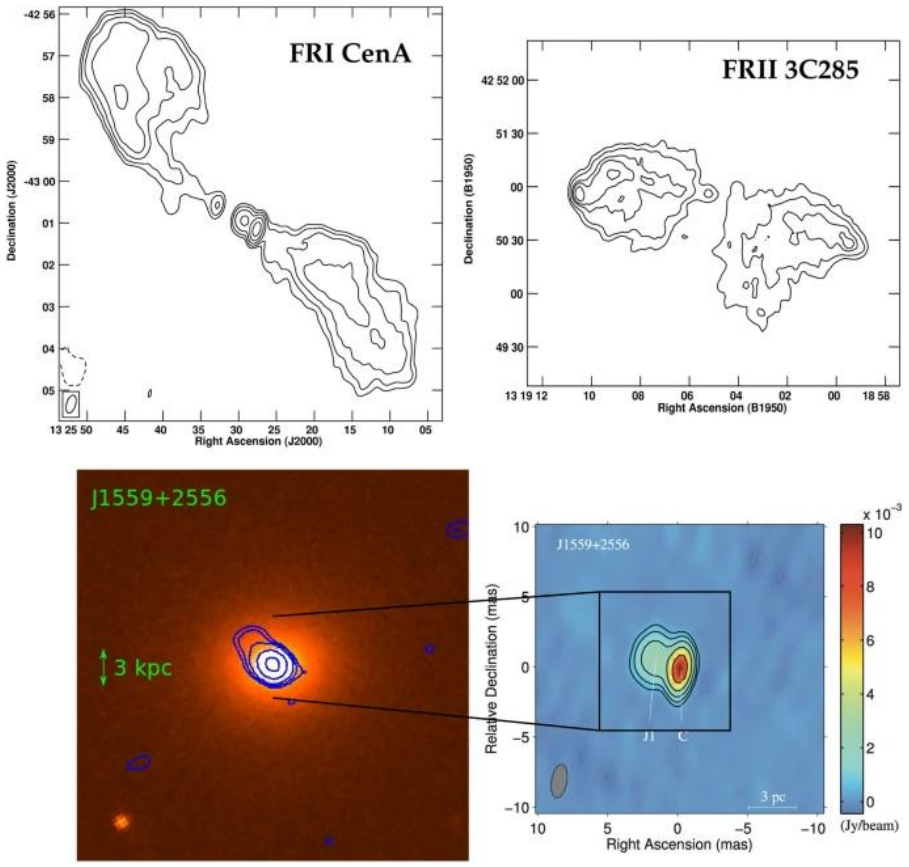

Figure 1.9: Multi-band composite panel of RGs. On the top, the FR I Cen A at 1.4 GHz (Burns et al., 1983) and the FR II 3C 285 at 1.4 GHz (Alexander and Leahy, 1987). On the bottom is show an FR 0: The left panel displays the r-band SDSS image of the host with the blue VLA 4.5 GHz radio contours (Baldi et al., 2019a). The right panel represents the high-resolution zoom on the radio core on the scale of 3 pc (Cheng and An, 2018). Image credit: Baldi (2023).

lower than FR Is at the same [O III]λ5007 luminosity, implying low jet efficiency. X-ray observations reveal hard, low-luminosity spectra typical of advection-dominated accretion flows (ADAF, Torresi et al. 2018), unlike the luminous thermal components of FR IIs/HERGs. The detection of gamma-rays in a few FR 0s (e.g., Grandi et al. 2016; Paliya 2021) suggests they can still accelerate particles to high energies, likely via compact jets (Baldi et al., 2019b).

Environmental studies show that FR 0s typically reside in moderately rich group-scale halos, though a significant fraction are found in denser cluster environments (Capetti et al., 2020b). Compared to FR Is, they are somewhat more commonly associated with lower-richness groups, suggesting that environment may play a role in limiting jet development or influencing AGN triggering. Nevertheless, their host galaxy properties—stellar mass, morphology, and gas content—are similar to those of FR Is, arguing against environmental differences as the sole explanation for their compactness.

Despite their small-scale jets, FR 0s may still drive feedback. X-ray observations (e.g. Ubertosi et al. 2021) have revealed cavities and cold fronts in some FR 0 hosts, confirming jet-induced heating can affect the host and surrounding medium, potentially regulating star formation, and the dominance of the global kinetic energy budget for the most massive galaxies (Igo and Merloni, 2025).

To date, two main models explain FR 0s: (1) the static scenario, where intrinsic factors (low black hole spin, weak magnetic flux, jet composition) limit jet growth; and (2) the dynamic scenario, where jets are short-lived, intermittent, or disrupted by the interstellar medium (ISM). A hybrid view may be needed to encompass the observed diversity.

In summary, FR 0s challenge standard AGN unification models. Their compactness is likely intrinsic, not due to orientation, and reflects either inefficient jet production or transient jet activity. FR 0s offer a unique window into low-luminosity AGN feedback and the physics of short-lived or suppressed radio-jet activity in massive galaxies.

2

The Sample

The aim of this thesis is to investigate the nuclear and extended emission in a sample of 32 FR 0 radio galaxies, with the goal of gaining insight into the physical processes that govern their jet mechanisms, their compact nature, and the extended emission found in a minority of cases.
This project represents a follow-up to the studies by Baldi et al. (2019a) and Capetti et al. (2020a), all of which rely on data drawn from a common source: the FR 0s catalogue known as FR0CAT, compiled by Baldi et al. (2018), which we briefly introduce below.

2.1 FR0CAT

FR0CAT represents the third entry in a series of studies focused on the low-power end of radio galaxies in the nearby Universe. The first paper focused on 219 FR I sources (Capetti et al., 2017b), the second explored the properties of 122 FR IIs (Capetti et al., 2017a), and then FR0CAT focuses on the FR 0s, selecting a sample of compact radio sources from the catalogue of 18,286 objects compiled by Best and Heckman (2012). This catalogue was constructed by cross-matching data from the NVSS, FIRST, and SDSS surveys, and contains mostly RL-AGN, with a possible minor contribution from RQ-AGN, as noted by Baldi and Capetti (2010).

To identify the FR 0s sample, three main criteria were applied: (1) a redshift $z \leq 0.05$ to ensure adequate spatial resolution, (2) a maximum positional offset of $2''$ between the optical and radio positions, and (3) a minimum FIRST flux density of 5 mJy to allow for reliable size measurements. These constraints resulted in a sample of 191 sources.

Subsequently, they visually inspected the FIRST radio images to exclude sources with clearly extended emission, retaining only those whose deconvolved major axis was smaller than $4''$, i.e., sources with an observed major axis under $6''.7$, which corresponds to a projected linear size of ~ 2.5 kpc at $z = 0.05$. At the end of the selection process, a total of 104 compact radio galaxies were classified as FR 0s, all exhibiting LERG-like optical spectra, with the exception of four sources whose spectral features were more consistent with those of HERGs.

Some other defining properties of the FR0CAT sample include 1.4 GHz radio luminosities in the range 10^{38}–10^{40} erg·s^{-1}, a predominant fraction (86%) of hosts being massive ETGs with an absolute r-band magnitudes typically between $-23 \lesssim M_r \lesssim -21$, and an estimated[1] BH masses span from 10^8 to $10^9\, M_\odot$. While a few outliers deviate

[1]From the stellar velocity dispersion $\sigma_\star$ and the relation of Tremaine et al. (2002).

from these general trends, the overall distributions are illustrated in the histograms of Figure 2.1.

To address the many open questions surrounding the nature of FR 0s, various studies have made use of the FR0CAT sample. As mentioned at the beginning of this chapter, this thesis builds on two foundational works, which will be briefly introduced below along with the two Projects that represent a direct follow-up.

2.1.1 Project 1

Capetti et al. (2020a) investigated the low-frequency radio properties of 66-FR 0s, which corresponds to the complete subset of sources contained in FR0CAT that is visible in the sky region observed by LOFAR at 0.145-GHz. While the majority of the sources exhibit compact morphologies, 12 sources show resolved extended emission typically associated with jetted morphologies. Notably, about 20% of the sources have steep spectra ($\alpha \geq 0.5$), suggestive of confined extended emission within the LOFAR resolution limits.

To further investigate the spectral properties of the sources with extended emission, five of the most extended FR 0s among the twelve resolved by LOFAR were randomly selected and observed with the S-band of the VLA at 3.0 GHz. These five sources, which form this thesis *Project 1*, are stored inside two NRAO proposals — 20A-487 and 21A-001 — with a total approved time of 3 and 5 hours, respectively, under the principal investigator (PI) Ranieri D. Baldi.

These five sources were observed through the VLA C-configuration, which offers a maximum baseline of 3 km. Given a central frequency of 3 GHz (S-band), the synthesised beamwidth[2] $\theta_{\rm HPBW}$ is estimated at ~ 7 arcsec, while the detectable largest angular scale (LAS) structure is approximately 490 arcsec[3], which is more than enough for this sample, well within the 100 kpc-scale. This ensures our sources are all perfectly observable within the VLA field of view, allowing us to create spatially resolved radio maps and better characterise their resolved structures through the spectral index.

Through the spectral analysis of the extended emission, we aim to assess the physical origin and evolutionary stage of the jets. The detection of ultra-steep ($\alpha \gtrsim 1.2$) spectral index in the extended components would suggest the presence of an aged plasma, remnants of a past jet activity that has since ceased. In contrast, a steep spectral index ($\alpha \sim 0.6 - 0.8$) would imply that the emission originates from currently weak or slowly advancing jets, incapable of forming the large-scale morphologies characteristic of classical FR I or FR II radio galaxies. Disentangling these scenarios is crucial to understand the life and duty cycles of RL-AGNs, particularly within the FR 0s population.

2.1.2 Project 2

Baldi et al. (2019a) investigated a sub-sample of 18 randomly selected sources from the FR0CAT catalogue, conducting VLA observations at 1.5, 4.5, and 7.5 GHz aimed at studying the nuclear spectral properties and the presence of resolved kpc-scale jets.

[2]For an untapered map produced from a full 12 hour synthesis observation of a source which passes near the zenith.

[3]These numbers are taken from National Radio Astronomy Observatory (NRAO).

The sample is mostly dominated by the core emission and displaying a set of properties consistent to a scaled-down version of FR Is. However, despite achieving subarcsecond resolution, corresponding to $\sim 100-300$ pc, the majority of sources remained unresolved and only four exhibited evidence of larger-scale structures. The sample studied by Baldi et al. (2019a) has 13 sources in common with the study of Capetti et al. (2020a).

To expand the statistical significance of the initial 18 FR 0 sources, proposal 19A-082 (PI: Ranieri D. Baldi) was awarded 14 hours of observational time. This program targeted an additional 27 FR 0s[4] from the FR0CAT sample, which constitute *Project 2* of this thesis. Therefore, the aim of this project is to revisit and expand the analysis conducted by Baldi et al. (2019a), and generalize their findings across a broader and statistically more significant sample of sources.

Following an observational strategy similar to Baldi et al. (2019a), the targets were observed in both the L and C bands, with exposure times equally divided between them. The L-band setup used the standard 1 GHz bandwidth centred at 1.5 GHz. For the C band, a custom configuration was used, by splitting the available 2 GHz bandwidth into two 1 GHz subbands centred at 4.5 GHz (C1) and 7.5 GHz (C2). This customisation grants a better representation of the core spectral emission properties at high frequencies. Both the L and C bands contain 16 SpWs each, consisting of 64 channels with a width of 1 MHz. Observations for each source lasted approximately 10 minutes in both the L and C bands, interspersed with 2-4 minute scans of phase calibrators. The flux density calibrator 3C 286 was observed for about 5-7 minutes.

The characteristics of the proposals are summarised in Table 2.1, while the main properties of the 32 sources of this thesis are shown in Table 2.2. We also show the distributions of some generic quantities (redshift, absolute magnitude, BH mass, [O III] line luminosity) of the Projects, compared to the whole FR0CAT sample, in Figure 2.1. Additionally, to better frame this thesis sources, we present them through their optical images in Figures 2.2, 2.3 and B.1, to which have been superimposed the radio isophotes of their 0.145-GHz LOFAR maps.

Project	**Proposal**	**N**	**Array**	**Bands**	**Freq** [GHz]	**Chan**	$\mathbf{\Delta\nu}$ [GHz]
1	20A-487	1	C	S	3.0	16	2.0
	21A-001	4	C	S	3.0	16	2.0
2	19A-082	27	A	L	1.5	16	1.0
				(C1+C2)	(4.5, 7.5)	(16+16)	1.0, 1.0

Table 2.1: Summary of VLA observational proposals. In the second row of the second Project, the values in brackets indicate the two VLA-C sub-bands (C1 and C2), explicitly listed since only half of the 4 GHz C-band was used and referring to the nominal 6 GHz central frequency would be misleading, as it lies outside the observed ranges (4–5 GHz and 7–8 GHz). Column description: (1) Project of this thesis; (2) NRAO proposal ID; (3) number of sources observed; (4) VLA array configuration; (5) spectral band of the VLA; (6) observed central frequency; (7) number of spectral channels, (8) bandwidth in GHz.

[4]Randomly selected by the VLA scheduler within the FR0CAT catalogue, with the exception of the 18 previously selected by Baldi et al. (2019a).

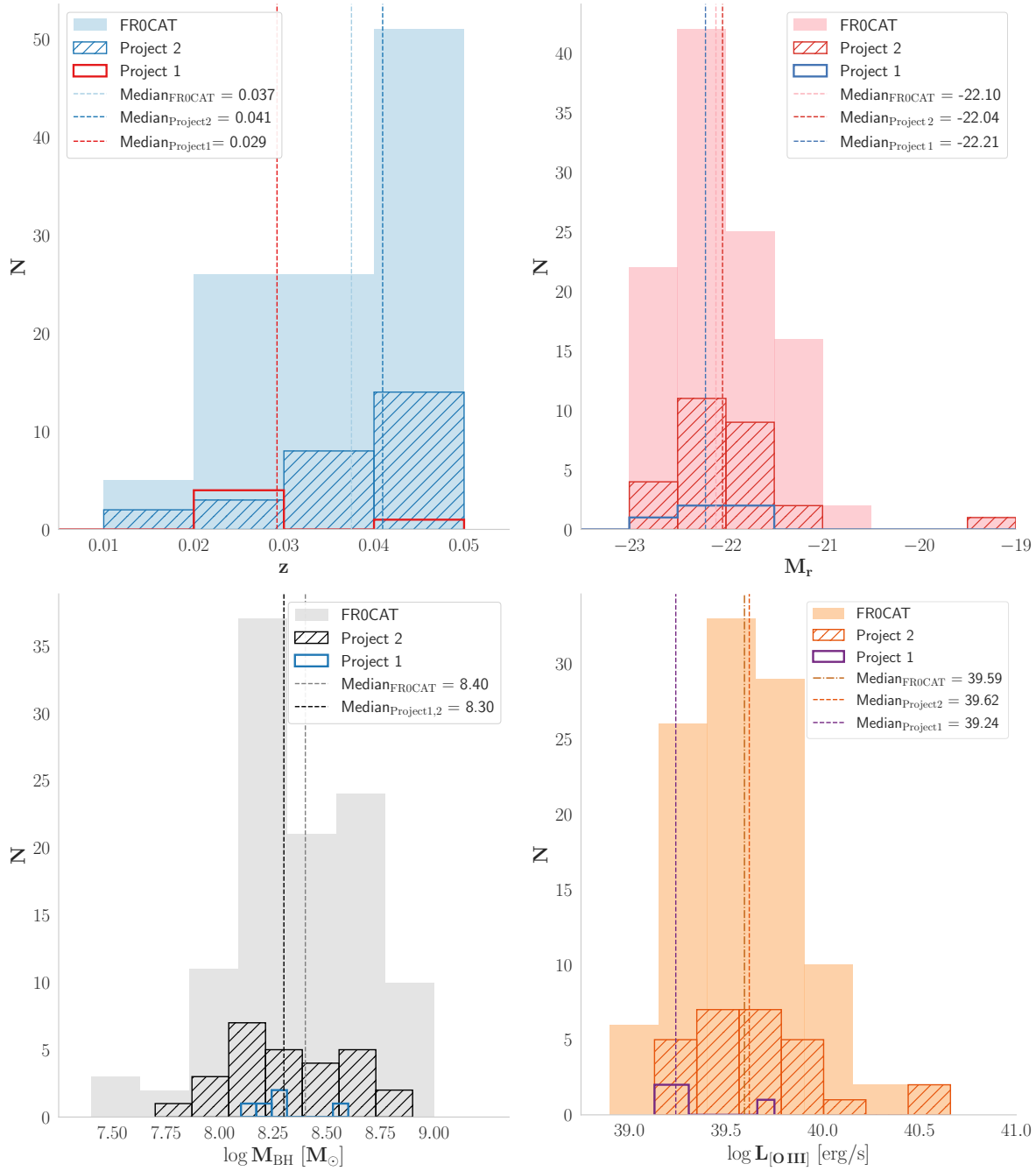

Figure 2.1: Distributions of redshift (top left), absolute r-band magnitude (top right), black hole mass (bottom left), and [O III] line luminosity (bottom right) for the 32 sources analyzed in this thesis – divided into Project 1 (empty histograms) and Project 2 (hatched histograms) – compared with the 104 sources from the FR0CAT catalogue. The filled histograms representing the FR0CAT sample are based on data from Baldi et al. (2018).

SDSS	Name	z	D_L	M_r	$L_{[NVSS]}$	$L_{[OIII]}$	M_{BH}
J080716.58+145703.3	CGCG 088-035	0.030	130.6	-21.88	38.93	39.13	8.3
J091039.92+184147.6	NGC 2774	0.029	128.8	-22.21	39.14	39.19	8.1
J091601.78+173523.3	NGC 2794	0.029	128.7	-22.50	38.86	39.75	8.3
J104403.68+435412.0	UGC 05845	0.025	110.9	-21.83	38.84	39.28	8.2
J172215.41+304239.8	CGCG 170-018	0.047	208.4	-22.93	38.78	39.24	8.6

SDSS	Name	z	D_L	M_r	$L_{[NVSS]}$	$L_{[OIII]}$	M_{BH}
J010852.48−003919.4	-	0.045	204.5	-21.47	38.89	39.77	8.30
J011204.61−001442.4	UGC 00753	0.044	199.5	-21.68	39.09	39.40	8.30
J011515.78+001248.4	GIN 061	0.045	203.6	-22.01	39.48	39.63	8.50
J075354.98+130916.5	-	0.048	220.1	-22.36	38.77	39.47	8.90
J080716.58+145703.3	CGCG 088-035	0.030	130.6	-21.88	38.93	39.13	8.30
J084701.88+100106.6	-	0.048	225.25	-22.20	39.28	39.44	8.50
J101806.67+000559.7	-	0.048	225.5	-21.75	39.07	40.66	7.70
J102403.28+420629.8	-	0.044	200.9	-21.86	38.60	39.28	8.20
J104811.90+045954.8	NGC 3386	0.034	158.3	-22.34	39.30	39.96	8.10
J104852.92+480314.8	UGC 05915	0.041	188.35	-22.18	39.05	40.62	8.10
J105731.16+405646.1	NGC 3468	0.025	115.05	-22.34	38.98	39.46	8.70
J112029.23+040742.1	CGCG 039-127	0.050	230.9	-22.53	38.81	39.95	8.40
J130837.91+434415.1	NGC 5003	0.036	164.35	-22.63	39.41	40.06	8.60
J133042.51+323249.0	-	0.034	155.1	-21.68	38.85	39.79	7.90
J134159.72+294653.5	-	0.045	207.15	-22.10	38.87	39.62	8.10
J135036.01+334217.3	NGC 5318	0.014	65.7	-21.46	38.84	39.52	8.10
J142724.23+372817.0	IC 4435	0.032	147.8	-22.08	38.87	39.27	8.80
J143312.96+525747.3	MCG +09-24-014	0.047	217.3	-21.59	39.09	39.72	8.40
J152151.85+074231.7	NGC 5920	0.045	205.7	-22.66	38.90	39.24	8.60
J154147.28+453321.7	UGC 09981	0.037	167.4	-22.04	38.62	39.59	8.30
J154426.93+470024.2	CGCG 250-006	0.038	172.7	-22.55	38.94	39.80	8.60
J154451.23+433050.6	CGCG 222-050	0.037	167.45	-22.48	38.73	39.63	8.30
J155953.99+444232.4	B3 1558+448	0.042	190.75	-21.94	39.56	39.84	8.00
J160641.83+084436.8	-	0.047	218	-22.21	38.86	39.69	8.00
J161256.85+095201.5	NGC 6081	0.017	76.8	-21.55	38.33	39.35	8.20
J162944.98+404841.6	-	0.029	131.25	-19.05	38.36	39.21	8.60
J164925.86+360321.3	CGCG 197-016	0.031	142	-21.68	38.61	39.45	8.10

Table 2.2: Summary of the main properties of the 5 sources in Project 1 (top Table) and the 27 sources in Project 2 (bottom Table). Column description: (1) Source name in SDSS, hereafter referred with the short form (for example: J010852.48−003919.4 → J0108-00); (2) other name; (3) redshift; (4) luminosity distance [Mpc]; (5); (6) SDSS DR7 r band absolute magnitude; (7) logarithm of the [OIII] line luminosity [erg s^{-1}]; (8) logarithm of the black hole mass [solar units]. Data of columns 5-8 are taken from Baldi et al. (2018).

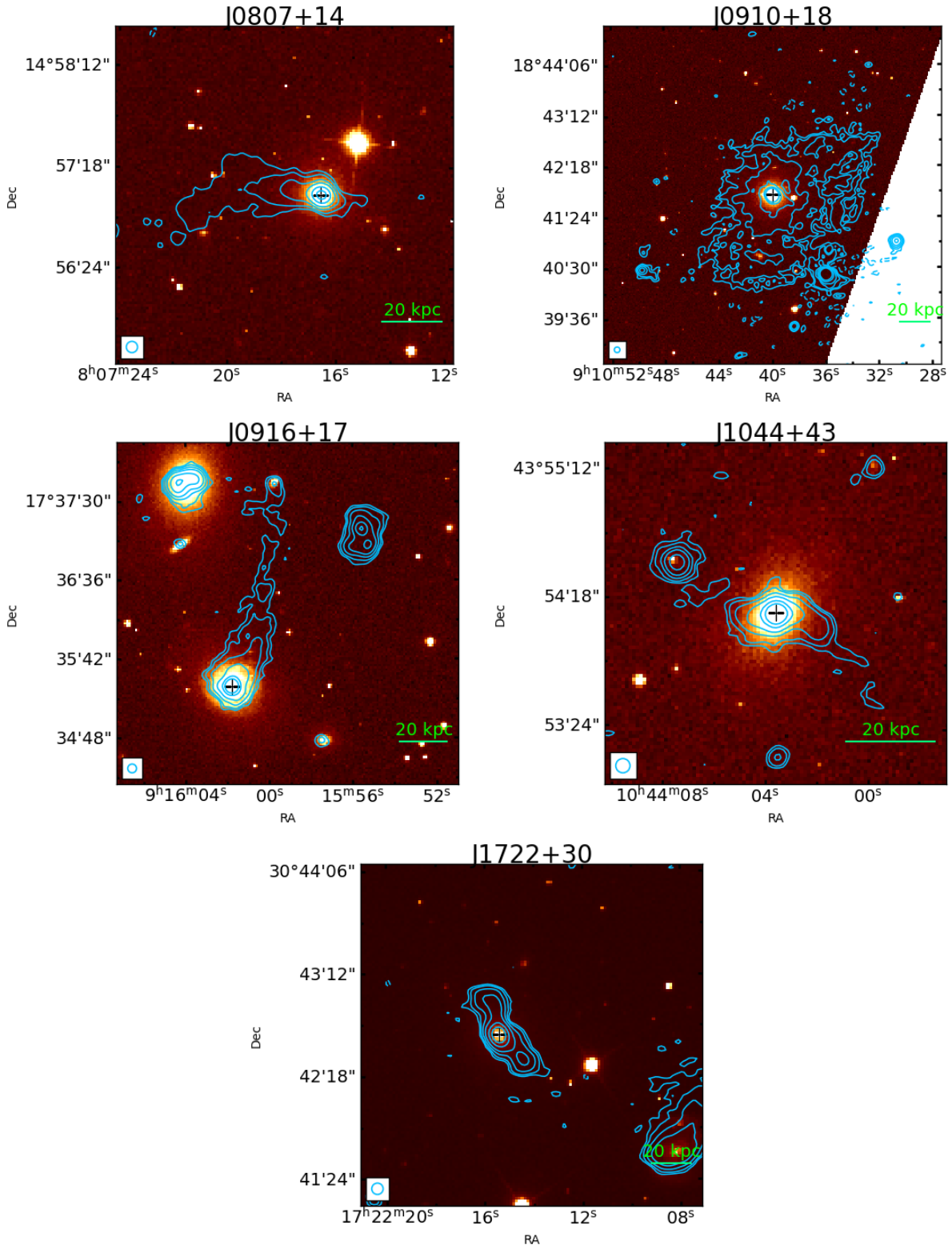

Figure 2.2: SDSS optical images of the host galaxies associated with the five FR 0s of Project 1, overlaid with LOFAR radio contours at 0.145 GHz. The LOFAR beam of $6'' \times 6''$, is shown in the bottom-left corner of each panel, while the black cross marks the coordinate centre of the host galaxy. The contour levels follow the sequence [-3, 3, 5, 10, 20, 50, 100]σ, where σ is the local rms of [7.8, 10.6, 13.1, 8.5, 12.0]$\cdot 10^{-5}$ Jy$\cdot$beam^{-1}, respectively. In `J0910+18`, the optical map does not fully cover the field of view, resulting in a region where only the white radio background is displayed.

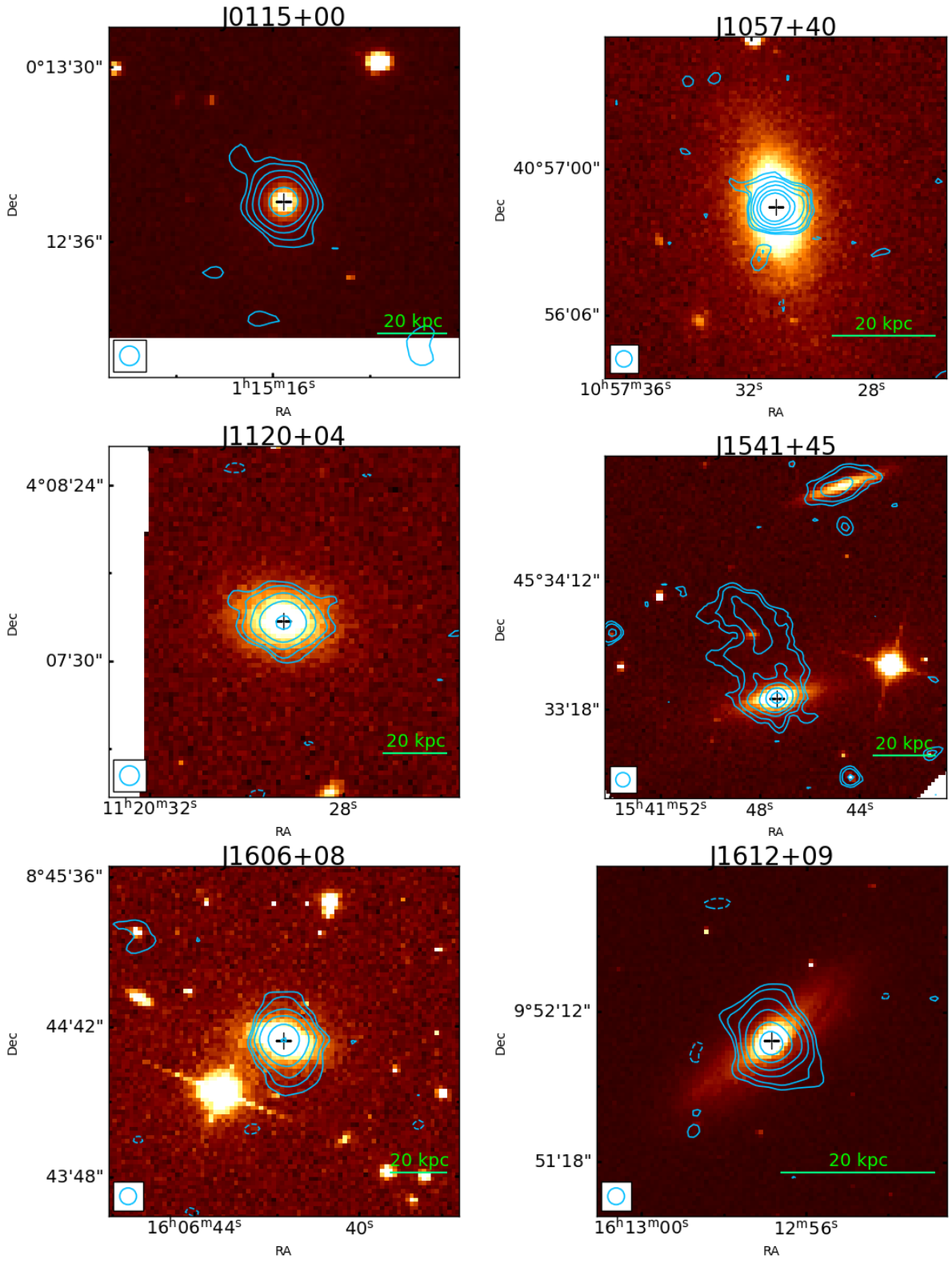

Figure 2.3: Selection of SDSS optical images of the host galaxies associated with the 27 FR 0s of Project 2, overlaid with LOFAR radio contours at 0.145 GHz. The LOFAR beam of $6'' \times 6''$, is shown in the bottom-left corner of each panel, while the black cross marks the coordinate centre of the host galaxy. The contour levels follow the sequence [-3, 3, 5, 10, 20, 50, 100]σ, where σ is the local rms of [18.4, 5.9, 14.6, 7.2, 14.3, 18.3]$\cdot 10^{-5}$ Jy$\cdot$beam^{-1}, respectively. In some cases, the optical maps do not fully cover the field of view, resulting in regions where only the white radio background is displayed. The remaining images are shown in Figure B.1.

3

Radio astronomy and interferometry

3.1 Radio emission

Radio astronomy was officially born in May 1933, when Karl Jansky discovered radio waves emanating from the center of our Galaxy. This emission was later identified as synchrotron radiation (Alfvén and Herlofson, 1950), based on its power-law spectrum and high degree of polarization, features discussed in Section 1.1.4. In 1953, Shklovsky proposed that the radio and optical emission from the Crab Nebula was due to synchrotron processes—a hypothesis later confirmed by polarization measurements (Dombrovsky 1954; Vashakidze 1954). This was instrumental in confirming that the optical jet of M87, a major radio source identified in 1949 (Bolton et al. 1949), was also polarized and due to synchrotron emission.

The field of radio astronomy expanded rapidly during the 1960s, driven by the development of increasingly powerful radio telescopes and the release of the first catalogs (e.g. 3C Catalogue Bennett 1962a, Parkes Catalogue Bolton et al. 1964) dedicated specifically to radio galaxies. However, since most galaxies emit some level of radio radiation, a more precise classification was required. Consequently, radio galaxies came to be defined as galaxies that emit significantly more radio power than typical systems like the Milky Way.

Radio astronomy is the study of natural radio emission from celestial sources. The range of radio frequencies or wavelengths is set by the atmospheric opacity, and it ranges in a very broad logarithmic interval of almost five decades, from $\sim$ 10 MHz to $\sim$ 1 THz. This type of emission is very important because almost every object emits radio waves at some level, and it is possible to have very complete surveys, since the radio emission easily penetrates the interstellar dust and Compton-thick layers of neutral gas; this results in a small number of obscured sources.

Because the radio band is so broad, a wide variety of radio telescopes and observing techniques are needed to effectively cover the *radio window* (Figure 3.1); which represents the range of wavelengths in which there is relatively little radiation absorption by atmospheric gases. The partially absorbing atmosphere does not just attenuate incoming radio radiation, it also emits radio noise that can seriously degrade the sensitivity of ground-based observation, which are then limited in optical, near infrared (NIR) and radio bands. The physical processes that otherwise limit the atmospheric window are the following:

- At high frequencies, mid infrared (MIR) radiation is absorbed by the vibrational transition of atmospheric molecules (CO_2, O_2, H_2O);
- Lower energy rotational transitions of atmospheric molecules define the interval between far infrared (FIR) and ~ 1 THz;
- Below ~ 300 MHz the variable ionospheric refraction increasingly degrades observations, and for frequencies $\nu < 10$ MHz the radio component is usually reflected back into space by Earth's ionosphere.

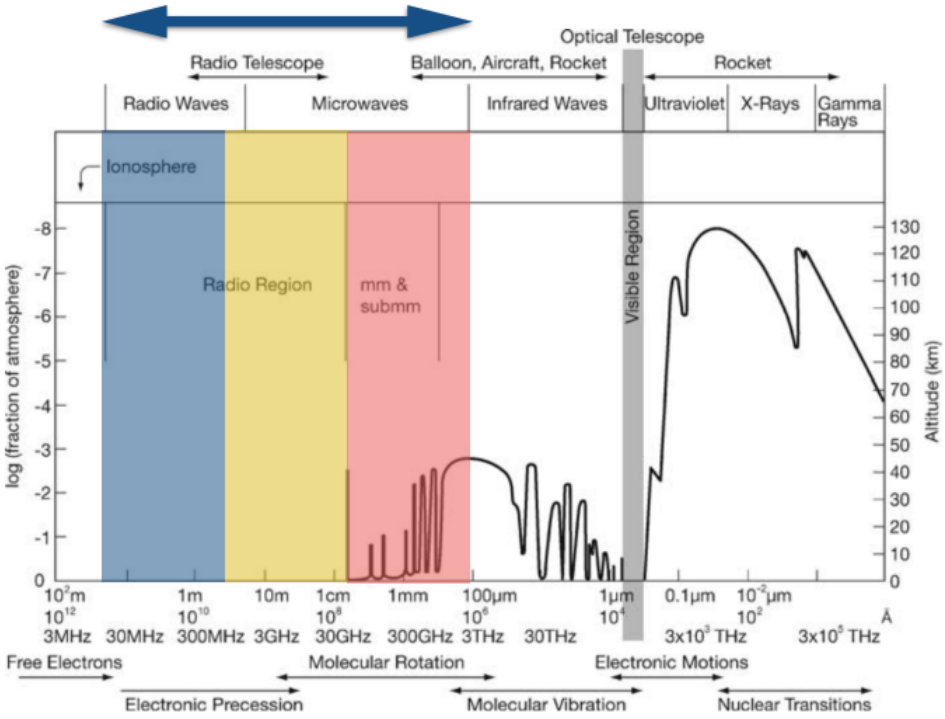

Figure 3.1: Atmospheric window. The small gray stripe is where the atmosphere is completely transparent to ground-based observations. Image credit: John McKean (2015).

3.2 Single-dish telescopes

A basic radio telescope typically consists of a single parabolic dish that collects incoming wavefronts in phase and focuses them onto a receiver, commonly a dipole antenna, which converts the freely propagating electromagnetic radiation into guided signals.

When a point source is observed, its signal is modulated by the *power pattern* of the telescope, which basically describes the angular distribution of the radiation power, thus how sensitive a telescope is to signals coming from different directions. It is essentially the square of the voltage response (i.e. the electric field pattern), and from its shape derives the concept of angular resolution. In the right plot of Figure 3.2 it is emphasized the *main lobe* of the pattern, which indicates the direction in which the maximum response of the telescope lies. In an ideal case, the main lobe would be the only detected signal from the telescope. However, because of diffraction and the finite size of the dish, the response

of the telescope also shows multiple *side-lobes* [1]: weaker, ring-like lobes surrounding the main one containing unwanted signals from off-target directions.

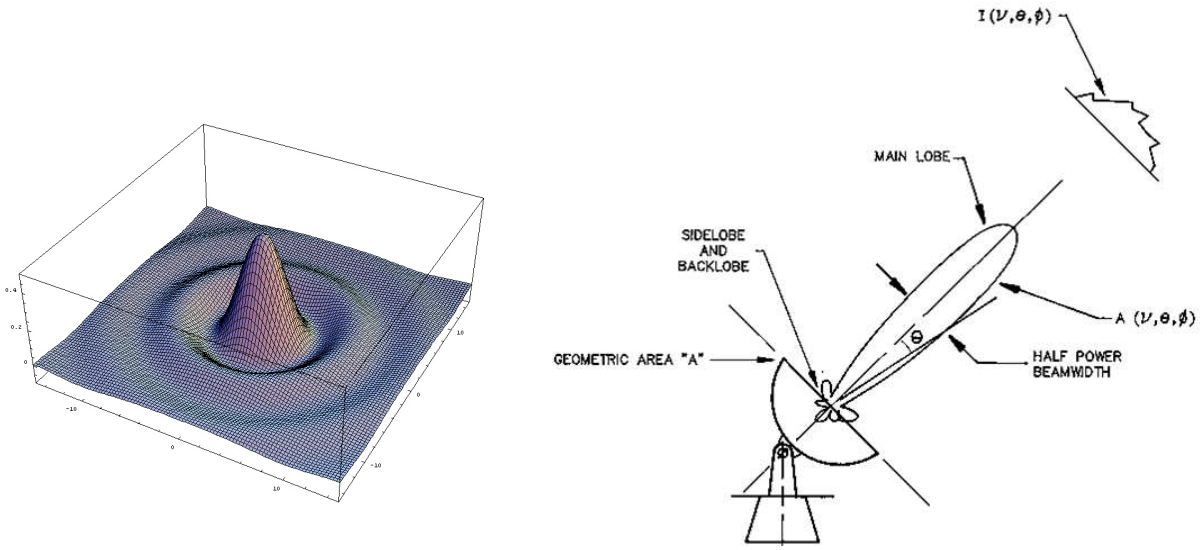

Figure 3.2: (left) 3D representation of an Airy pattern, image credit: Rubén (2009). (right) Longitudinal section of the Beam in polar coordinates, image credit: Fanti (2007).

Single-dish radio telescopes present some disadvantages, such as a relatively low angular resolution $\theta_{\rm BW}$ imposed by the fixed diameter of the antenna, which results in $\theta_{\rm BW} \sim 0.89\frac{\lambda}{D}$, where D is the antenna diameter and λ the wavelength of the observation. The large beamwidth, combined with a limited field of view (FoV) $\theta_{\rm FOV} \sim 1.22\frac{\lambda}{D}$ and a fixed collecting area $\mathrm{A} \lesssim \pi D^2/4$, highlight significant limitations of single-dish telescopes, especially for deep, high-resolution observations and morphological[2] studies.

These challenging problems and the need for achieving greater resolutions in observations lead to the natural birth of the interferometry.

3.3 Interferometry

Radio interferometry, strictly speaking, is a synthetic aperture imaging technique used in radio astronomy to combine signals from several radio telescopes to generate high-resolution images of celestial objects. Over the last decades, several radio-interferometric facilities have been developed, including the Very Large Array (VLA; Perley et al. 2011) and, more recently, the Australian Square Kilometre Array Pathfinder (DeBoer et al. 2009), the LOw Frequency ARray (LOFAR; van Haarlem et al. 2013), the Australian Square Kilometre Array Pathfinder (ASKAP; Hotan et al. 2021).

The immediate advantage of using an interferometric array, instead of a single-dish telescope, is a substantial improvement in the added resolution, now given by $\theta_{BW} \approx \lambda/b_{max}$, where $b_{max} \gg D$ is the maximum baseline available, i.e. the distance between two antennas in the array. The missing short spacings ($b < D$) can be recovered through

[1] The beam of a perfect paraboloid usually has the first sidelobe intensity at few percent of the peak, while for an interferometer (see Section 3.3) it can be as high as $\sim 15\%$.

[2] According to the Rayleigh criterion, two sources can only be resolved if their angular separation exceeds the beamwidth.

complementary single-dish observations, provided that the dish diameter exceeds the minimum interferometric baseline (i.e. $D > b_{min}$). For example, the 100-meter Green Bank Telescope (GBT) can supply measurements for baselines shorter than 25 meters, which are inaccessible to the 25-meter dishes of the VLA.
The simplest interferometer is a pair of radio telescopes whose voltage outputs are correlated, thus multiplied and averaged in time, as shown in the left panel of Figure 3.3.

Electromagnetic waves hit the antenna plates and are converted into two equal currents V_1 and V_2, which are amplified and then corrected for the geometric delay $\tau_g = b\cos(\theta)/c$ so that the phase can be preserved. The response R of a two-element interferometer with directive antennas, also called *dirty beam*, is the cosine function multiplied by the product of the voltage patterns of the individual antennas:

$$R =< V_1 V_2 >= \frac{V^2}{2}\cos(\omega\tau_g) \tag{3.1}$$

The output amplitude of the correlator $V^2/2$ is proportional to the flux density F of the point source multiplied by the effective collecting areas of the two antennas $A_{1,2}$: $V^2/2 \propto F(A_1, A_2)^{1/2}$.

If individual antennas were isotropic, the interferometer point source response would be a cosine function with all lobes at the same height (Figure 3.3, *right*), which clearly is not a good power pattern since we cannot distinguish a main lobe; like in the single-dish case.

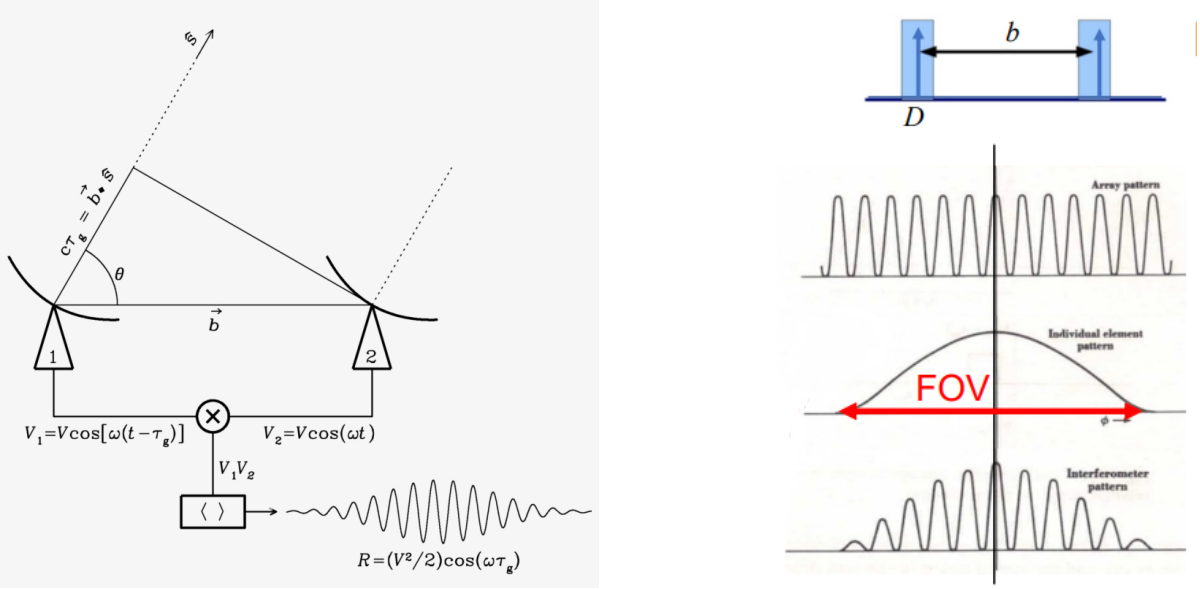

Figure 3.3: (Left) Components of a two-element quasi monochromatic multiplying interferometer where $\vec{s}$ is the unit vector in the direction of a distant point source, $\vec{b}$ is the baseline vector and R is the interferometer response. (Right) In case of identical antennas, the response is the power pattern of the individual antennas ($\sin^2(c)$) and is called the *primary beam* of the interferometer, which defines the FoV ($\theta_{FoV} \approx \lambda/D$) of the interferometer. Images credit: Condon and Ransom (2016).

The correlator response varies sinusoidally as the Earth rotation changes the source direction relative to the baseline vector. These sinusoids are called *fringes* and have a

phase[3]:

$$\phi = \omega\tau_g = 2\pi\frac{b\cos(\theta)}{\lambda} \tag{3.2}$$

The angular resolution of the fringes, or *synthesized beam*, is given by

$$\theta_{BW} \sim \frac{1}{u} \qquad \text{with } u = \frac{b\sin(\theta)}{\lambda} \tag{3.3}$$

Improving the instantaneous point source response pattern of an interferometer fundamentally requires more baselines, which allows for more combinations between long and short baselines. This is crucial, as different observations focus on different types of objects, thus:

- Longer baselines have a smaller angular fringe spacing, and they are more sensitive to compact objects, with the longest baseline b_{max} defining the angular resolution $\theta_{BW} \approx \lambda/b_{max}$;
- Shorter baselines will instead be more sensitive to extended objects since their angular fringe spacing is larger, so the shortest baseline b_{min} defines the maximum recoverable scale $\theta_{BW,max} \approx \lambda/b_{min}$.

An interferometer with N antennas contains $N(N-1)/2$ pairs of antennas, each of which is a two-element interferometer, so the instantaneous beam rapidly approaches a Gaussian as N increases, as shown in the left panel of Figure 3.4.

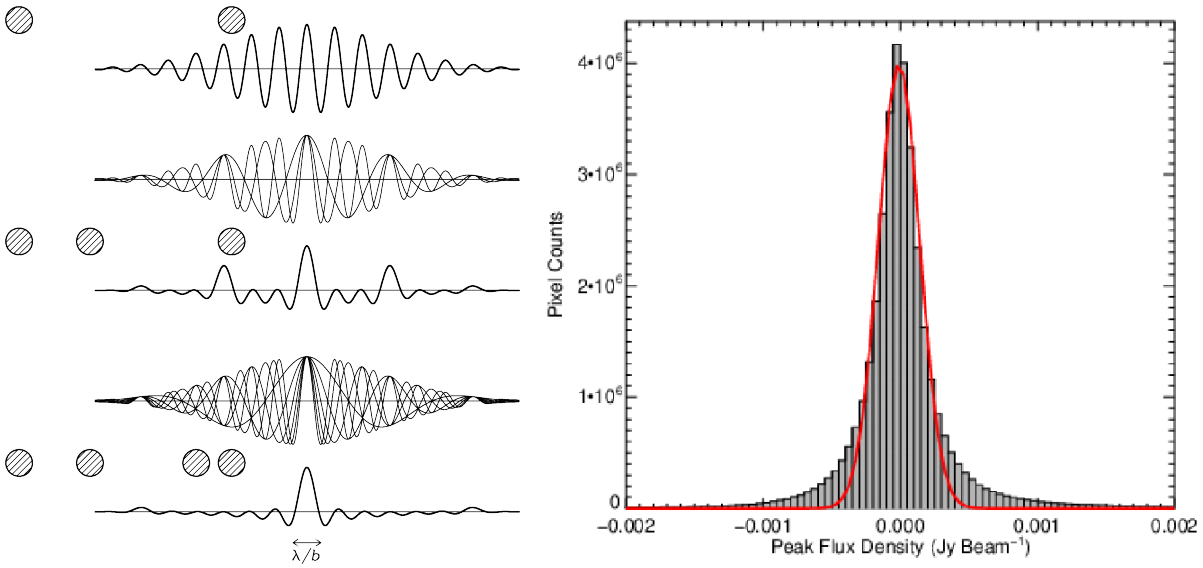

Figure 3.4: (Left) The instantaneous synthesized beam rapidly approaches a Gaussian curve as the number N of the responses of its components (two-element interferometers) increases, but the sidelobes are still significant and there is a negative "bowl" caused by the lack of spacings shorter than the diameter of the individual antenna. Credit: Condon and Ransom (2016). (Right) Typical noise distribution. The red line shows the results of a Gaussian fit to the distribution. Credit: Medina et al. (2019).

[3]We only measure a relative phase, $\omega\tau_g$, which is the only term that survives after the correlation is done. To measure an absolute phase, we need a reference antenna.

The point-source rms noise of an interferometer array of N antennas, which is:

$$\sigma_{rms} = \frac{2kT_{sys}}{A_e[N(N-1)\,\Delta\nu\,\tau]^{1/2}} \tag{3.4}$$

where k is the Boltzmann constant, A_e is the effective area of a single antenna [m^2], $N(N-1)$ the number of unique baselines in the array with N antennas, $\Delta\nu$ is the bandwidth per channel [Hz], τ the integration time [s] and T_{sys} is the system noise temperature, defined as the equivalent temperature of the total noise power present at the output of the receiving system, including contributions from the receiver, sky, ground, and other sources.

The important dependence of Equation 3.4 is given by $\sigma_{rms} \propto T_{sys}(\Delta\nu\,\tau)^{-1/2}$, and so the rms noise is reduced by the square root of the observation time τ and bandwidth. Since the thermal noise arises from the random motion of electrons in a conductor due to thermal agitation, it is statistically characterized by a Gaussian (normal) distribution with zero mean, implying that the fluctuations are equally likely to be positive or negative. This property makes the thermal noise distribution symmetric around zero; as shown in the right panel Figure 3.4.

3.4 Interferometric imaging

In general, if the source is slightly extended with a sky brightness distribution $I_\nu(\hat{s})$ near frequency $\nu = \omega/(2\pi)$, the response in Equation 3.1 is obtained by summing the responses of independent point sources:

$$R_c = \int I(\hat{s}) \cos\left(\frac{2\pi\nu}{c}\vec{b}\cdot\hat{s}\right) d\Omega = \int I(\hat{s}) \cos\left(\frac{2\pi}{\lambda}\vec{b}\cdot\hat{s}\right) d\Omega. \tag{3.5}$$

R_c is the cosine correlator, and it is sensitive only to the even part I_E of an arbitrary brightness distribution, which can instead be written as $I = I_E + I_O$, where I_O represents the odd part of the distribution detected by the response of the sine correlator R_s:

$$R_S = (V^2/2)\sin(\omega\tau_g) = \int I(\hat{s}) \sin\left(\frac{2\pi}{\lambda}\vec{b}\cdot\hat{s}\right) d\Omega. \tag{3.6}$$

Since it is very convenient to treat sines and cosines functions through the Euler's formula[4], it is possible, and preferable, to combine the sine and cosine correlators to obtain the *complex correlator*. The response to a source with brightness distribution $I(\hat{s})$ of the two-element quasi-monochromatic interferometer with a complex correlator is the *complex visibility* V:

$$V \equiv R_C - iR_S = Ae^{-i\phi} = \int I(\hat{s}) \exp\left(-\frac{i2\pi}{\lambda}\vec{b}\cdot\hat{s}\right) d\Omega. \tag{3.7}$$

The visibilities represent the starting point in our analysis, which are complex numbers of amplitude $A = \sqrt{R_C^2 + R_S^2}$ and phase $\phi = \arctan(R_S/R_C)$.
To do imaging, we want to reconstruct the surface brightness $I(\hat{s})$ inside the integral in Equation 3.6. For this purpose, we move to the *uv-plane*, which represents the natural coordinate system for the correlator response and gives the spatial distribution of baselines, in unit of wavelength λ, as seen from the source at infinity. In this plane the

[4] $e^{i\phi} = \cos(\phi) + i\sin(\phi)$.

complex visibility and the brightness distribution are a Fourier pair and can be written as:

$$V(u,v) = \iint I_\nu(l,m) exp[-2\pi i(ul+vm)] dl dm \tag{3.8}$$

$$I_\nu(l,m) = \iint V(u,v) exp[2\pi i(ul+vm)] du dv \tag{3.9}$$

where u,v are the baselines measured in wavelengths units, and l,m can be simply correlated to the right ascension and declination respectively. For each integration time and frequency interval, a single baseline samples a single point in the (u,v) plane[5] by measuring both the amplitude and the phase of the complex visibility. In fact, the receiver is sensitive to a certain frequency band, which is generally divided into N_{spw} spectral windows (spw), which are further subdivided into N_{chan} channels. Therefore, during an observation of total duration T_{tot} and integration time T_{int}, using N_b baselines, the number of visibilities is given by:

$$N_{vis} = 4 \cdot N_b \cdot N_{spw} \cdot N_{chan} \cdot \frac{T_{tot}}{T_{int}} \tag{3.10}$$

In order to fill the uv-plane completely one would require an infinite number of baselines, thus antennas. To overcome this problem, it is clearly not possible to build infinite antennas and recover the perfect brightness distribution by Fourier transform the visibility function. However, an ingenious solution has been developed: the *Principle of Earth Rotation Aperture Synthesis* (Figure 3.5), which takes advantage of Earth rotation to produce an apparent variation of the antenna positions and thus their baselines. In this way, the projected distance of the baselines changes over time during an observation, providing a better *uv*-coverage in the Fourier plane. Increasing the number of visibilities improves the reconstruction of the brightness distribution of the object, therefore the (synthesized/dirty) beam.

3.5 Radio facilities of interest

Over the past few decades, advancements in radio interferometry coupled with large-scale sky surveys have revolutionised our ability to map the radio Universe with unprecedented sensitivity and angular resolution. Several major radio facilities have contributed to this progress, each operating at different frequency ranges and with distinct scientific goals. Here, we have worked on the images produced by the VLA, LOFAR and ASKAP and their relative surveys; and sometimes compared results with the existing literature. This helped us to look at the sources at different frequencies, enriching their broad-band spectrum and radio morphology. We briefly present here the radio telescopes and surveys that were used in this work.

3.5.1 The Karl G. Jansky Very Large Array (JVLA)

The JVLA, or simply VLA, is a 27–element interferometric array with antennas of 25 meters in diameter, arranged along the arms of an upside-down Y (see Figure 3.6, *left*),

[5]The ensemble of the interferometer pairs constitutes the (u,v) coverage, which represents the sampling function, whose Fourier transform is the dirty beam.

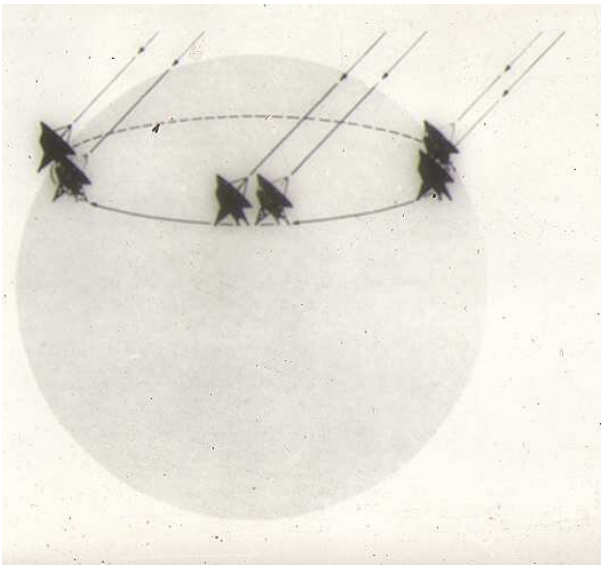

Figure 3.5: Principle of Earth Rotation Aperture Synthesis, where the rotation of the Earth supplies extra coverage in the uv-plane. Credit: Fanti (2007).

which can observe the sky at a wide range of frequencies and angular resolutions. The VLA is located at an elevation of 2100 meters on the Plains of San Agustin in southwestern New Mexico, USA. It was built in the 1960s and underwent a major modernisation between 2010 and 2013, including the replacement of the correlation system, a significant increase in sensitivity, and an expansion of frequency coverage from 1 to 50 GHz. This major renovation became known as the Expanded VLA (EVLA) and was later renamed the Jansky Very Large Array (JVLA) in 2012; to honour the memory and contributions in radio astronomy of Karl G. Jansky.

The telescopes can be moved along a railroad track to form four basic antenna arrangements, called configurations, whose scales vary by the ratios 1 : 3.28 : 10.8 : 35.5 from smallest to largest. These configurations are denoted D, C, B, and A, respectively. The VLA cycles through its four configurations approximately every 16 months, with observing projects ranging from 1/2 hour to several weeks. Additionally, hybrid configurations (BnA, CnB, and DnC) exist to optimise the observation of sources with specific declinations. The VLA antennas are all outfitted with eight receivers (feeders, Figure 3.6, *right*) providing continuous frequency coverage from 1 to 50 GHz in the following observing bands: 1–2 GHz (L-band); 2–4 GHz (S-band); 4–8 GHz (C-band); 8–12 GHz (X-band); 12–18 GHz (Ku-band); 18–26.5 GHz (K-band); 26.5–40 GHz (Ka-band); and 40–50 GHz (Q-band). Additionally, we present below the two main VLA surveys used in this thesis:

1) The Faint Images of the Radio Sky at Twenty-Centimeters (FIRST) is a deep radio survey conducted at 1.4 GHz using the VLA in its B-configuration. From 1993 to 2002, it used 3200 observing hours to cover approximately 10,000 square degrees of the northern sky, offering a high angular resolution of 5 arcseconds and a sensitivity of 0.15 mJy/beam (Becker et al. 1995). The survey has catalogued over 900,000 radio sources, making it an essential dataset for extragalactic radio astronomy. FIRST has been particularly useful for identifying compact radio-loud quasars, tracing the large-scale cosmic web, and uncovering the radio emission properties of star-forming galaxies.

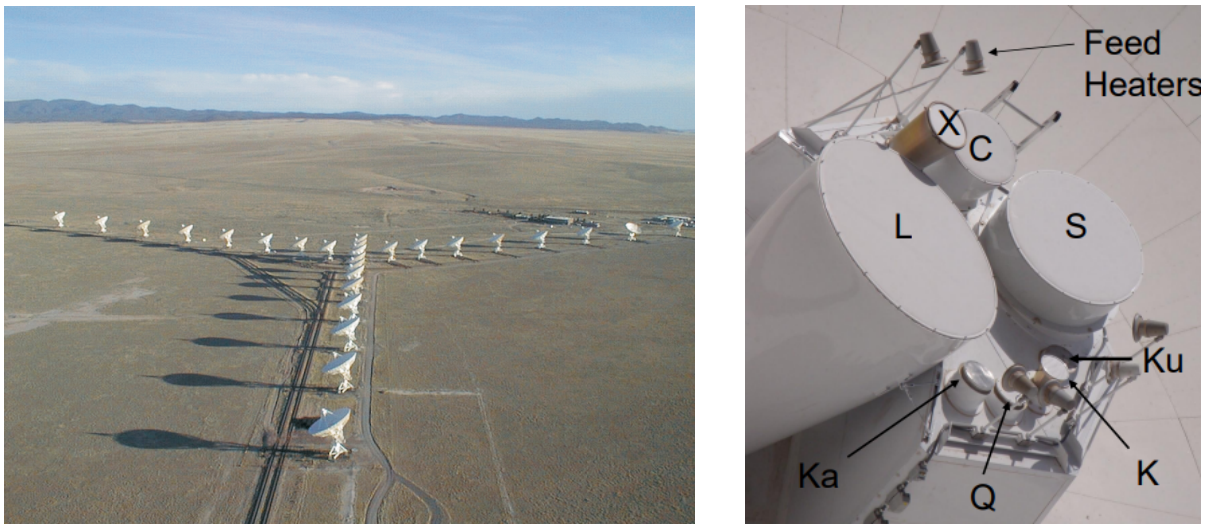

Figure 3.6: (Left) Aerial view of the VLA. (Right) Close-up of the VLA feed system, covering multiple frequency bands for radio astronomy observations. Images credit: NRAO and John McKean (2015), respectively.

It provides high positional accuracy (∼1 arcsecond, White et al. 1997), enabling precise cross-matching with optical surveys such as the SDSS. However, FIRST is not as sensitive to extended radio structures due to a lack of short antennae baselines. As a result, the total radio luminosity of sources that are larger than a few arcseconds will be systematically low (Becker et al. 1995). In extreme cases, some larger radio sources are completely missed, introducing systematic biases into the derived radio source sample.

2) The NRAO VLA Sky Survey (NVSS) was carried out using the D-configuration of the VLA at 1.4 GHz (L-band). From 1993 to 1996, it used 2932 observing hours to covers approximately 82 % of the sky (declinations north of −40°) with a uniform angular resolution of 45 arcsecond, down to a limiting point source flux density of about 5σ, or 2.5 mJy. The survey achieved a typical sensitivity of 0.45 mJy/beam, making it suitable for detecting both compact and moderately extended radio sources (Condon et al. 1998). NVSS data have been extensively cross-matched with optical and infrared catalogues, playing a crucial role in the identification and classification of radio sources in the local and distant Universe. Additionally, the NVSS and FIRST surveys are highly complementary for identifying radio sources associated with nearby galaxies; with the first providing the sensitivity to large-scale radio structures required to detect all of the emission from extended radio sources, while the latter provides the high angular resolution required to reliably identify the host galaxy.

3.5.2 LOFAR

The Low-Frequency Array LOFAR is an interferometric radio telescope designed to observe the low-frequency radio sky with unprecedented sensitivity and resolution. Operated by ASTRON in the Netherlands, LOFAR consists of thousands of dipole antennas distributed across Europe, with a core in the Netherlands. It operates primarily in two frequency bands: 10–90 MHz (Low Band Antennas, LBA), and 110–240 MHz (High

Figure 3.7: The large circular island encompasses the six core stations that make up the Superterp, the heart of the LOFAR core. Three additional LOFAR core stations are visible in the upper right and lower left of the image. Each of these core stations includes a field of 96 low-band antennas and two sub-stations of 24 high-band antenna tiles each. Image credit: van Haarlem et al. (2013).

Band Antennas, HBA). The unique architecture of LOFAR enables observations at angular resolutions down to ∼0.3 arcseconds when using international baselines (Moldón, J. et al. 2015), a resolution which, in the radio band, has for many decades only been achievable at high frequencies. Its field of view depends on frequency, but typically spans several degrees, with the HBA array providing a field of view of approximately 5° at 150 MHz, while the LBA offers a broader field of view of 20° at 60 MHz (van Haarlem et al. 2013). This capability has proven instrumental in performing large-area sky surveys and studies of rare class of sources such as probing ultra-steep spectrum radio sources, studying radio emission from cosmic ray interactions, and mapping large-scale magnetised structures in galaxies and clusters. In this case, we also present the main LOFAR survey:

The LOFAR Two-metre Sky Survey (LoTSS) is an ambitious project designed to image the entire northern sky with 3168 pointings of eight hours each in the frequency range between 120 and 168 MHz (van Haarlem et al. 2013). Using the LOFAR HBA array, LoTSS achieves a typical angular resolution of 6 arcseconds and a median sensitivity of ∼83 μJy/beam (∼ 0.10 mJy/beam), as demonstrated in its second data release (LoTSS-DR2, Shimwell, T. W. et al. 2022), which covers approximately 27% of the northern sky (∼ 5700 square degree) and includes over 4.4 million radio sources. The first LoTSS data release (DR1; Shimwell, T. W. et al. 2019), instead, presented the results obtained from observations of 424 square degrees in the HETDEX Spring Field. The flux density scale was adjusted to ensure consistency between the two releases (Hardcastle et al. 2016 for further details).

3.5.3 ASKAP

ASKAP is a radio interferometer operated by CSIRO in Western Australia, consisting of 36 12-meter dishes spread across six square kilometres, and equipped with phased-array feeds (PAFs) on top of each antenna, allowing a large instantaneous field of view ($\sim 30\,\mathrm{deg}^2$, Hotan et al. 2021) and high survey speed. Operating in the 700–1800 MHz range, ASKAP is optimized for wide-field continuum and spectral line observations, particularly neutral hydrogen at cosmological redshifts.

The Rapid ASKAP Continuum Survey (RACS) is a large-scale radio survey that covers almost the entire southern sky ($\sim$ 36,000 deg^2) at frequencies of 887 MHz, 1.3 GHz, and 2.7 GHz, and represents the first major continuum survey carried out with ASKAP. It boasts high sensitivity (RMS noise ~ 0.2–$0.3\,\mathrm{mJy\,beam}^{-1}$) and a resolution of $\sim$10–15 arcseconds (McConnell et al., 2020b), significantly improving upon previous southern hemisphere radio surveys. The rapid survey speed of ASKAP enables RACS to provide an excellent snapshot of the southern sky, making it a valuable resource for studying AGN, star-forming galaxies, and large-scale radio structures, as well as for cross-matching with optical and infrared data. Finally, RACS will also serve as a pilot for deeper, more sensitive projects such as the Evolutionary Map of the Universe (EMU, Norris et al. 2011).

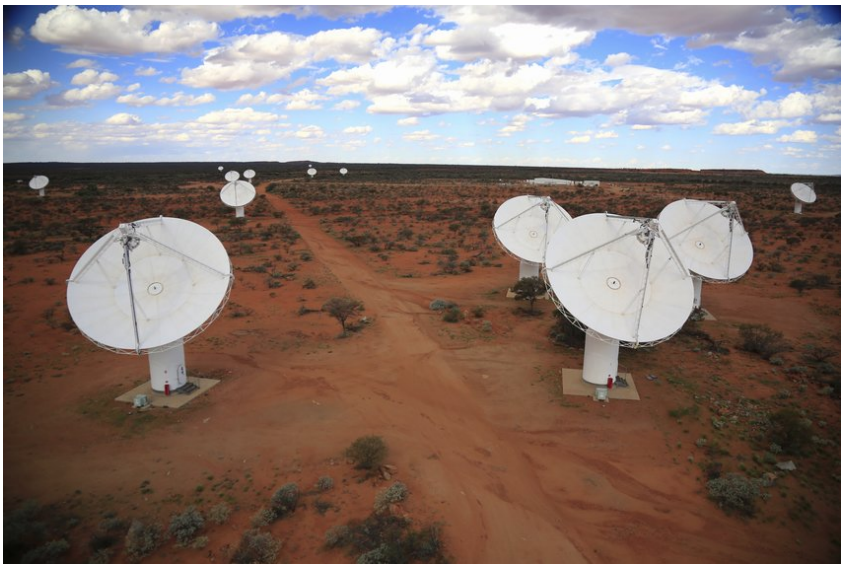

Figure 3.8: CSIRO's Australian Square Kilometre Array Pathfinder (ASKAP) telescope. Credit: Hotan et al. (2021).

4

Data reduction

In general, the calibration of the datasets was performed using standard pipeline procedures[1], with additional manual flagging applied to remove residual RFI and noisy scans. However, as a preparatory exercise, source `J1044+43`, part of Project 1, was calibrated directly from the raw dataset using the *Common Astronomy Software Applications* software (CASA Team et al., 2022) `CASA-6.6.3.22`, equipped with `IPython 7.34.0`.

In this section we present the main steps of the manual *calibration a priori* procedure applied to `J1044+43`, which serves as a preparatory stage for the subsequent self-calibration and imaging, both of which were performed manually for each source in the sample.

An initial assessment of the raw dataset can be performed with the `listobs` task, which provides a comprehensive summary of the observational setup and scan information. This particular sample was observed with the S-band of the VLA C-array, and covers a total integration time of 1790s (Figure 4.1), used to observe three fields across six scans and sixteen spectral windows (SpWs), starting at frequency 1988 Mhz and ending at 3884 Mhz. The three observed objects are:

- Phase calibrator: Field 0 (`J1130+3815`), scan 1,2 and 5.
- Target: Field 1 (`J1044+43`), scan 1 and 4.
- Flux calibrator: Field 2 (3C286), scan 6.

Upon examining the observer log, available in the `NRAO` archive, we noticed that four antennas were malfunctioning during data acquisition, in particular antenna 19, which was immediately partially removed.
We then visualised the physical layout of the antennas and their uv-coverage (Figure 4.2) through the graphical user interface `GUI`. During this step we also selected a reference antenna, whose phase (for both polarizations) will be arbitrarily set to zero during calibration. Antenna `ea12` was chosen as the reference due to its nominal performance and, more importantly, its central location within the array. The central position minimises atmospheric phase errors and provides a more symmetric calibration baseline, ensuring better stability and reliability during phase referencing.

[1] We used pipeline 2024.1.0.8 on `CASA 6.6.1-17`.

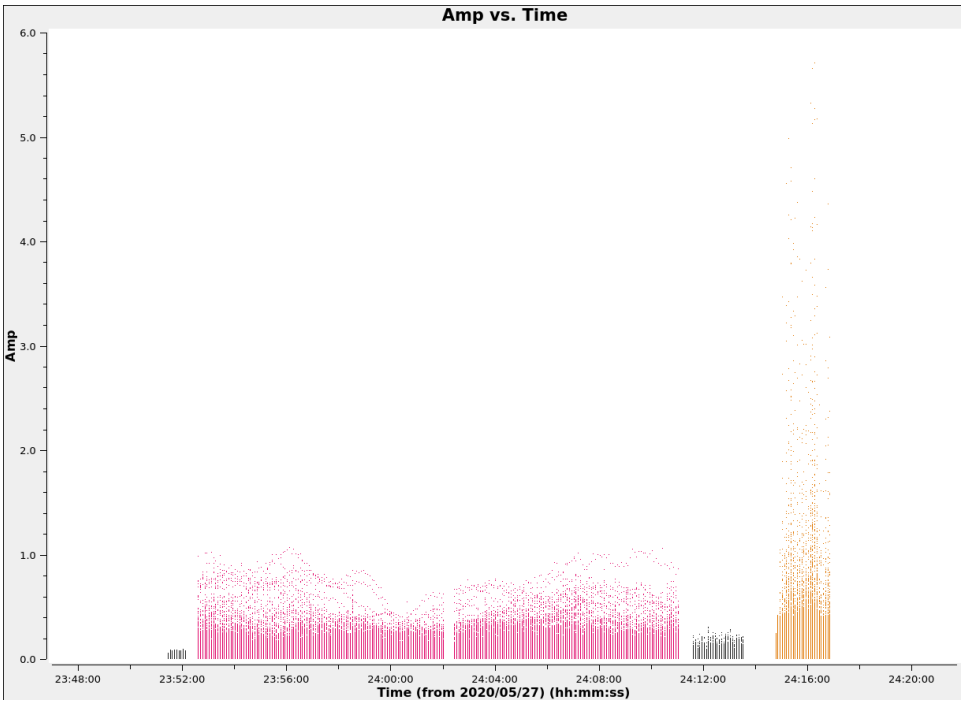

Figure 4.1: Amplitude vs time for the three fields of interest: target in red, primary (flux) calibrator in orange and secondary (phase) calibrator in black.

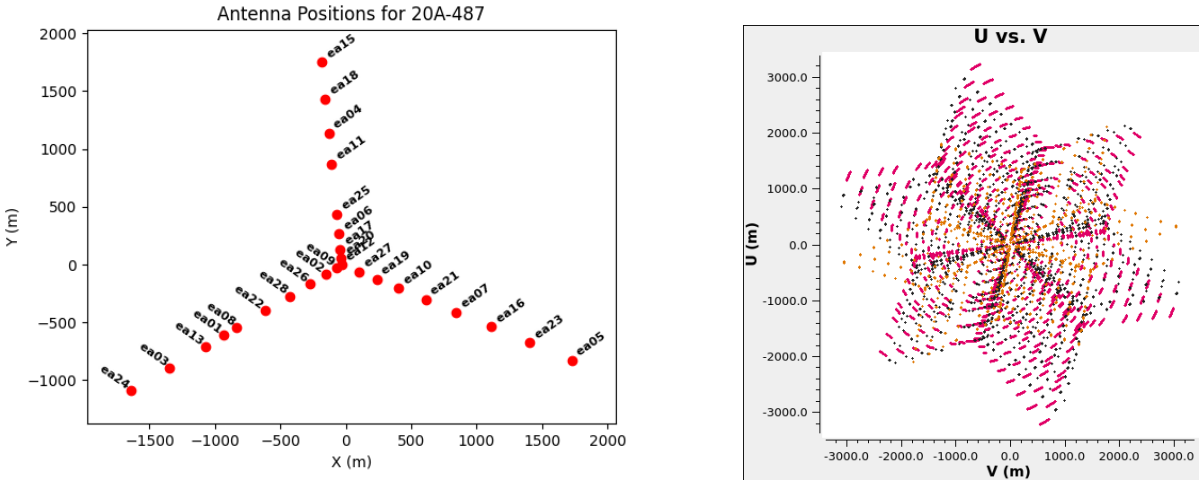

Figure 4.2: (Left) VLA antenna positions during J1044+43 observation: Antenna `ea12` was selected as the phase reference antenna for calibration. (Right) uv-coverage of the array.

4.1 Flagging

Before initiating the calibration process, it is necessary to identify and remove any corrupted or unreliable data from the dataset. Some data subsets are inevitably affected by instrumental issues, such as malfunctioning antennas or the reduced sensitivity of the outer channels of a spectral window, which stems from the shape of the bandpass filter.

The main cause of 'bad data' is associated with radio frequency interference (RFI), which refers to unwanted radio signals that contaminate astronomical observations, often originating from satellites. RFI can be continuous or intermittent, and it is more problematic within the low frequency range, such as the L-band we are using. SpWs 1 and 2 were removed (already visible in Figure 4.3) because they were affected by strong RFI.

We removed the *setup scan*, recognisable by its shorter integration time and its position at the beginning of the observation, as it serves only to stabilize the system and is not intended for scientific analysis. We then applied a *quack* flagging, discarding the first 10 seconds of each scan to account for potential initial instabilities.

After completing the standard initial flagging steps, attention was turned to the removal of RFI, which fortunately occurs at known, fixed frequencies, making it relatively easy to identify. Most of the flagging was done thanks to the automatic tools provided by `CASA`, such as `TFCrop` and `R-flag`, which will be introduced in the following. A preliminary benefit consists of running the *Hanningsmooth* algorithm through the homonymous task in `CASA`, which applies a triangle kernel that reduces and flags the number of channels that may look bad. This will decrease the spectral resolution by a factor of two, but deals with the strong RFI (Figure 4.4), which could otherwise cause a zig-zag pattern across the channels, otherwise known as Gibbs phenomenon.

The first autoflagging tool applied was `TFCrop`, an algorithm that identifies outliers in the two-dimensional time–frequency plane and can operate on uncalibrated (Non-bandpass-corrected) data. In many cases, however, `TFCrop` alone is insufficient to remove all RFI contamination. For this reason, we also employed `RFlag`, another RFI-detection algorithm that uses a sliding-window statistical filter to flag outliers. This tool is particularly effective for low-level, noisy RFI, but it requires calibrated data; therefore, a preliminary bandpass calibration was performed beforehand.

To further improve the flagging efficiency, the `extend` parameter was used to grow flags around existing flagged regions. However, a single application of these two autoflagging tools was not sufficient in most cases, and therefore an iterative process alternating `TFCrop` and `RFlag` was adopted. Finally, any residual bad data that persisted after the automated procedures were manually identified and flagged.

The post-flagging result is shown in Figure 4.5. The final percentage of flagged data amounts to approximately $\sim 50\%$, which was expected, as also the *VLA exposure time calculator*[2] predicted at least 25% RFI contamination in the S-band and an expected thermal noise of $\langle \sigma_{\mathrm{rms}} \rangle = 100\ \mu$Jy/beam.

[2] https://obs.vla.nrao.edu/ect/

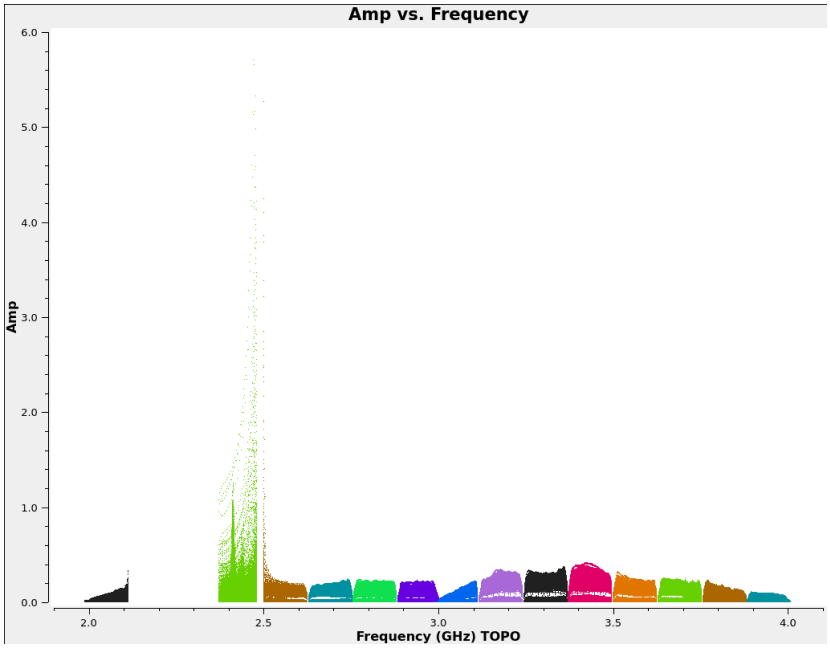

Figure 4.3: Amplitude vs Frequency of the target J1044+43 before Hanning smooth. SpW 1 and 2 have been already removed due to strong RFI.

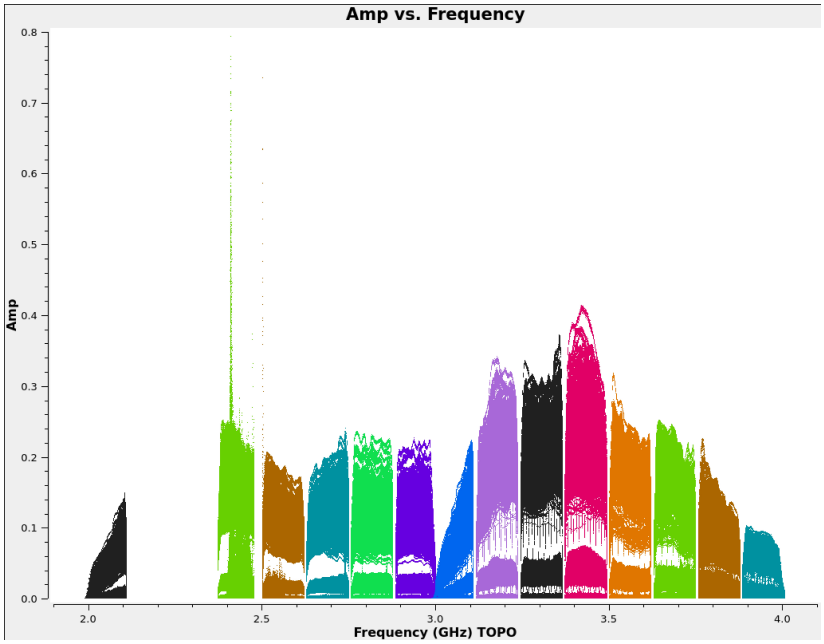

Figure 4.4: Plot of Amplitude vs Frequency of the target J1044+43 after Hanning smooth. Aside from that RFI spike in the SpW 3, the dataset has significantly improved.

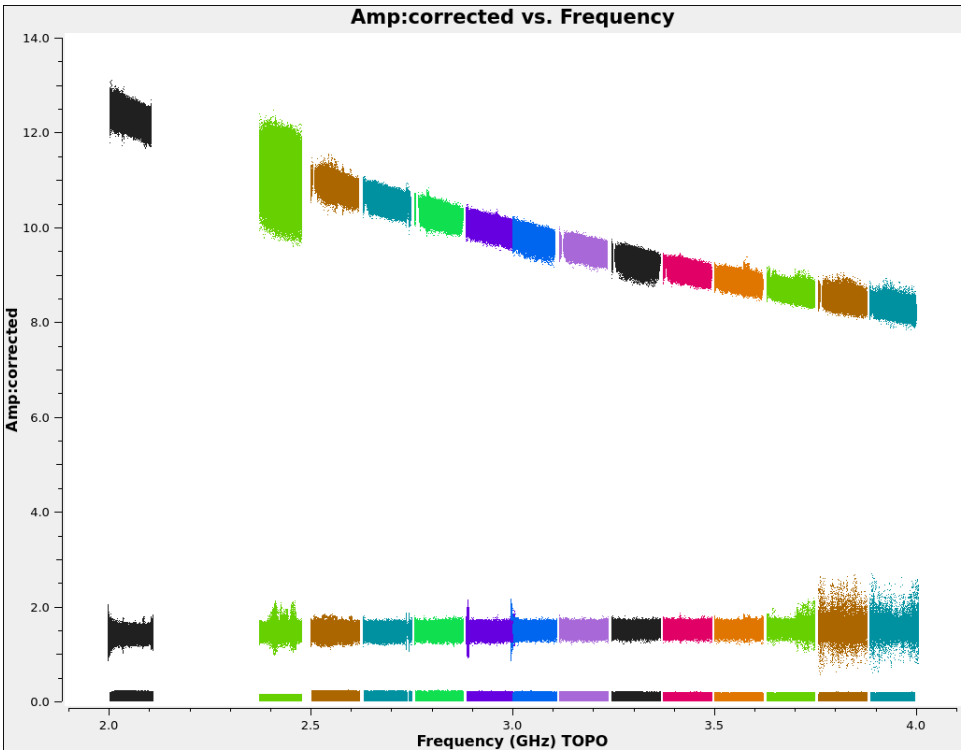

Figure 4.5: Plot of Amplitude vs Frequency of the three fields after the auto-flag procedure. From bottom to top are shown the target, secondry (phase) calibrator and primary (flux) calibrator.As `RFlag` operates on calibrated data, a preliminary bandpass calibration was first applied; thus, the dataset used in this step had already undergone a partial correction.

4.2 Calibration

Calibration is the process of determining the net complex correction factors that must be applied to the visibilities in order to make them as close as possible to what an idealised interferometer would measure. The corrections are derived by making use of two calibrators, and then applied to the target, with the assumption that the effects that distort the signal for all sources are similar, provided they are spatially close to each other.

The source visibilities collected by the antennas are corrupted by many different factors, such as the atmospheric and human interference, but also electronic noise coming from the instrumentation. The true visibilities V^{true} can be written as:

$$V_{ij}^{\text{true}}(u,v,\nu) = b_{ij}(t)B_i(\nu,t)B_j^*(\nu,t)g_i(t)g_j(t)V_{ij}^{\text{obs}}(u,v,\nu)e^{i[\theta_i(t)-\theta_j(t)]} \tag{4.1}$$

where the index (i,j) refers to two specific antennas, while:

- b_{ij} is the baseline term;
- B_i is the instrumental response as a function of frequency and time, namely the complex bandpass;

- $G_i = g_i e^{i\theta_i}$ is the complex gain, described by its amplitude g_i and phase θ_i, which calibrate the flux and phase of the target.

The calibration process has the goal of determining the values of these gains (which are just like the visibilities, complex numbers); which we can better visualize by rewriting equation 4.1 from the perspective of the observed visibilities V^{obs} in this very basic and simple way:

$$V_{ij}^{\text{obs}}(\nu, t) = G_{ij}(\nu, t) V_{ij}^{\text{true}}(\nu, t)\,, \tag{4.2}$$

where the dependence on time has been expressed because the quantities can change with temperature, atmospheric conditions, as well as various additional elements. The factor G_{ij} encompasses all the corruptions that affect the true visibilities; in this case only the Bandpass response B_{ij} and electronic gains J_{ij} have been considered, which are determined through calibrator sources during the observing period; while the impact of the troposphere is mitigated at later times by the self-calibration process.

Equation 4.2 describes a system of $N(N-1)/2$ baselines for an interferometer with N unknowns (antennae). This is an overdetermined problem that we can solve by using the principle of closure for amplitude and phase. To do this, we observe sources for which the true visibilities are known. These objects, called *calibrators*, are required to be bright sources to ensure high signal-to-noise ratios and consequently reliable solutions, and also point-like sources, whose Fourier transforms exhibit constant amplitude and zero phase, making them optimal references for gain calibration.

The primary calibrator serves as a flux calibrator and must not vary on short time scales; it is observed at least once, usually at the beginning or end of the observation. The secondary calibrator, or phase calibrator, must be angularly close to the target so that it can be observed several times alternately with the target, ensuring good phase sampling.

We now describe the steps to perform in the *calibration a priori*, displayed in the flow chart in Figure 4.6. The various steps of the calibration process, after the initial flagging, can be schematised in the following order:

1. **Antenna Position Correction**

   When antennas are moved, residual errors in the geographical coordinates of the antenna will cause time-dependent delay errors in the correlated data. Normally, the observatory will solve for these offsets soon after the move and correct the correlator model, but sometimes science data is taken before the offsets are available, and thus the correction must be handled in post-processing.

   Since the visibility function depends on u and v, when the baseline positions are incorrect, then u and v will be incorrectly calculated and there will be errors in the image. This task is used to correct for the exact distance that separates two antennas and to accurately calculate the geometric delay between them. The corrective term b_{ij} can be obtained directly from NRAO.

2. **Choosing the Model for the Primary Calibrator**

   `CASA` includes a database containing amplitude models for various flux calibrators: for this dataset, the model of the calibrator 3C286 was chosen and loaded into the `MODEL DATA` column of the measurement set. The flux density scale adopted for the VLA between 1 and 50 GHz is based on the standard model from Perley and Butler (2017). This allows us to compare the model with the observed values and calculate the conversion factor into physical units.

3. **Initial Phase Calibration**

   This step accounts for the small variations in phase with time in the bandpass, before solving for the bandpass solution itself. A selection of channels unaffected by RFI is made, and a time average of the phases of the associated visibilities is performed to reduce the scatter. In this step, a reference antenna must also be chosen, whose properties have been explained earlier.

4. **Geometric Delay Correction**

   The correlator must account for the geometric delay originating from the physical fact that the incoming signal does not reach all antennas simultaneously. The residual delay within a given spectral window, which is a function of frequency, is corrected by normalising it to the same reference antenna.

5. **Bandpass Calibration**

   The instrument does not respond uniformly across all frequencies; in fact, the frequency variations of the visibility data are a reflection of the different antenna bandpasses. Therefore, the bandpass calibrator, which in our case coincides with the flux calibrator, is used to compute the corrective terms B_i.

6. **Gain Calibration**

   The next step is to derive corrections for the complex antenna gains, g_i and θ_i. The signal received by the baselines must first travel through the Earth atmosphere, which is extremely variable in time. In order to have a fair representation of the atmospheric fluctuation of the target signal, it is necessary to look at a bright point-like source spatially close to our target, the secondary (phase) calibrator.

   Being the atmosphere variable in time, we have to make multiple scans on the phase calibrator during the observation to track these variations, which we assumed to be linear. While for the primary calibrator a known flux density value has been previously set, for the secondary calibrator the flux density is not known and thus it is set to an arbitrary value of 1 Jy and must be properly scaled. On the other hand, we do not have this discrepancy for the phases, being both calibrators point-like objects whose Fourier transform produces constant trends; apart from small fluctuation that can be ascribed to the atmosphere.

7. **Scaling the Amplitude Gains**

   Having determined the relative gain amplitudes and phases across the array using the secondary calibrator, we can compare these gain amplitudes with those previously obtained from the primary calibrator. The primary calibrator, being a source of known flux density, allows for an unambiguous determination of the intrinsic flux density of the secondary calibrator. We re-scale the amplitude gains in this way:

$$V^{i,j}_{\text{obs,sec}} = G^{i,j}_{\text{sec}} V^{i,j}_{\text{model,sec}} \quad \Rightarrow \quad V^{i,j}_{\text{obs,sec}} = G^{i,j}_{\text{sec}} \cdot 1\,\text{Jy} \tag{4.3}$$

   As mentioned above, since $V^{i,j}_{\text{model,sec}}$ is unknown, `CASA` sets a fictitious arbitrary value of 1 Jy as the first estimation to solve for $G^{i,j}_{\text{sec}}$. We can now find the correct value using the aforementioned antenna correction $G^{i,j}_{\text{prim}}$:

$$V^{i,j}_{\text{obs,sec}} = G^{i,j}_{\text{prim}} V^{i,j}_{\text{model,sec}} \quad \Rightarrow \quad V^{i,j}_{\text{model,sec}} = \frac{V^{i,j}_{\text{obs,sec}}}{G^{i,j}_{\text{prim}}} = \frac{G^{i,j}_{\text{sec}} \cdot 1\,\text{Jy}}{G^{i,j}_{\text{prim}}} \tag{4.4}$$

   The flux rescaling is performed through the task *fluxscale*, which returned a flux density value of 1.522 ± 0.002 Jy for the secondary (phase) calibrator J1130+3815. This task also returns the flux density for all spectral windows (SpWs) (Table 4.1).

Window	**Flux Density (Jy)**
SpW 0	1.413 ± 0.002
SpW 1	*Insufficient Data*
SpW 2	*Insufficient Data*
SpW 3	1.484 ± 0.007
SpW 4	1.475 ± 0.006
SpW 5	1.461 ± 0.005
SpW 6	1.458 ± 0.005
SpW 7	1.465 ± 0.005
SpW 8	1.481 ± 0.005
SpW 9	1.494 ± 0.005
SpW 10	1.501 ± 0.005
SpW 11	1.506 ± 0.005
SpW 12	1.560 ± 0.005
SpW 13	1.572 ± 0.005
SpW 14	1.573 ± 0.005
SpW 15	1.502 ± 0.001
J1131+3815	**1.522 ± 0.002**

Table 4.1: Flux density derived for the secondary (phase) calibrator `J1130+3815`. The flux density of SpW 1 and 2 are missing because they were removed. In the last row is presented the first order fit for the flux density estimation of `J1130+3815`.

8. **Applying the Calibration.**

   After computing all the gains, the corrections can be applied to the two calibrators, and the visibilities are inspected to ensure the quality of the calibration. The calibration is not an immediate process, but requires several iterations until the desired level of accuracy is achieved (low scatter of phase and amplitude gains).

   Only at that point the gains can be applied to the target. In this specific case, the calibration was performed three times, and then the corrections were finally applied also to the target, whose final calibrated visibilities are shown in Figure 4.7.

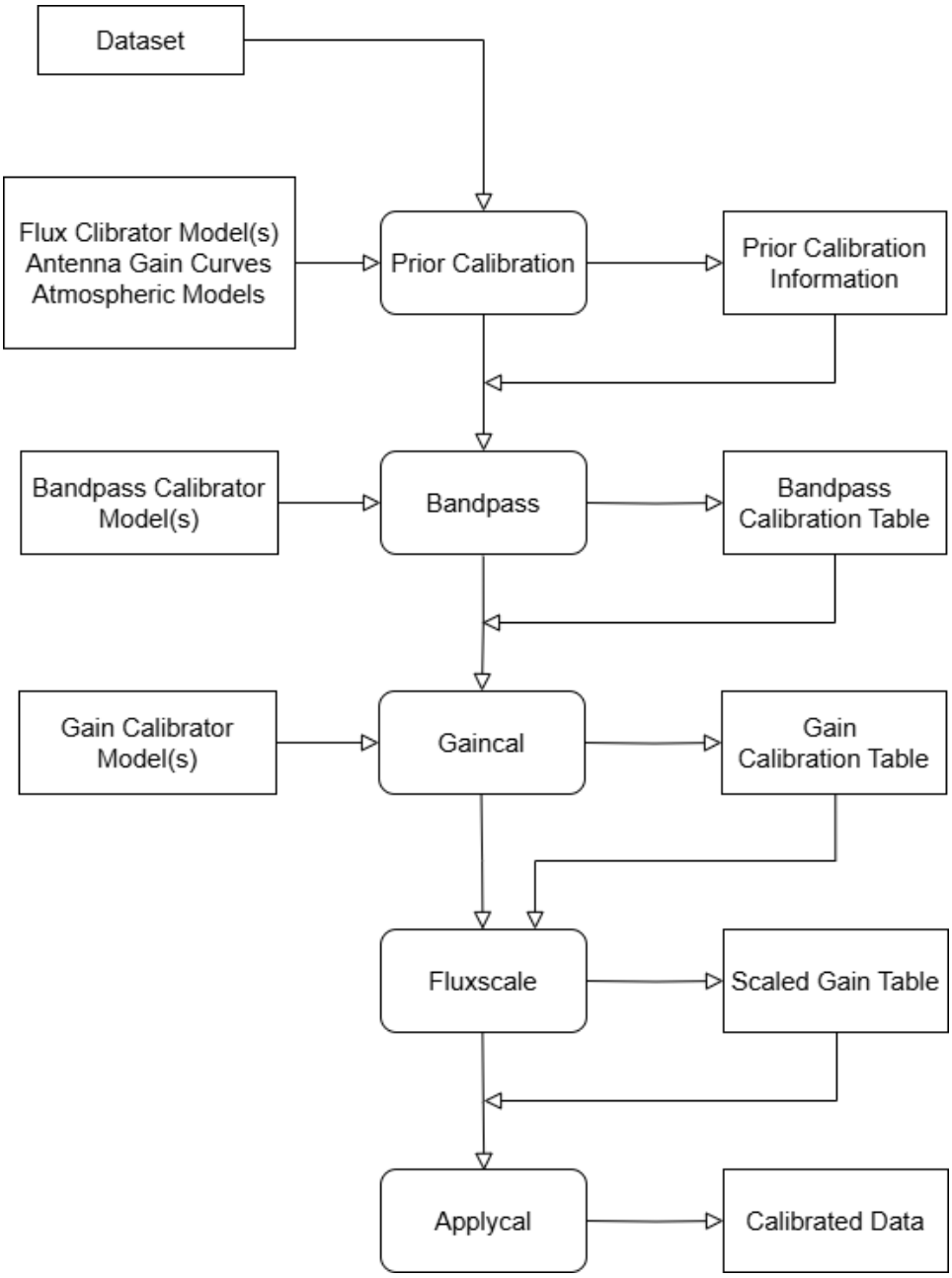

Figure 4.6: Flowchart of the key steps in *a priori calibration*: first column represent the input data, the second column the process (embodied by a task) and the third column the output data.

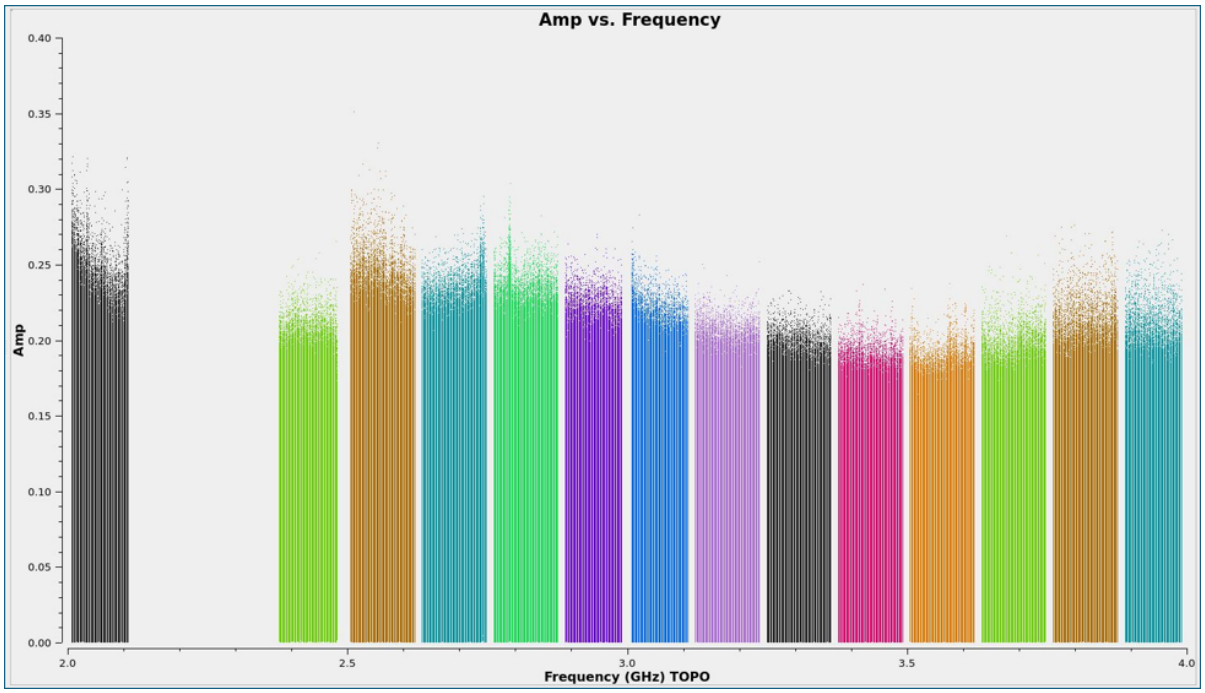

Figure 4.7: Calibrated visibilities of the target.

4.3 Imaging

Once the data are prepared and the calibration is deemed satisfactory, the calibrators are no longer needed. At this stage, the dataset can be split to produce a new measurement set containing only the calibrated data for each individual target, which are written in the `DATA COLUMN`.

From this point onward, we will consider both Projects 1 and 2, as imaging has now been performed on all 32 available sources. Before proceeding, however, a brief digression on the theoretical foundations of imaging is in order. It is useful to recall the relation between the visibility data $V(u, v)$ and the brightness distribution $I(l, m)$, which are Fourier transform pairs:

$$I(l, m) = \int V(u, v)\, e^{[2\pi i(ul+vm)]}\, du\, dv \tag{4.5}$$

where u, v are the baselines measured in units of the observing wavelength, while the l and m coordinates are the direction cosines on the sky, which can be simply correlated to the right ascension and declination respectively.

In the image plane, the sampled visibility translates into the sampled brightness (called the *Dirty Map* (DM), I^{DM}) given by the convolution between the true brightness distribution I^{True} and the *Dirty Beam* (DB):

$$I^{\mathrm{DM}} = I^{\mathrm{True}} * \mathrm{DB} \tag{4.6}$$

where the DB and the DM are obtained respectively as the Fourier transforms of the sampling function[3] Π and the sampled visibility. Therefore, to recover the true brightness distribution, that is, the *clean map*, it is necessary to deconvolve the dirty map with the dirty beam; or alternatively, we can directly calculate the inverse Fourier transform of the sampled visibility V_s and link it to the true map using the convolution theorem:

$$F^{-1}(V) = F^{-1}(V_s \cdot \Pi) = F^{-1}(V_s) * F^{-1}(\Pi) \tag{4.7}$$

The ensemble of these operations constitutes the cleaning process. We assume that the source is the sum of many point-like objects, whose brightness is described by a Dirac δ-function. From the Dirty Map, the intensity and position of the brightest *clean components* (CCs) are identified. These CCs are Fourier transformed and subtracted from the visibilities, leaving the residual visibilities V^{res}:

$$V^{\text{res}} = V^{\text{obs}} - \text{FT}\left(\sum \text{CC}\right) \tag{4.8}$$

This process is repeated until all peaks in the image have been identified and subtracted. At this point, the CCs are convolved with a '*clean beam*'—given by a Gaussian fit of the main lobe of the dirty beam—and the resulting map is added to the noise map, resulting in the clean map. Equation 4.8 can also be written in terms of brightness:

$$I^{\text{residual}}(x,y) = I^{\text{dirty}}(x,y) - \gamma B(x,y) * I^{\text{clean}}(x,y) \tag{4.9}$$

Here $\gamma = 0.1 - 0.3$ is the loop gain of the CLEAN algorithm, it controls how much of the peak intensity is removed during each iteration of CLEAN. $B(x,y)$ is the dirty beam, and $I^{\text{clean}}(x,y)$ is the pixel with the highest brightness. The cleaning process can be stopped when all residual peaks are comparable to the thermal noise level of the image, or when the total flux density has converged. The restoring process starts from the last produced residual image, adds the clean component convolved with the clean beam and adds it back to the residual image:

$$I^{\text{final}}(x,y) = I^{\text{clean}}(x,y) * B'(x,y) + I^{\text{residual}}(x,y) \tag{4.10}$$

The task used in `CASA` to produce images is called `tclean`, which both Fourier transforms the data and deconvolves the resulting image. A preliminary step, before running `tclean`, is the choice of the parameters for the task. First of all, properly selecting the sampling interval, i.e. the pixel size Δx, to avoid aliasing. To achieve this, it is sufficient to satisfy the sampling theorem, which provides a condition under which a discrete set of samples can fully capture the information from a continuous signal. In the context of interferometry, this means sampling up to a spatial frequency determined by the maximum baseline u_{max}. This condition is known as the Nyquist rate and can be expressed as follows:

[3]The Sampling Function Π, which is essentially the uv-plane, takes the value 1 at the points where the visibility has been measured and the value 0 everywhere else.

$$\Delta x \leq \frac{1}{2\,u_{\max}} \tag{4.11}$$

A safe choice, for a good sampling, is to sample the beam with 3 to 7 pixels, and never less than 2 (from Eq. 4.11). We opted for 5 pixel per beam. Therefore, we estimated the angular resolution as $\theta = (\lambda/u_{\max}) \cdot 206265$ [arcsec], where 206265 is the conversion factor from radians to arcseconds, and then the pixel size as $= \theta/5$ [arcsec]

4.4 Self Calibration

After calibrating a data set using the observed calibrator sources, there may be residual phase and/or amplitude errors in the calibrated data of the target source that still degrade the image quality. Self-calibration, or *selfcal*, is fundamentally similar to standard 'calibration a priori', with the subtle difference that this time is the target source itself the calibrator. This particular becomes increasingly important for bright and extended sources, where phase errors cannot always be fully corrected by relying solely on a secondary calibrator observed in different pointings. In fact, atmospheric conditions can vary on much shorter timescales than the interval between calibrator scans. For this reason, it is desirable to derive calibration solutions over shorter timescales.

The self-calibration process reduces the interpolation timescale, exploiting the highest signal-to-noise visibilities of the target itself to improve phase stability; producing this time a non-point-like source model for the atmospheric variations. Each "round" of self-calibration presented here will follow the same general procedure:

1. Create an initial model by conservatively cleaning the target field with a mask;
2. Obtain the calibration table with the solutions (*gaincal task*);
3. Inspect the calibration solutions using plotms and flag bad data;
4. Apply the calibration table with the solutions to the data (*applycal task*).

Repeat through points 1 to 4 for how many cycles are needed, as there is no universal rule as long as the rms is reduced in each iteration. The most important parameter is the *solint*, which sets the temporal interval to interpolate the calibration solutions more finely. When the thermal noise stops improving; or equivalently, the dynamic range—defined as the ratio between the peak flux and the rms—does not change anymore, it is a good sign to stop the selfcal. It is common practice to first run the self-calibration for the phases only, since phase errors (due to atmospheric fluctuations, antenna position errors, clock errors, etc.) are generally more significant and can severely distort the image, causing loss of coherence and resolution. Then, when the phase-selfcal no longer provides improvements, a subsequent attempt that involves also the amplitude— the *amplitude-selfcal*—could be useful to further reduce residual artefacts and improve the rms. The whole process can require anywhere from a single cycle to multiple iterations of both types of selfcal.

5. As a last step, a final tclean is launched to produce a final image.

The cleaning was performed using a *Hogbom deconvolver* in a *standard grid*, *mfs-specmode*, *interactive mode*, without a *threshold* and adopting a *Briggs weight* with *robust parameter* r= 0.5), and finally a variable *imsize*. We briefly explain the meaning behind this configuration:

- **Deconvolver**: is the algorithm used for the deconvolution process meant to reconstructs the sky image from the observed visibility data. Different algorithms are optimised for different types of data and imaging scenarios. The Hogbom deconvolver we used is an adapted version of the Hogbom Clean (Högbom, 1974) and is better suited for point-like (or compact) sources, ideal for FR 0s.

- **Grid**: is a regular pixel grid defined by the image cell size and image dimensions. the standard grid is simply a Cartesian grid in right ascension (RA) and declination (Dec), with pixel sizes set at 1/5 of the beam in this case.

- **Ppecmode**: stands for 'spectral mode', in case of the multi-frequency synthesis (mfs) mode, it allows for multi-frequency analysis instead of a monochromatic view. This enables the production of a map with the average frequency across the bandwidth, as well as a map at the frequency of each channel (the 'cube' map, typically used for line emission analysis).

- **Niter, threshold**: The `clean` task can operate automatically or interactively, but in both cases the process stops when one of these two parameters is reached. We did not use a threshold and a niter= 5000 was sufficient for the whole cleaning process.

- **Weight**: gives more or less weight to certain visibilities (i.e. baselines) in the data set. In this study, three weighting schemes were used: (i) `Natural`: Data visibility weights are gridded onto a uv-cell and summed. More visibilities in a cell will increase the cell's weight, and since uv cells are weighted based on their rms, this will usually emphasise shorter baselines. Natural weighting, therefore, results in a better surface brightness sensitivity but also in a larger PSF and therefore in a degraded resolution. (ii) `Uniform`: weights are first gridded as in natural weighting, but then each cell is corrected so that the weights are independent of the number of visibilities inside. This gives a fairer representation of the uv-coverage and sidelobes are more suppressed, resulting in a smaller PSF and better spatial resolution; favouring extended sources with respect to natural weighting, but with worse sensitivity (higher rms). `Briggs`: the robust parameter R (with $-2 \leq R \leq 2$) balances between natural ($R = 2$) and uniform ($R = -2$) weighting. This option offers a compromise between spatial resolution and surface brightness sensitivity, and usually robust values near zero are used.

- **Imsize**: defines the dimensions of the map in pixels. It is typically chosen as a grid size proportional to the field of view.

We used the Briggs weight (robust parameter r=0.5) during the whole self calibration to highlight the compact nature of FR 0s, and additional tests with different weight (natural or uniform) were also carried out in an attempt to uncover additional diffuse emission in the resolved sources. However, due to the compactness of the sources, not many differences were discovered in these attempts.

Project 1

These 5 FR 0s used the C-configuration of the VLA, observed at a central frequency of 3 GHz (S-band). The final images were produced on a [2048x2048] grid with a pixel size of 1.0 arcsec and confidence contours of [-3, 3, 5, 10, 20, 50, 100]σ_{rms}.
The self-calibration procedure improved the RMS and the peak flux, with respect to the pre-selfcal image, around 50% and 3.5%, respectively. The total percentage of flag is averaged at $\sim$ 40%. Table 4.2 reports the final results:

Name	**RMS** [mJy·beam^{-1}]	**Peak** [mJy/beam]	**Beam** [arcsec]
J0807+14	$2.10 \cdot 10^{-2}$	27.11	8.50 x 6.98
J0910+18	$3.28 \cdot 10^{-2}$	28.87	8.28 x 6.02
J0916+17	$1.88 \cdot 10^{-2}$	9.76	10.49 x 7.31
J1044+43	$2.67 \cdot 10^{-2}$	33.12	7.22 x 6.64
J1722+30	$1.35 \cdot 10^{-2}$	3.70	7.46 x 7.10

Table 4.2: Map parameters for the 5 FR 0s sources after self calibration. Columns: (1) source name; (2) RMS noise in the map with Briggs weight (r=0.5); (3) peak flux density, associated uncertainty of $\sim$ 5%; (4) synthesized beam size.

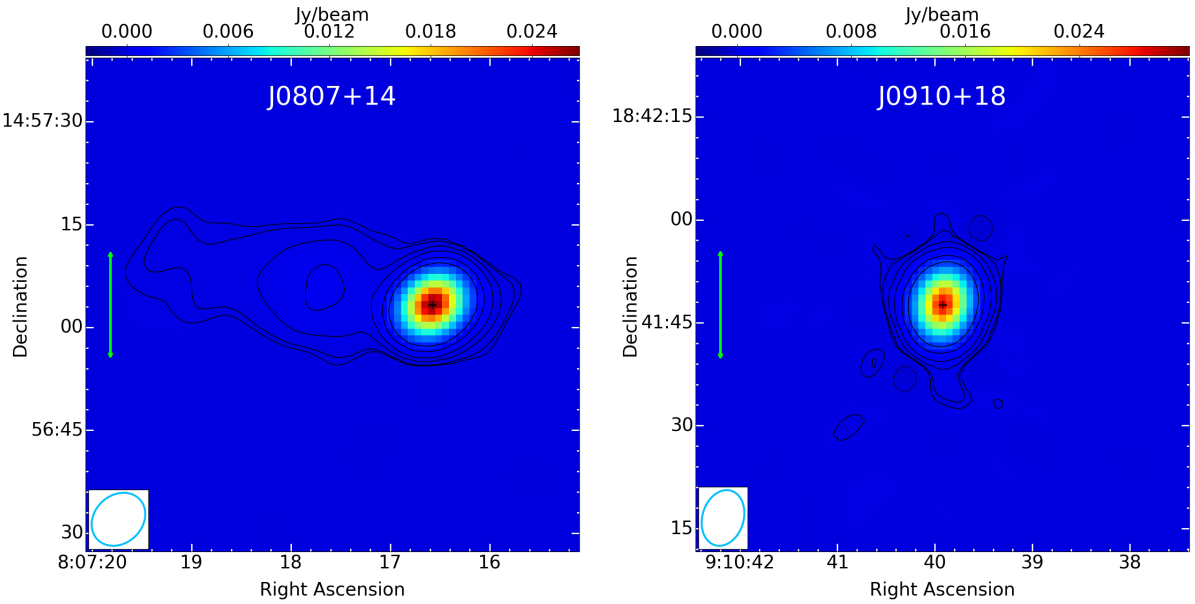

Figure 4.8: VLA radio maps of Project 1 after self-calibration with Briggs (r=0.5) weight. The contour levels follow the sequence [-3, 3, 5, 10, 20, 50, 100] σ_{rms}, where σ_{rms} is the local rms of the final maps reported in Table 4.2. The green arrow indicates a symbolic scale of 20 kpc, while the beam is shown in the bottom-left corner. Continued on next page

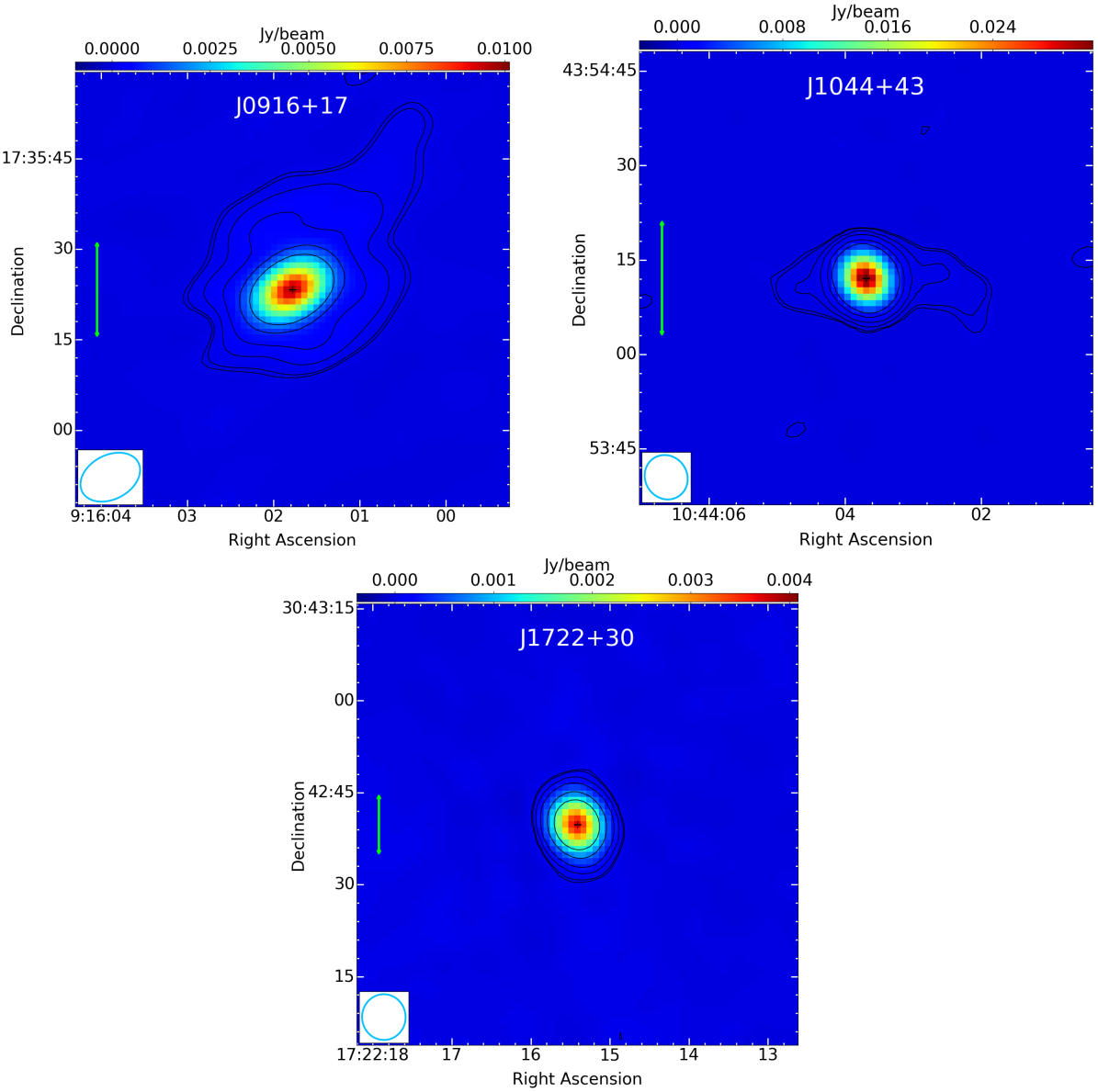

Project 2

This project contains 27 FR 0s, observed at 1.5, 4.5 and 7.5 GHz (L,C bands) in the A-configuration of the JVLA. The final images were produced on a variable square grid (max: 20'000 arcsec, min: 6144 arcsec) with a pixel size, at the three frequency, of [0.20, 0.07, 0.05] arcsec. In the tables below, all VLA maps use Briggs weighting with a robust parameter of 0.5 (Briggs0.5).

In most cases, self-calibration was performed individually for each band (L,C1,C2), with the exception of a few objects where the C band was self-calibrated as a whole (C_{TOT} =C1+C2) and then the individual bands C1 and C2 were split from C_{TOT} at the end. In addition to saving time, this method facilitated the self-calibration procedure by having a higher signal-to-noise ratio (SNR) in faint objects. The validity of this method was (empirically) confirmed for sources lacking extended emission, while it caused some problems otherwise. This method was successfully applied to 12 compact objects without issues, most of which were reassessed by self calibrating the individual C1- and C2-band, revealing discrepancies of less than 5%.

The self-calibration procedure improved the RMS and peak flux relative to the pre-selfcal image by approximately 25% and 3% in the L-band, with a total percentage of flag averaged at $\sim 40-45\%$ due to the strong RFI at these frequencies. The C-band was significantly less affected by RFIs, and the selfcal improved the RMS and peak flux of around 50% and 5%, with an average flag percentage of $\sim 30-35\%$. We report the final results of the self-calibration in Table 4.3:

Table 4.3: Selfcal parameters for the 27 FR 0 sources in Briggs weight (robust=0.5) at the three frequencies 1.5, 4.5 and 7.5 GHz; each source has three rows, one for each frequency: from the top 1.5, 4.5, 7.5 GHz. Columns: (1) source name; (2) RMS noise in the map; (3) peak flux of the source at the end of the self-calibration, uncertainty of $\sim 5\%$; (4) confidence contour used in the final maps.

Name	**RMS** [mJy/beam]	**Peak** [mJy/beam]	**Beam** [arcsec]	**Contours** [σ]
J0108−00	$2.44 \cdot 10^{-1}$	11.18	1.61 x 1.26	-3,3,5,10,20,50,100
	$4.35 \cdot 10^{-2}$	10.49	0.39 x 0.36	-3,3,5,10,20,50,100
	$1.29 \cdot 10^{-2}$	13.36	0.28 x 0.25	-3,3,5,10,20,50,100
J0112−00	$4.61 \cdot 10^{-2}$	16.79	1.37 x 1.16	-3,3,5,10,20,50,100
	$1.71 \cdot 10^{-2}$	13.67	0.46 x 0.39	-3,3,5,10,20,50,100
	$1.65 \cdot 10^{-2}$	11.12	0.46 x 0.26	-3,3,5,10,20,50,100
J0115+00	$3.57 \cdot 10^{-2}$	45.63	1.29 x 1.11	-3,3,5,10,20,50,100
	$1.87 \cdot 10^{-2}$	42.05	0.46 x 0.44	-3,3,5,10,20,50,100
	$1.64 \cdot 10^{-2}$	37.00	0.41 x 0.27	-3,3,5,10,20,50,100
J0753+13	$2.72 \cdot 10^{-2}$	3.11	1.23 x 1.20	-3,3,5,10,20,50,100
	$1.36 \cdot 10^{-2}$	3.37	0.51 x 0.44	-3,3,5,10,20,50,100
	$1.18 \cdot 10^{-2}$	2.62	0.31 x 0.26	-3,3,5,10,20,50,100
J0807+14	$3.02 \cdot 10^{-2}$	20.42	1.24 x 1.18	-3,3,5,10,20,50,100
	$1.53 \cdot 10^{-2}$	22.01	0.41 x 0.37	-3.5,3.5,5,10,20,50,100
	$1.54 \cdot 10^{-2}$	24.97	0.28 x 0.25	-3,3,5,10,20,50,100
J0847+10	$3.47 \cdot 10^{-2}$	19.93	1.22 x 1.16	-3,3,5,10,20,50,100
	$1.65 \cdot 10^{-2}$	12.59	0.43 x 0.40	-3,3,5,10,20,50,100
	$1.45 \cdot 10^{-2}$	10.10	0.26 x 0.23	-3,3,5,10,20,50,100
J1018+00	$2.73 \cdot 10^{-2}$	5.72	1.63 x 1.30	-3,3,5,10,20,50,100
	$1.46 \cdot 10^{-2}$	2.37	0.48 x 0.44	-3,3,5,10,20,50,100
	$1.27 \cdot 10^{-2}$	1.52	0.30 x 0.29	-3,3,5,10,20,50,100
J1024+42	$2.98 \cdot 10^{-2}$	5.30	1.47 x 1.25	-3,3,5,10,20,50,100
	$2.43 \cdot 10^{-2}$	2.68	0.80 x 0.40	-3,3,5,10,20,50,100
	$2.68 \cdot 10^{-2}$	1.39	0.43 x 0.24	-3,3,5,10,20,50,100
J1048+04	$6.90 \cdot 10^{-2}$	46.97	1.65 x 1.26	-5,5,10,20,50,100

Continued on next page

	$1.97 \cdot 10^{-2}$	26.42	0.49 x 0.44	-5,5,10,20,50,100
	$1.68 \cdot 10^{-2}$	18.80	0.30 x 0.27	-5,5,10,20,50,100
J1048+48	$3.46 \cdot 10^{-2}$	14.68	1.41 x 1.12	-5,5,10,20,50,100
	$2.63 \cdot 10^{-2}$	3.83	0.55 x 0.47	-3,3,5,10,20,50,100
	$2.07 \cdot 10^{-2}$	2.09	0.31 x 0.29	-3,3,5,10,20,50,100
J1057+40	$4.07 \cdot 10^{-2}$	33.40	1.53 x 1.29	-5,5,10,20,50,100
	$3.23 \cdot 10^{-2}$	19.72	10.52 x 0.43	-5,5,10,20,50,100
	$2.72 \cdot 10^{-2}$	14.49	0.35 x 0.23	-5,5,10,20,50,100
J1120+04	$2.88 \cdot 10^{-2}$	7.43	1.81 x 1.26	-3,3,5,10,20,50,100
	$1.63 \cdot 10^{-2}$	4.75	0.56 x 0.45	-3,3,5,10,20,50,100
	$1.38 \cdot 10^{-2}$	3.96	0.35 x 0.29	-3.5,3.5,5,10,20,50,100
J1308+43	$3.98 \cdot 10^{-2}$	48.29	1.54 x 1.29	-5,5,10,20,50,100
	$2.03 \cdot 10^{-2}$	36.06	0.68 x 0.41	-5,5,10,20,50,100
	$2.36 \cdot 10^{-2}$	36.56	0.45 x 0.25	-5,5,10,20,50,100
J1330+32	$2.77 \cdot 10^{-2}$	16.08	1.83 x 1.12	-3.5,3.5,5,10,20,50,100
	$1.66 \cdot 10^{-2}$	11.20	0.93 x 0.39	-3.5,3.5,5,10,20,50,100
	$1.57 \cdot 10^{-2}$	9.34	0.57 x 0.24	-3.5,3.5,5,10,20,50,100
J1341+29	$2.68 \cdot 10^{-2}$	7.61	1.94 x 1.15	-3,3,10,20,50,100
	$1.62 \cdot 10^{-2}$	6.84	0.89 x 0.46	-3,3,5,10,20,50,100
	$1.86 \cdot 10^{-2}$	6.03	0.81 x 0.30	-3,3,5,10,20,50,100
J1350+33	$4.67 \cdot 10^{-2}$	103.62	1.87 x 1.14	-5,5,10,20,50,100
	$3.93 \cdot 10^{-2}$	85.17	1.00 x 0.66	-3.5,3.5,5,10,20,50,100
	$3.13 \cdot 10^{-2}$	92.38	0.42 x 0.24	-3,3,5,10,20,50,100
J1427+37	$2.68 \cdot 10^{-2}$	6.03	1.36 x 1.22	-3,3,5,10,20,50,100
	$1.55 \cdot 10^{-2}$	1.24	0.50 x 0.40	-3,3,5,10,20,50,100
	$1.77 \cdot 10^{-2}$	0.56	0.30 x 0.25	-3,3,5,10,20,50,100
J1433+52	$2.89 \cdot 10^{-2}$	13.41	1.43 x 1.11	-3,3,5,10,20,50,100
	$1.60 \cdot 10^{-2}$	8.69	0.53 x 0.37	-3,3,5,10,20,50,100
	$1.76 \cdot 10^{-2}$	6.60	0.36 x 0.22	-3,3,5,10,20,50,100
J1521+07	$3.54 \cdot 10^{-2}$	4.33	1.68 x 1.66	-3,3,5,10,20,50,100
	$1.74 \cdot 10^{-2}$	1.07	0.80 x 0.40	-3,3,5,10,20,50,100
	$1.55 \cdot 10^{-2}$	0.48	0.48 x 0.25	-3,3,5,10,20,50,100
J1541+45	$2.72 \cdot 10^{-2}$	5.35	1.47 x 1.07	-3,3,5,10,20,50,100
	$1.6 \cdot 10^{-2}$	3.21	0.67 x 0.38	-3,3,5,10,20,50,100
	$2.13 \cdot 10^{-2}$	2.38	0.44 x 0.22	-3,3,5,10,20,50,100
J1544+43	$2.77 \cdot 10^{-2}$	6.97	1.54 x 1.20	-3,3,5,10,20,50,100
	$1.65 \cdot 10^{-2}$	13.41	0.66 x 0.37	-3,3,5,10,20,50,100

Continued on next page

	$1.64 \cdot 10^{-2}$	13.68	0.41 x 0.21	-3.5,3.5,5,10,20,50,100
J1544+47	$2.58 \cdot 10^{-2}$	17.44	1.52 x 1.12	-3,3,5,10,20,50,100
	$1.66 \cdot 10^{-2}$	12.05	0.64 x 0.37	-3,3,5,10,20,50,100
	$1.79 \cdot 10^{-2}$	9.47	0.44 x 0.22	-3,3,5,10,20,50,100
J1559+44	$5.72 \cdot 10^{-2}$	43.62	1.51 x 1.16	-5,5,10,20,50,100
	$1.88 \cdot 10^{-2}$	11.00	0.59 x 0.36	-3.5,3.5,5,10,20,50,100
	$1.64 \cdot 10^{-2}$	4.80	0.39 x 0.21	-3.5,3.5,5,10,20,50,100
J1606+08	$3.44 \cdot 10^{-2}$	7.73	1.52 x 1.22	-3.5,3.5,5,10,20,50,100
	$1.83 \cdot 10^{-2}$	3.16	0.55 x 0.43	-3.5,3.5,5,10,20,50,100
	$1.98 \cdot 10^{-2}$	1.88	0.32 x 0.25	-3.5,3.5,5,10,20,50,100
J1612+09	$3.32 \cdot 10^{-2}$	18.40	1.54 x 1.22	-4.5,4.5,5,10,20,50,100
	$1.81 \cdot 10^{-2}$	6.66	0.50 x 0.45	-4.5,4.5,5,10,20,50,100
	$2.00 \cdot 10^{-2}$	3.87	0.34 x 0.32	-4,4,5,10,20,50,100
J1629+40	$2.88 \cdot 10^{-2}$	3.90	1.11 x 0.94	-3,3,5,10,20,50,100
	$1.69 \cdot 10^{-2}$	1.84	0.41 x 0.31	-3,3,5,10,20,50,100
	$1.68 \cdot 10^{-2}$	1.38	0.26 x 0.19	-3,3,5,10,20,50,100
J1649+36	$2.54 \cdot 10^{-2}$	3.27	1.22 x 1.14	-3,3,5,10,20,50,100
	$1.48 \cdot 10^{-2}$	0.92	0.47 x 0.41	-3,3,5,10,20,50,100
	$1.60 \cdot 10^{-2}$	0.71	0.26 x 0.25	-3,3,5,10,20,50,100

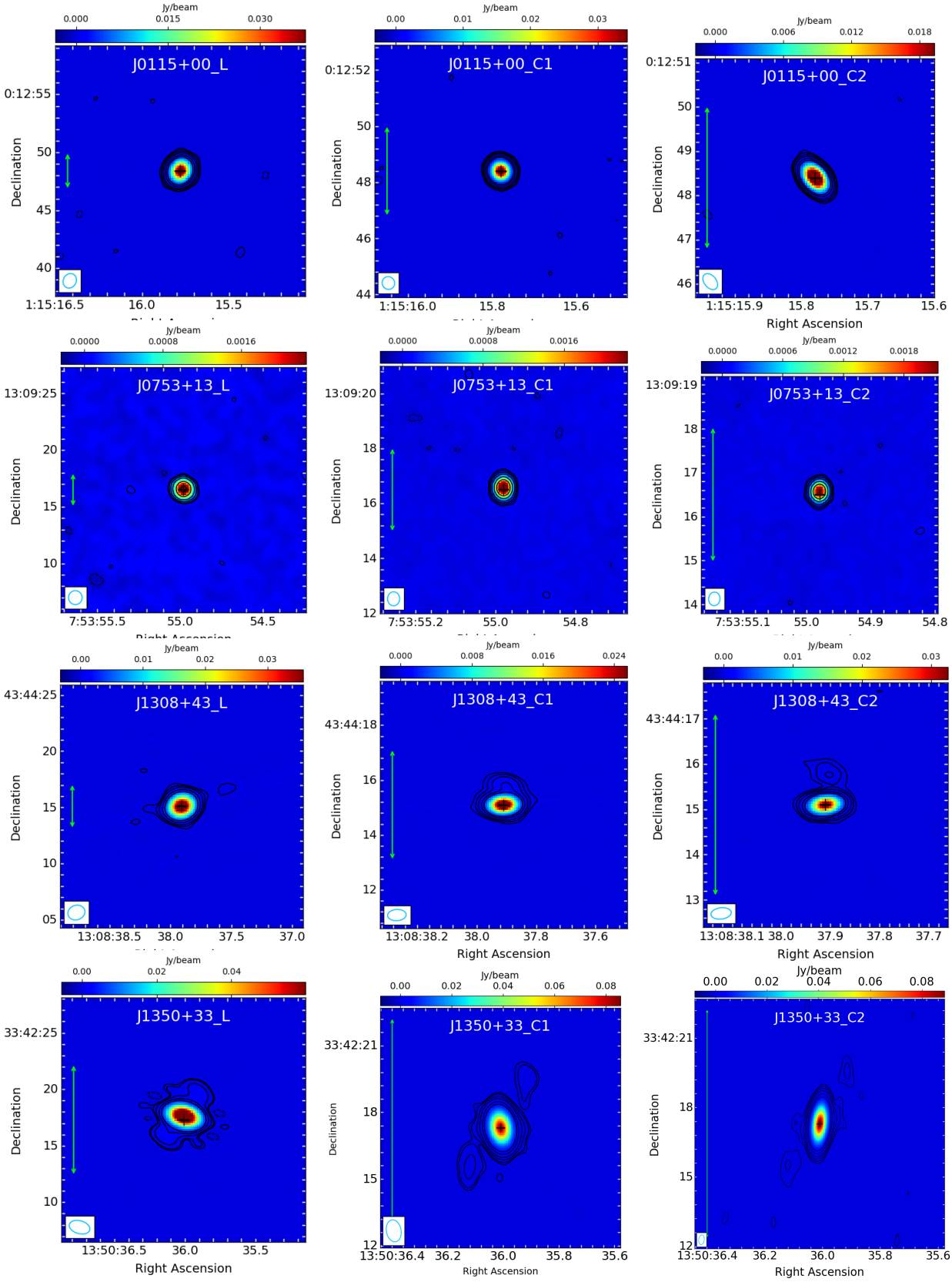

Figure 4.9: Selection of VLA radio maps of Project 2 sources after self-calibration, imaged using Briggs weighting (robust = 0.5). The maps are obtained at 1.5 GHz (L-band), 4.5 GHz (C1-band), and 7.5 GHz (C2-band). The remaining images are shown in Figure C.1, while the local rms and contour levels are listed in Table 4.3. The green arrow indicates a symbolic scale of 3 kpc, the beam is shown in the bottom-left corner, and the black cross marks the radio coordinate centre of each FR 0 source.

5

Results

In this chapter, we describe the procedures used to derive the flux densities F, which were then used to calculate the spectral indices, construct the spectral energy distributions (SEDs), and finally determine the radio luminosities and the core dominance of the sources in the analysed sample.

5.1 Flux densities

The flux density of the sources was inferred from three different emission regions:

- *The core region*, whose value was determined using the 2D fitting tool `imview` in `CASA`, which provides several parameters, including the *integrated* flux density $S_{\rm int}$ [mJy] and the *peak* flux density $S_{\rm peak}$ [mJy/beam]. Since most of the sources are compact and unresolved, with $S_{\rm int}/S_{\rm peak} \approx 1$, we adopted the peak flux density as a representative measure of the core emission throughout this analysis.
- *The total region*, evaluated using the highest confidence contour, typically the 3σ isophote, and at most the 5σ level.
- *The extended region*, defined using the same approach as the total region, the only difference being the exclusion of the nuclear (core) region from the traced contour.

Further details on the images used when extracting the flux densities will be underlined later; however, independently from the considered flux density, the total uncertainty on the flux density F is expressed in Equation 5.1, and includes several contributions added in quadrature. In the first term (i) there is the systematic error $\sigma_{\rm sys}$, which accounts for uncertainties in the flux density F calibration, which varies depending on the instrument involved in the observation. We considered 5% for the VLA (NRAO) and for NVSS (Condon et al., 1998), 3% for FIRST (White et al., 1994), and 10% for both LOFAR (Capetti et al., 2020a) and RACS (McConnell et al., 2020a). The second (ii) term includes the average thermal noise $\sigma_{\rm rms}$ measured directly in the map, scaled by the number of independent beams covering the source $n_{\rm beam}$, which is put to unity for unresolved sources. Lastly, the third (iii) term is an additional uncertainty σ_{2D}, included to account for the error introduced by the 2D-fit when measuring the core flux density.

$$\Delta F = \sqrt{\underbrace{(\sigma_{\rm sys} \cdot F)^2}_{\text{(i)}} + \underbrace{(\sigma_{\rm rms} \cdot \sqrt{n_{\rm beam}})^2}_{\text{(ii)}} + \underbrace{\sigma_{2D}^2}_{\text{(iii)}}} \tag{5.1}$$

Since our targets are predominantly unresolved and with a high SNR, Equation 5.1 in most cases can be simply approximated with $\Delta F \approx \sigma_{\rm sys} \cdot \mathrm{F}$.

The list of sources and their flux density measurements is presented in Tables 5.1 and 5.2. The initial inspection of the sources was typically performed using the 0.145 GHz LOFAR maps, from which approximately 20 targets were identified in the public DR2 catalog[1]. The remaining sources were obtained from individual LoTSS pointings located in the DR3 coverage area, to which we have privileged access. Observations at progressively higher frequencies were then included: 0.887 GHz images from RACS, followed by 1.4 GHz maps from the FIRST survey. Finally, the frequency range explored in this work was completed with the VLA data presented in Chapter 2, which included the 3.0 GHz S-band and high-resolution L- and C-band observations at 1.5, 4.5, and 7.5 GHz. This spectral coverage corresponds to a resolution range of approximately $\sim 0.3''$ to $25''$, resulting in projected sizes that range from scales of hundreds of parsecs to hundreds of kiloparsecs, providing the necessary observational leverage to trace radio emission across a wide range of physical scales.

The only radio maps that we did not directly analyse are the 1.4 GHz NVSS images, which offer an additional view on the FR 0s at $45''$ resolution, and for which we used the flux densities already provided by Baldi et al. (2018).

The flux densities reported in Tables 5.1 and 5.2 are not all derived from the self-calibrated images produced with Briggs weight and Robust=0.5, shown in Figures 4.9 and C.1, which we refer to as the *original resolution* maps. Instead, a substantial portion of the shown core flux densities was measured from images smoothed (indicated by the superscript *sm*) to a common resolution using the `CASA` task `imsmooth`, in order to perform a consistent beam-matched analysis and ensure a fair comparison across different interferometers/surveys.

In the case of Project 2, this resulted in the smoothing of all of C1 and C2 maps at the resolution of the L-band observations for core analysis. However, for Project 1, although the smoothed maps are not explicitly marked in Table 5.1 as no uniform convolution scheme was applied, all the spectral indices were computed from beam-matched maps. When considering the degraded maps, we registered a median increase in core flux densities of approximately 2.3% at 4.5 GHz and 3.8% at 7.5 GHz. This increase is attributed to the larger synthesised beams caused by the smoothing, which were doubled in size at 4.5 GHz and quadrupled at 7.5 GHz, thereby enclosing more extended emission.

This resolution-matching procedure was not applied to the total or extended flux densities, since a map with a degraded resolution could lose important details on its extended emission. Therefore, these flux densities were measured directly from the original resolution maps. To ensure that no extended emission was missed, we re-imaged the maps showing extended structures using a *natural weighting*, enhancing the contribution from shorter baselines, confirming a negligible difference in the total flux density ($\lesssim 3\%$).

[1] https://lofar-surveys.org/dr2_release.html

Name	$F_{0.145,\ \mathrm{core}}$	$F_{0.887,\ \mathrm{core}}$	F_{NVSS}	F_{FIRST}	$F_{3.0,\ \mathrm{core}}$
J0807+14	23.7 ± 2.8	27.8 ± 2.8	23.7 ± 1.2	25.5 ± 0.8	27.3 ± 1.4
J0910+18	108.5 ± 11.1	63.7 ± 6.4	50.0 ± 2.5	47.4 ± 1.4	30.9 ± 1.6
J0916+17	40.8 ± 4.1	27.3 ± 2.8	24.5 ± 1.2	14.55 ± 0.5	10.1 ± 0.5
J1044+43	23.5 ± 2.4	-	32.0 ± 1.6	23.2 ± 0.7	33.8 ± 1.7
J1722+30	23.0 ± 2.3	-	8.1 ± 0.4	5.7 ± 0.2	4.0 ± 0.2

Name	$F_{0.145,\mathrm{tot}}$	$F_{0.887,\mathrm{tot}}$	$F_{3.0,\ \mathrm{tot}}$	$F_{0.145,\ \mathrm{ext}}$	$F_{0.887,\ \mathrm{ext}}$	$F_{3.0,\ \mathrm{ext}}$
J0807+14	51.2 ± 5.11	39.5 ± 4.0	29.9 ± 1.5	27.3 ± 2.2	15.5 ± 1.6	3.8 ± 0.2
J0910+18	421.3 ± 42.2	141.1 ± 14.2	37.4 ± 1.9	280.9 ± 28.1	63.8 ± 6.5	< 6.94
J0916+17	100.2 ± 10.3	34.4 ± 3.5	14.6 ± 0.7	54.5 ± 5.5	-	4.4 ± 0.2
J1044+43	48.0 ± 4.7	-	36.3 ± 1.8	22.9 ± 2.3	-	3.0 ± 0.2
J1722+30	60.8 ± 6.1	-	5.0 ± 0.3	34.0 ± 1.7	-	< 1.11

Table 5.1: ID and flux densities [mJy] of the five sources in project 1. The top Table refers to the core component, but it features also the 1.4-GHz NVSS and FIRST data because they always see an unresolved target. The Bottom Table contains the total (tot) and extended (ext) flux densities. The subscript is referring to the central observational frequency, in GHz, of the map, aside for NVSS and FIRST that share the 1.4-GHz value. Thus, 0.145-GHz in LOFAR, 0.887-GHz in RACS, and 3.0-GHz for the VLA.

In the context of the first project, the extended emission in the five LOFAR-selected sources from Capetti et al. (2020a) was detected in only three of the corresponding VLA observations, while the remaining two sources–`J0910+18` and `J1722+30`–had only their cores detected. For the extended emission of these sources at 3.0-GHz we derived a flux density upper limit in the following way:

$$S_{\mathrm{lim}} = n \cdot \sigma_{\mathrm{rms,VLA}} \cdot \sqrt{N_{Beam}} \tag{5.2}$$

Where n=3 is the confidence factor, $\sigma_{\mathrm{rms,VLA}}$ is the map noise extracted from a very close region of the target and N_{Beam} is the number of beams covering the source.

Finally, in the last column of Table 5.2 we list the measured *jet-sidedness* (jet ratio) for the extended sources exhibiting a double-lobed structure. This quantity is simply defined as the ratio of the flux densities between the two jets and offers insights into the interaction between FR 0 radio jets and their surrounding environment, as well as a probe of the jet inclination along the line of sight.

For compact sources like FR 0s, estimating the jet-ratio is particularly challenging due to the difficulty in separating the extended jet emission from the nuclear component. For this reason, we present only the jet ratios derived from the high resolution VLA observations of Project 2. The measurement was performed on the map that provided the clearest view of the extended structures, typically the 7.5-GHz C2-band, with the exception of two source–`J1350+33` and `J0807+14`–where the L-band offered a better representation.

When a well-defined extended structure is present, such as in the cases of J1649+36 and J0807+14, isolating the flux density of the two jets, excluding the core, is relatively straightforward. In all other cases, the jet ratio was estimated by averaging measure-

Name	$F_{0.145}$ ± ∼10%	$F_{\rm NVSS}$ ± ∼5%	$F_{\rm FIRST}$ ± ∼3%	$F_{1.5}$ ± ∼5%	$F_{4.5}^{sm}$ ± ∼5%	$F_{7.5}^{sm}$ ± ∼5%	$F_{0.145,\rm tot}$ ± ∼10%	$F_{1.5,\rm tot}$ ± ∼5%	$F_{4.5,\rm tot}$ ± ∼5%	$F_{7.5,\rm tot}$ ± ∼5%	Jet ratio ± ∼20%
J0108−00	4.4	10.9	12.6	11.1	10.7	13.4	11.2	12.4	10.9	13.4	
J0112−00	6.1	17.9	18.3	16.8	13.7	11.1	15.6	14.8	13.8	11.2	
J0115+00	15.5	42.6	44.8	45.6	42.1	37.1	48.2	45.3	42.1	37.1	
J0753+13	1.2	7.4	12.1	3.2	3.4	2.7	1.7	3.0	3.3	2.7	
J0807+14	17.5	28.4	22.8	20.4	22.9	25.4	59.1	27.3	27.0	26.6	2.6
J0847+10	29.5	23.7	22.7	20.0	12.8	10.6	111.5	20.8	12.8	10.9	
J1018+00	4.6	14.3	5.1	5.7	2.4	1.7	15.3	6.1	2.5	1.6	
J1024+42	4.0	6.0	5.2	5.4	2.6	1.5	5.4	5.5	2.7	1.4	
J1048+04	104.6	49.1	45.3	47.3	29.4	23.9	354.2	50.5	29.7	24.1	
J1048+48	61.1	19.2	18.4	14.8	5.3	3.2	81.8	17.8	6.4	3.7	1.1
J1057+40	28.1	44.8	45.9	33.6	20.2	14.8	41.6	35.3	20.4	14.7	
J1120+04	8.2	7.5	7.1	7.5	4.8	4.3	29.1	7.8	5.0	4.3	
J1308+43	95.0	58.4	51.6	48.2	37.8	38.2	125.9	50.1	39.6	39.0	-
J1330+32	13.7	17.9	16.7	16.1	11.4	9.6	19.9	16.4	11.5	9.6	
J1341+29	9.3	10.4	9.3	7.7	6.9	6.1	12.2	7.8	6.9	6.2	
J1350+33	250.2	101.3	97.0	103.6	85.9	93.3	401.4	120.1	90.4	96.5	1.0
J1427+37	32.3	20.8	9.9	5.9	2.8	1.9	49.9	10.4	5.6	4.6	-
J1433+52	5.8	15.6	15.1	13.4	8.7	6.9	8.6	13.5	8.7	6.9	
J1521+07	22.5	11.7	5.8	4.3	1.8	1.1	22.5	6.1	2.6	1.5	1.3
J1541+45	9.5	8.9	5.2	5.4	3.3	2.5	33.3	5.5	3.4	2.7	
J1544+43	2.2	11.5	11.9	7.0	13.5	14.1	2.9	6.9	13.5	14.1	
J1544+47	28.8	17.6	17.0	17.7	12.4	9.8	33.2	18.1	12.4	9.8	
J1559+44	182.5	59.5	56.0	43.7	19.8	12.9	219.1	55.6	24.3	16.0	1.6
J1606+08	14.7	9.3	8.5	7.8	3.2	2.0	56.3	8.0	3.2	1.9	
J1612+09	27.4	21.7	19.8	18.6	7.8	5.2	112.0	20.1	8.0	5.2	
J1629+40	9.4	7.7	6.6	4.0	1.9	1.4	13.4	4.2	1.9	1.4	
J1649+36	28.6	11.9	8.4	3.1	1.7	1.4	40.9	11.5	5.5	3.8	1.1

Table 5.2: ID and flux densities [mJy] of the 27 FR 0s of Project 2. Column description: (1) ID, with names in bold indicating extended sources in the VLA maps; (2)–(4) LOFAR, NVSS, and FIRST core flux densities [mJy/beam]; (5)–(7) beam-matched VLA core flux densities [mJy/beam], while the superscript '*sm*' indicates the smoothed maps; (8)–(11) total flux densities from LOFAR and VLA maps at original resolution [mJy]; (12) jet ratio.

ments taken from different regions along the jets. For each region, two circular apertures were placed symmetrically on opposite sides of the core, at equal distances, while attempting to minimize contamination from the core itself.

5.1.1 Sizes

At the time of the flux density estimation, the largest angular scale (LAS) of each source was also retrieved, and reported in Tables 5.3. These angular sizes were then converted into projected largest linear sizes (LLS, see Figure 5.1) using the *Ned Wright Cosmology Calculator*[2]. The cosmological model adopted throughout this thesis is the default Planck-like cosmology provided by `NED` at the time of use[3], with $H_0 = 67.8$ $km \cdot s^{-1} \cdot Mpc^{-1}$, $\Omega_m = 0.308$, $\Omega_\Lambda = 0.692$. This means that $1''$ corresponds to $0.32 - 1.01$ kpc at $z = 0.015 - 0.05$.

When it comes to estimating the physical sizes of the sources, the unresolved targets provide limited information. For these cases, we only derived an upper limit on the size based on the major axis of the beam in the highest-resolution maps, namely the 3.0 GHz S-band and the 7.5 GHz C2-band from the VLA. In the second project, most of the sources (19 of 27) remain unresolved even at a resolution of $\sim 0.3''$, corresponding to a linear scale of 100-300 pc at $z \simeq 0.015 - 0.05$.

The extended radio emission was estimated using the "ruler" tool in `imview`, applied to the band with the lowest available resolution. An associated uncertainty due to the use of this tool was estimated to be on the order of $\lesssim 5\%$, based on repeated independent measurements of the same quantity. In Project 2, this corresponds to the 1.5 GHz L-band for the three FR 0s that are resolved across all VLA bands, and to the 4.5 GHz C1-band for the remaining five-six; displaying extended emission on scales smaller than 10 kpc, while in the first project they can reach up to ~ 50 kpc.

Project 1			
Name	**Morph**	**Size$_{VLA}$**	**Size$_{LOF}$**
J0807+14	Two-jets	22.07	62.63
J0910+18	-	<7.06	143.23
J0916+17	One-jet	52.71	72.04
J1044+43	-	<5.01	34.42
J1722+30	One-jet	39.4	59.49

Table 5.3: Morphology and linear size [kpc] of the VLA and LOFAR observations for sources in Project 1. Estimated error at $\lesssim 5\%$.

[2] http://www.astro.ucla.edu/~wright/CosmoCalc.html
[3] Comparable to the 2018 Planck cosmology (Planck Collaboration et al. 2020).

Project 2			
Name	**Morph**	**Size$_{VLA}$**	**Size$_{LOF}$**
J0108−00		<0.4	<6.1
J0112−00		<0.4	<6.1
J0115+00		<0.4	<6.1
J0753+13		<0.4	<6.1
J0807+14	Two-jets	8.5	62.6
J0847+10		<0.4	51.6
J1018+00		<0.4	<6.1
J1024+42		<0.4	<6.1
J1048+04		<0.4	27.0
J1048+48	Two-jets	2.3	28.9
J1057+40		<0.4	17.5
J1120+04		<0.4	33.0
J1308+43	One-jet	2.1	20.6

Project 2			
Name	**Morph**	**Size$_{VLA}$**	**Size$_{LOF}$**
J1330+32		<0.4	<6.1
J1341+29		<0.4	17.4
J1350+33	Two-jets	2.3	12.3
J1427+37	One-lobe	2.2	25.0
J1433+52		<0.4	<6.1
J1521+07	Two-jets	3.7	<6.1
J1541+45		<0.4	49.9
J1544+43		<0.4	<6.1
J1544+47		<0.4	<6.1
J1559+44	Two-jets	3.7	21.1
J1606+08		<0.4	35.7
J1612+09		<0.4	15.8
J1629+40		<0.4	14.7
J1649+36	Two-jets	5.3	15.7

Table 5.4: Morphology (as seen by the VLA) and linear size [kpc] from VLA and LOFAR observations for the sources in Project 2. Estimated error $\lesssim 5\%$.

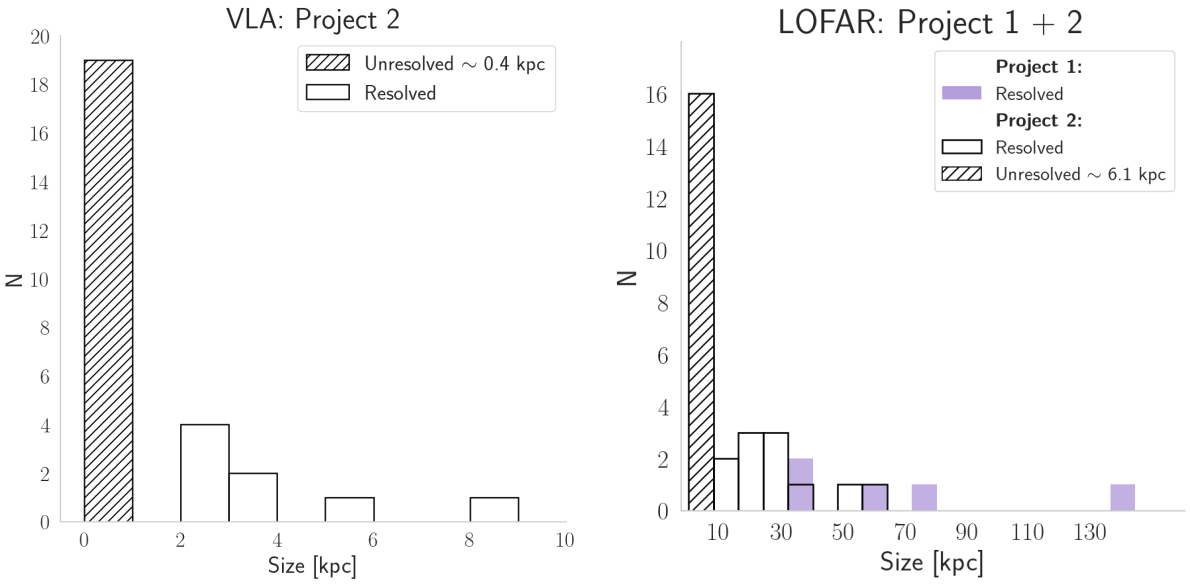

Figure 5.1: Linear size in kpc of the VLA (a) and LOFAR (b) observations. The five FR 0s of Project 1 are not shown in the VLA panel because they are out of scale ($20 \lesssim$ LLS [kpc] $\lesssim 50$). The hatch represents the unresolved sources.

5.2 Spectral analysis

The flux densities reported in Tables 5.1 and 5.2 were used to derive the spectral indices α for the corresponding emission components (core, total, and extended emission). The spectral index is a powerful diagnostic tool to probe the emission properties of each source, as it quantifies how the flux density F varies with frequency ν, according to the power-law $F \propto \nu^{-\alpha}$ already discussed in Section 1.1.4. It is calculated using the expression:

$$\alpha = -\frac{\ln\left(S_1/S_2\right)}{\ln\left(\nu_1/\nu_2\right)}, \tag{5.3}$$

with an associated uncertainty estimated using the standard error propagation applied to Equation 5.3:

$$\Delta\alpha = \left|\frac{1}{\log\left(\frac{\nu_1}{\nu_2}\right)}\right| \sqrt{\left(\frac{\Delta S_1}{S_1}\right)^2 + \left(\frac{\Delta S_2}{S_2}\right)^2} \tag{5.4}$$

The two projects had different focus, and aside from the nuclear region, we have usually included the results relative to the extended component for the five sources of project 1 and the results of the total component when dealing with the 27 sources of project 2.

As mentioned before, most spectral indices were computed using maps with the same resolution (beam-matched) and also same beam position angle (BPA). The cases where this was too detrimental, due to a significant disparity in resolution between different maps, a spectral index was still computed under the assumption that the source was compact at all frequencies. This condition represents the premise to freely compute spectral indices while neglecting the matching of image parameters (beam size and BPA). Conversely, an artificial steepening of the spectral slope may arise for extended sources if the maximum recoverable emission by the telescope is smaller than the extent of the sources, thus part of the emission is resolved out.

The spectral indices corresponding to the different regions of interest are listed in Tables 5.5 and 5.6. Focusing on Project 2, the results reveal the presence of a sub-kiloparsec flat-spectrum core ($|\alpha| < 0.5$) that steepens moving to higher frequencies, from 0.145 to 4.5 GHz, then it does not show a steepening between 4.5 and 7.5 GHz, remaining constant on average (see Figure 5.2). An opposite trend is observed for the total emission component, where the spectral index is steeper at lower frequencies (0.145–1.5 GHz) and progressively flattens at higher frequencies, as the extended emission becomes increasingly resolved out.

This general trend can also be seen in project 1, but it is not very significant due to the paucity of sources necessary for a statistical interpretation.In Table 5.5 we can see that four sources out of five (80%) from Project 1 exhibit a core with a flat spectrum in the 0.145–1.4 GHz range.

The extended emission of the five sources in Project 1 is instead always steep ($\alpha > 0.5$) or ultra-steep ($\alpha > 1$). This is consistent with the emission being produced by optically thin plasma from the extended radio lobes. In particular, sources J1722+30 and J0910+18 show ultra-steep spectrum emission, consistent with old ageing plasma, likely

	core			extended
Name	$\alpha^{\mathbf{1.4}}_{\mathbf{0.145}}$ ±0.05	$\alpha^{\mathbf{3.0}}_{\mathbf{1.4}}$ ±0.08	$\alpha^{\mathbf{3.0}}_{\mathbf{0.145}}$ ±0.04	$\alpha^{\mathbf{3.0}}_{\mathbf{0.145}}$ ±0.03
J0807+14	−0.03	−0.09	−0.05	0.65
J0910+18	0.37	0.56	0.41	> 1.22
J0916+17	0.38	0.71	0.46	0.83
J1044+43	0.01	−0.49	−0.12	0.68
J1722+30	0.62	0.48	0.58	> 1.13

Table 5.5: Columns: (1) source name; (2), (3) and (4) beam-matched core spectral index between LOFAR-FIRST, FIRST-VLA, LOFAR-VLA; (5) beam-matched extended spectral index between LOFAR-VLA.

not fuelled with fresh particles. Instead, the 27 sources of Project 2 (Table 5.6) predominantly exhibit flat spectra, with $-0.5 < \alpha < 0.5$ observed in 16 sources (approximately 60%) across both the 1.5–4.5 GHz and 4.5–7.5 GHz frequency intervals. The remaining 11 sources show steep spectra, characterised by $|\alpha| > 0.5$, as illustrated in Figure 5.2. Notably, one source, J0753+13, displays a strongly inverted spectrum at low frequencies (0.145–1.5 GHz), with $\alpha = -1.01$.

An alternative method to analyse the spectral shape of the FR 0 core spectra involves the use of spectral curvature (Fig. 5.3), defined as the difference between two spectral indices: $\alpha_{\rm high} - \alpha_{\rm low}$, where $\alpha_{\rm high}$ is computed at frequencies higher than $\alpha_{\rm low}$. A positive curvature indicates that the spectrum becomes steeper at higher frequencies, whereas a value near zero suggests a constant slope that spans both frequency regimes. Figure 5.3 illustrates the previously discussed trends for the core (left plot): the spectral steepening is particularly evident in the filled histogram, which captures the transition from the LOFAR to the VLA bands. However, this steepening becomes less pronounced in the higher frequency range of the C-bands (hatched histogram). In fact, as shown in Figure 5.2, the spectral index exhibits a clear steepening in the 0.145–1.5–4.5 GHz range, followed by a constant spectral slope in the 4.5–7.5 GHz interval.

Interestingly, eight sources exhibit mildly convex spectra in the LOFAR–VLA frequency range, with the 1.5 GHz flux density exceeding those at both 0.145 and 4.5 GHz by approximately 40% in each direction. These cases will be further explored in the discussion chapter (see Section 6.4) to better address the possibility of young FR 0s, and possibly infer if any of them show the diagnostic features of GPS objects.

When the analysis is restricted to the VLA bands (1.5–4.5–7.5 GHz), the number of convex spectra drops to a single case: `J0753+13`, which shows a flux density at 4.5 GHz that surpasses those at 1.5 and 7.5 GHz by ∼7% and ∼20%, respectively.

	core				total			
Name	$\alpha^{\mathbf{1.4}}_{\mathbf{0.145}}$ ±0.06	$\alpha^{\mathbf{1.5}}_{\mathbf{0.145}}$ ±0.06	$\alpha^{\mathbf{4.5}}_{\mathbf{1.5}}$ ±0.07	$\alpha^{\mathbf{7.5}}_{\mathbf{4.5}}$ ±0.15	$\alpha^{\mathbf{1.5}}_{\mathbf{0.145}}$ ±0.05	$\alpha^{\mathbf{1.5}}_{\mathbf{0.145}}$ ±0.05	$\alpha^{\mathbf{4.5}}_{\mathbf{1.5}}$ ±0.07	$\alpha^{\mathbf{7.5}}_{\mathbf{4.5}}$ ±0.14
J0108−00	−0.47	−0.40	0.03	−0.43	−0.059	−0.04	0.12	−0.40
J0112−00	−0.487	−0.44	0.19	0.41	−0.071	0.02	0.06	0.42
J0115+00	−0.468	−0.46	0.07	0.25	0.023	0.03	0.07	0.25
J0753+13	−1.013	−0.41	−0.06	0.45	−0.865	−0.23	−0.11	0.45
J0807+14	−0.117	−0.07	−0.11	−0.20	0.362	0.33	0.01	0.03
J0847+10	0.116	0.17	0.41	0.37	0.688	0.72	0.44	0.32
J1018+00	−0.041	−0.09	0.81	0.65	0.498	0.39	0.81	0.86
J1024+42	−0.118	−0.12	0.66	1.10	0.035	−0.01	0.64	1.29
J1048+04	0.369	0.34	0.43	0.40	0.887	0.83	0.48	0.41
J1048+48	0.529	0.61	0.94	1.00	0.649	0.65	0.93	1.09
J1057+40	−0.217	−0.08	0.46	0.60	−0.081	0.07	0.50	0.64
J1120+04	0.063	0.04	0.41	0.19	0.637	0.56	0.41	0.29
J1308+43	0.269	0.29	0.22	−0.02	0.393	0.39	0.22	0.03
J1330+32	−0.087	−0.07	0.32	0.34	0.074	0.08	0.33	0.34
J1341+29	−0.001	0.08	0.10	0.24	0.136	0.19	0.11	0.23
J1350+33	0.418	0.39	0.15	−0.16	0.615	0.52	0.26	−0.13
J1427+37	0.52	0.73	0.67	0.76	0.703	0.67	0.57	0.38
J1433+52	−0.421	−0.36	0.40	0.46	−0.232	−0.19	0.40	0.46
J1521+07	0.6	0.71	0.79	0.95	0.521	0.56	0.77	1.07
J1541+45	0.265	0.24	0.46	0.52	0.784	0.77	0.43	0.44
J1544+43	−0.75	−0.50	−0.60	−0.07	−0.626	−0.37	−0.61	−0.08
J1544+47	0.231	0.21	0.32	0.46	0.305	0.26	0.34	0.48
J1559+44	0.521	0.61	0.72	0.83	0.585	0.59	0.75	0.81
J1606+08	0.24	0.27	0.81	0.91	0.822	0.83	0.84	1.00
J1612+09	0.142	0.17	0.79	0.80	0.745	0.74	0.84	0.83
J1629+40	0.156	0.37	0.69	0.53	0.31	0.50	0.72	0.64
J1649+36	0.541	0.95	0.54	0.35	0.635	0.54	0.67	0.75

Table 5.6: Spectral indices for Project 2. Columns: (1) source name; (2–5) core spectral indices; (6–9) total spectral indices. The superscripts and subscripts refer to the frequencies [GHz] employed: 0.145-GHz LOFAR, 1.4-GHz FIRST, 1.5-GHz L-band VLA, 4.5-GHz C(1)-band of the VLA and C(2)-band of the VLA.

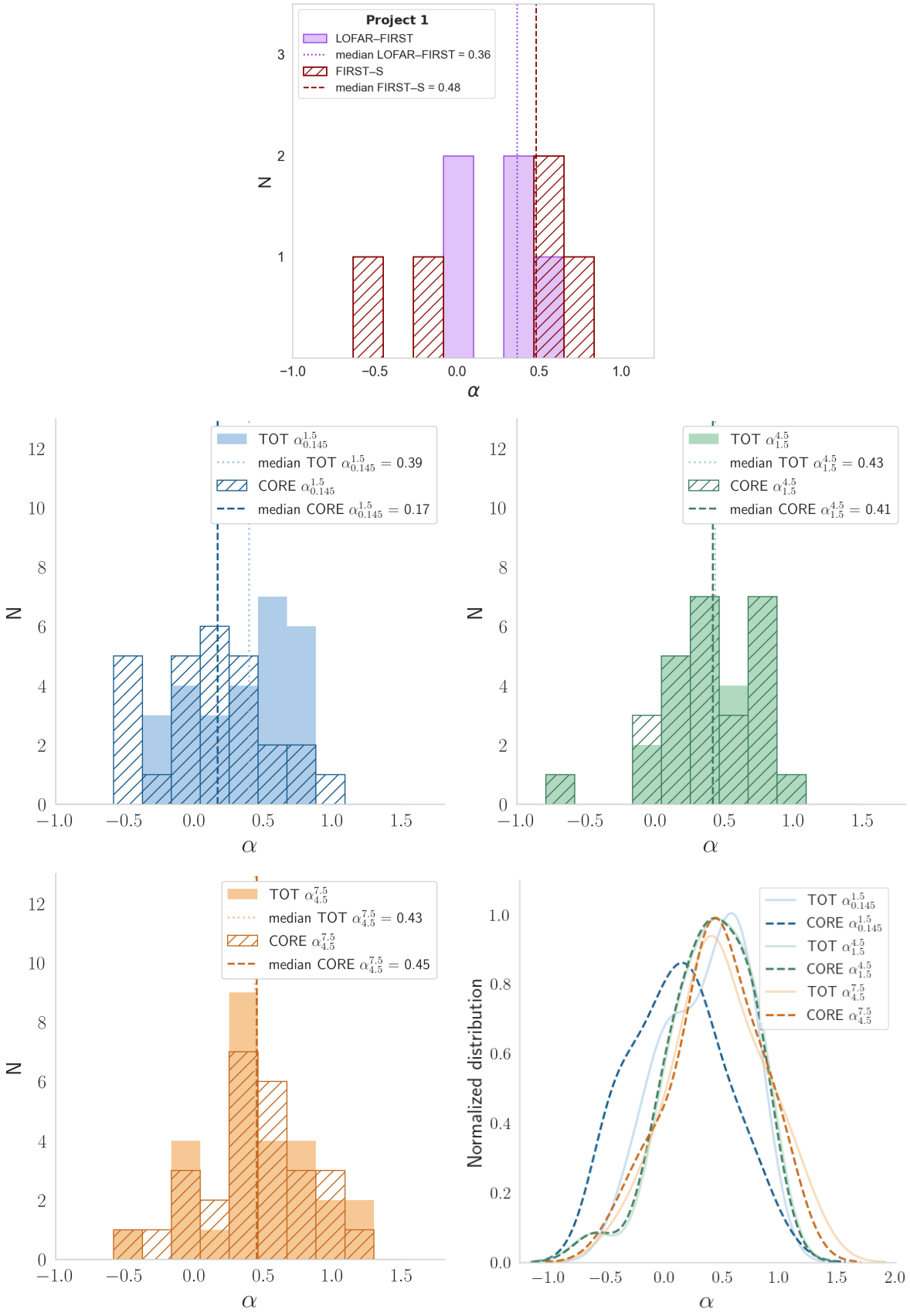

Figure 5.2: Top: core spectral index distribution of the 5 FR 0s in Project 1. Bottom: Spectral index distributions of the 27 FR 0s in Project 2 for the core (hatched) and total (filled) component. Bottom-right: Kernel density estimations (KDEs) for the total (solid curves) and nuclear (dashed curves) spectral indices.

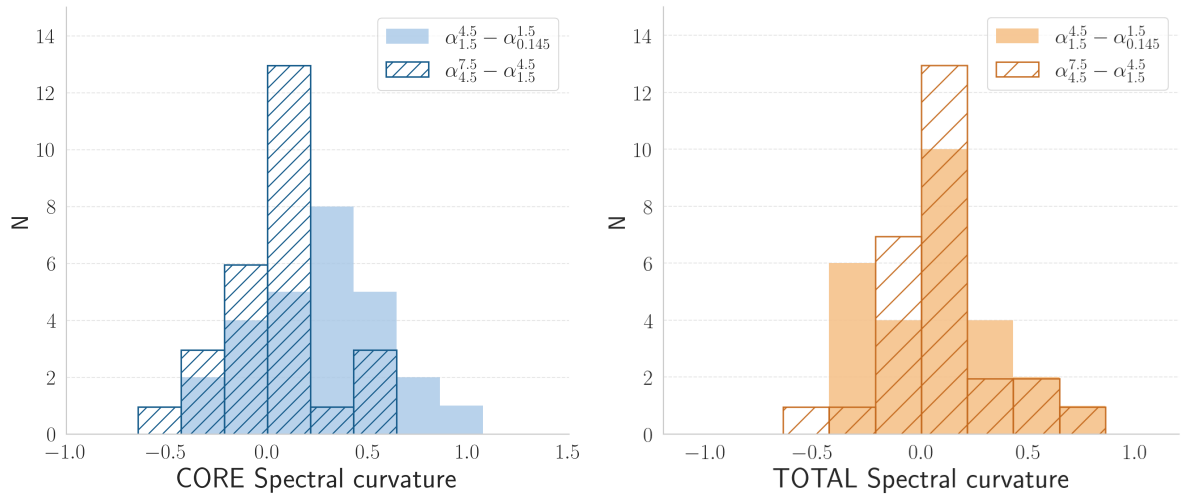

Figure 5.3: Distribution of the spectral curvatures computed using the core (left plot) and total (right plot) spectral indices. The frequencies [GHz] used are: 0.145 (LOFAR), 1.5 (JVLA-L), 4.5 (JVLA-C1), 7.5 (JVLA-C2).

5.2.1 Spectral Energy Distribution (SED)

To further investigate the radio spectral properties, we used the previously measured flux densities and spectral indices to construct the SEDs shown in Figures 5.4, 5.5 and D.1, covering all 32 sources. Wherever possible, beam-matched spectral indices were adopted to reduce the technical diversity that comes with different instrumental observations. Cases where this approach could not be applied are explicitly noted in the figure captions. For clarity, only the most relevant components are shown in the SED plots—primarily the core and extended emission—while total component was included only when it exhibits a significant departure from the core spectral behaviour.

On one hand, the SEDs of the core component of the 32 FR 0s show different global shapes: the majority has a flat spectral behaviour (12/32), while only 8 sources show a monotonic steep spectral distribution. The remaining 12 FR 0s display a spectral change from a flat to steep or from a steep to flat spectrum. On the other hand, the total or extended emission has generally a steeper spectrum than that of the central core.

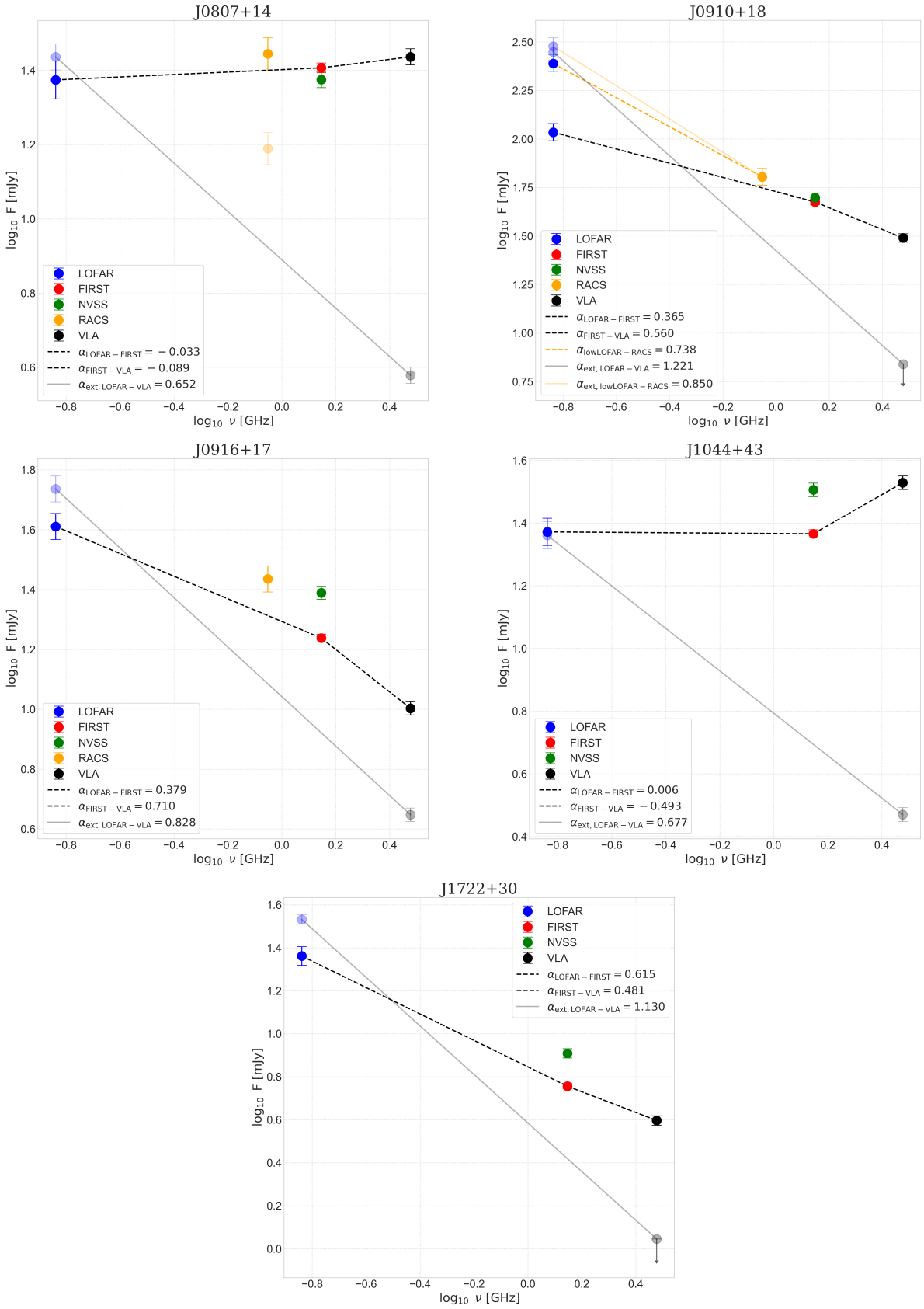

Figure 5.4: Beam-matched SED of the five sources of project 1. The dashed lines refers always to the nuclear (core) components, while the lighter continuous lines and points to the extended components (not the total).

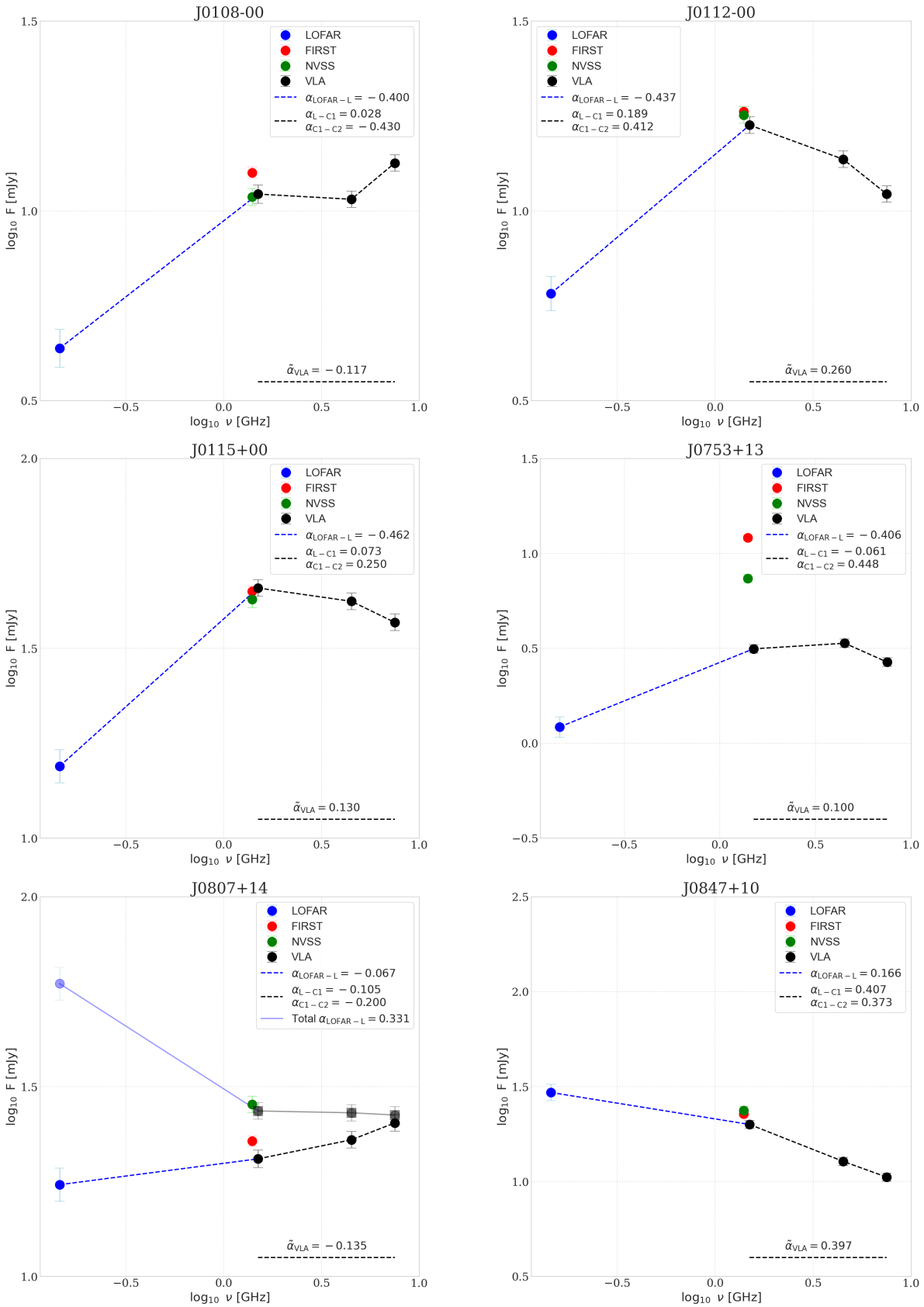

Figure 5.5: Selection of the radio SED of the sources in Project 2, the remaining images are shown in Figure D.1. The dashed lines refers always to the nuclear (core) components, while the lighter continuous lines and points to the total components. The short dashed line in the bottom-right corner is the average core spectral index for the beam matched VLA maps, from 1.5 to 7.5 GHz.

5.2.2 Luminosity and core dominance

Finally, we use the spectral indices α and the flux densities F presented before to compute the characteristic monochromatic radio power for each data point presented in the SED plots (Figures 5.4 and 5.5) through the relation:

$$L = 4\pi D_L^2 F(\nu)(1+z)^{\alpha-1}$$

$$= 1.13 \cdot 10^{24} \left(\frac{D_L}{\mathrm{Mpc}}\right)^2 \left(\frac{F}{\mathrm{mJy}}\right)(1+z)^{\alpha-1} \quad [\mathrm{erg \cdot s^{-1} \cdot Hz^{-1}}] \tag{5.5}$$

The last line of Equation 5.5 was further multiplied by the central frequency of the observed band, $\Delta\nu$, in order to express the luminosity in units of erg/s. D_L is the luminosity distance, which is a cosmologically dependent parameter defined as $D_L = (1+z)D_C$, where D_C is the cosmological comoving distance[4].The factor $(1+z)^{\alpha-1}$ represents the K-correction, which corrects the observed monochromatic flux to account for redshift effects and renormalizes it to the rest-frame of the source. However, in this study, the impact of the K-correction is negligible due to the low redshift of the sample ($z < 0.05$), implying that the resulting luminosities across different facilities and surveys are primarily determined by the flux densities themselves.

We also estimated the Eddington ratio λ_{edd} for the whole sample, defined as the ratio between the bolometric and Eddington luminosities. The bolometric luminosity, for low-luminosity AGN, can be inferred through the empirical relation $L_{Bol} = 3500\, L_{[\mathrm{OIII}]}$, described by Heckman et al. (2004), while the Eddington luminosity was already described in Equation 1.3.

The Eddington ratios, which can be considered as proxy for the accretion rate, are displayed in Tables 5.7 and 5.8, as well as in the left plot of Figure 5.8. The median λ_{edd} value (in logarithmic scale) is -4.51 and -3.24, respectively for Project 1 and Project 2, both of which below the nominal threshold between high and low accretion rate set at $\sim$ 10% ($log(\lambda_{edd}) = -2$), and therefore consistent with the radiatively inefficient accretion flows typically expected from low-excitation radio galaxies (LERGs) (Heckman and Best, 2014).

In the right plot in Fig. 5.8 are presented the values of the core dominance R, defined as the ratio between the nuclear and the total component, as seen in the maps at the highest and lowest resolutions available, respectively. The total component is always offered by the 1.4-GHz NVSS map at $\sim 45''$, while the core component is the 7.5-GHz VLA map at $\sim 0.3''$ for the Project 2, and the 3.0-GHz VLA maps at $\sim$ 7–10$''$ for Project 1. In this case, we preferred to make use of the new observed data of the VLA instead of using the higher resolution offered at 1.4-GHz by FIRST. The histograms with the radio-core and NVSS total luminosity are showed in Figures 5.6 and 5.7.

Flat-spectrum sources ($|\alpha| < 0.5$ at 7.5 GHz) have values $\log(R)$ in the range $-0.74 < \log R < 0.09$, while steep-spectrum sources yielded lower values ($-1.40 < \log R < -0.06$) due to a non-negligible extended component that increases the total flux density. This pattern is well depicted in Fig. 5.9, where the resolved sources generally have lower core dominance ($\log(\mathrm{R}) \to -1$), but it is not the case for the last five FR 0s of Project 1, which display a very high core dominance despite being among the most extended sources in

[4]Obtained from astro.ucla.edu.

FR0CAT. This could be explained by the way the core dominance was computed: in this case it was used a lower resolution VLA map to trace the nuclear emission, which probably could not disentangle efficiently the core component from the extended one, introducing an additional contribution that inflates the core dominance. This appears to be the case for Project 1, where the linear core dominance shows a median increase by a factor of 1.84 when using the VLA map instead of the FIRST image.

Name	$\mathbf{L_{0.145,\ core}}$	$\mathbf{L_{3.0,\ core}}$	$\mathbf{L_{0.145,\ ext}}$	$\mathbf{L_{3.0,\ ext}}$	$\lambda_{\mathbf{edd}}$	**R**
J0807+14	37.81	39.18	37.88	38.34	-4.07	0.06
J0910+18	38.46	39.24	38.89	38.59	-4.42	0.62
J0916+17	38.04	38.75	38.17	38.39	-5.02	-0.39
J1044+43	37.67	39.13	37.66	38.09	-4.80	0.23
J1722+30	38.21	38.75	38.39	38.21	-4.51	-0.31

Table 5.7: Logarithmic core and extended radio luminosities at 0.145 GHz (LOFAR) and 3.0 GHz (VLA-S) [erg·s^{-1}]. The associated error on the log quantity is approximately 2% and 4% for the VLA and LOFAR luminosities, respectively. The last two columns report the logarithmic Eddington λ_{edd} ratio and core dominance R= $\log_{10}(L_{\mathrm{S,core}}/L_{\mathrm{NVSS}})$.

Table 5.8: Logarithmic core and extended radio luminosities at 0.145 GHz (LOFAR) and 7.5 GHz (VLA-C2) [erg·s^{-1}]. The last two columns report the logarithmic Eddington λ_{edd} ratio and core dominance $\log_{10}(L_{\mathrm{C2,\ core}}/L_{\mathrm{NVSS}})$.

Name	$\mathbf{L_{0.145,\ core}}$	$\mathbf{L_{7.5,\ core}}$	$\mathbf{L_{0.145,\ tot}}$	$\mathbf{L_{7.5,\ tot}}$	$\lambda_{\mathbf{edd}}$	**R**
J0108−00	37.45	39.65	37.87	39.66	-3.09	0.09
J0112−00	37.57	39.56	37.99	39.56	-3.46	-0.21
J0115+00	37.99	40.10	38.50	40.10	-3.43	-0.06
J0753+13	36.96	39.03	37.10	39.01	-3.99	-0.46
J0807+14	37.71	39.58	38.24	39.61	-3.73	-0.06
J0847+10	38.37	39.64	38.96	39.66	-3.62	-0.37
J1018+00	37.56	38.86	38.10	38.83	-1.60	-0.96
J1024+42	37.40	38.71	37.53	38.67	-3.48	-0.64
J1048+04	38.62	39.70	39.16	39.70	-2.70	-0.42
J1048+48	38.54	38.98	38.67	39.04	-2.04	-0.92
J1057+40	37.77	39.22	37.94	39.21	-3.80	-0.49
J1120+04	37.84	39.27	38.40	39.28	-3.01	-0.28
J1308+43	38.61	39.93	38.74	39.94	-3.10	-0.20
J1330+32	37.72	39.28	37.88	39.28	-2.67	-0.28
J1341+29	37.80	39.33	37.92	39.33	-3.04	-0.24
J1350+33	38.24	39.53	38.45	39.54	-3.14	-0.04
J1427+37	38.06	38.55	38.25	38.92	-4.09	-1.40
J1433+52	37.63	39.43	37.80	39.42	-3.24	-0.38
J1521+07	38.19	38.60	38.18	38.73	-3.92	-1.30
J1541+45	37.63	38.77	38.18	38.81	-3.27	-0.57
J1544+43	36.98	39.51	37.10	39.50	-3.23	0.08

Continued on next page

J1544+47	38.13	39.39	38.20	39.38	-3.36	-0.27
J1559+44	39.03	39.60	39.11	39.69	-2.72	-1.00
J1606+08	38.05	38.91	38.64	38.89	-2.87	-0.70
J1612+09	37.42	38.41	38.03	38.41	-3.41	-0.64
J1629+40	37.41	38.31	37.57	38.30	-3.95	-0.74
J1649+36	37.98	38.38	38.13	38.80	-3.21	-1.15

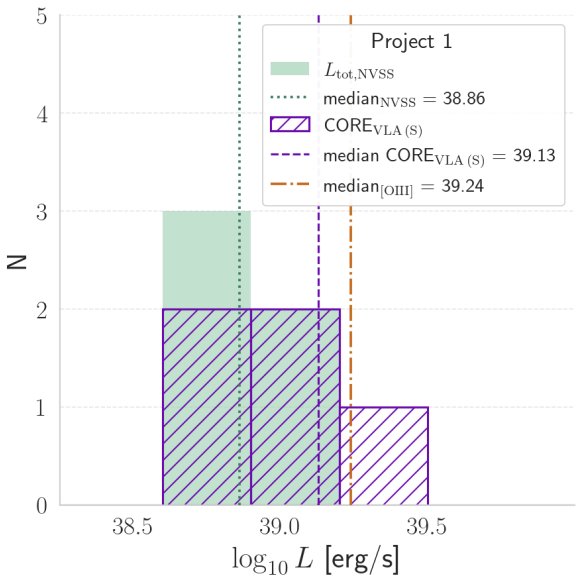

Figure 5.6: Distribution of the monochromatic 1.4-GHz NVSS and 3.0-GHz VLA core luminosities in Project 1.

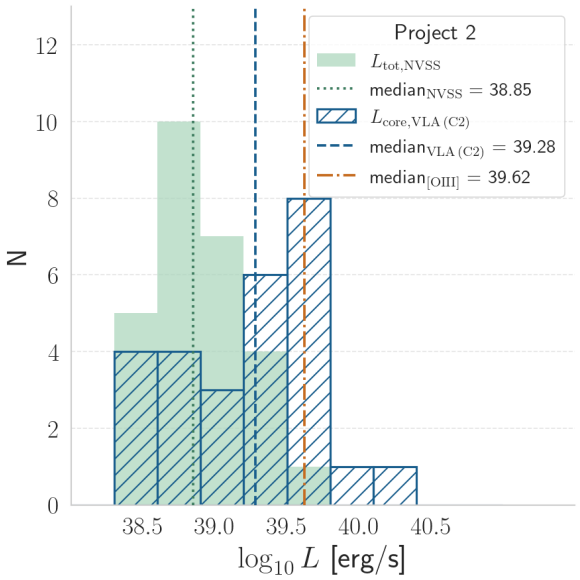

Figure 5.7: Distribution of the monochromatic 1.4-GHz NVSS and 7.5-GHz JVLA core luminosities in Project 2.

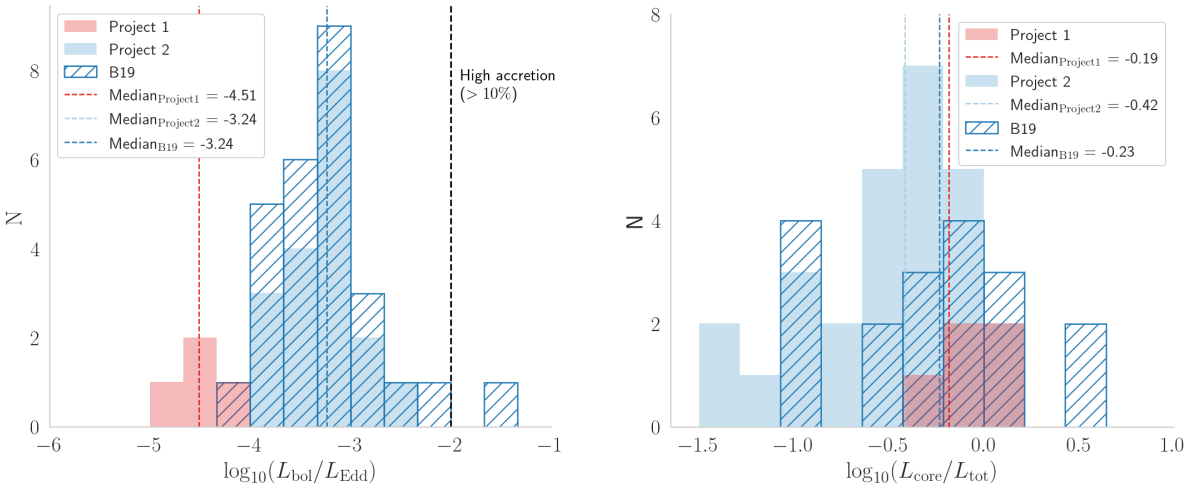

Figure 5.8: Distribution of Eddington ratio (left) and core dominance (right) for the 32 FR 0s of this thesis: Project 1 sources in red and Project 2 sources in light blue, and also the 18 sources from Baldi et al. (2019a), here called B19 (blue hatched histograms).

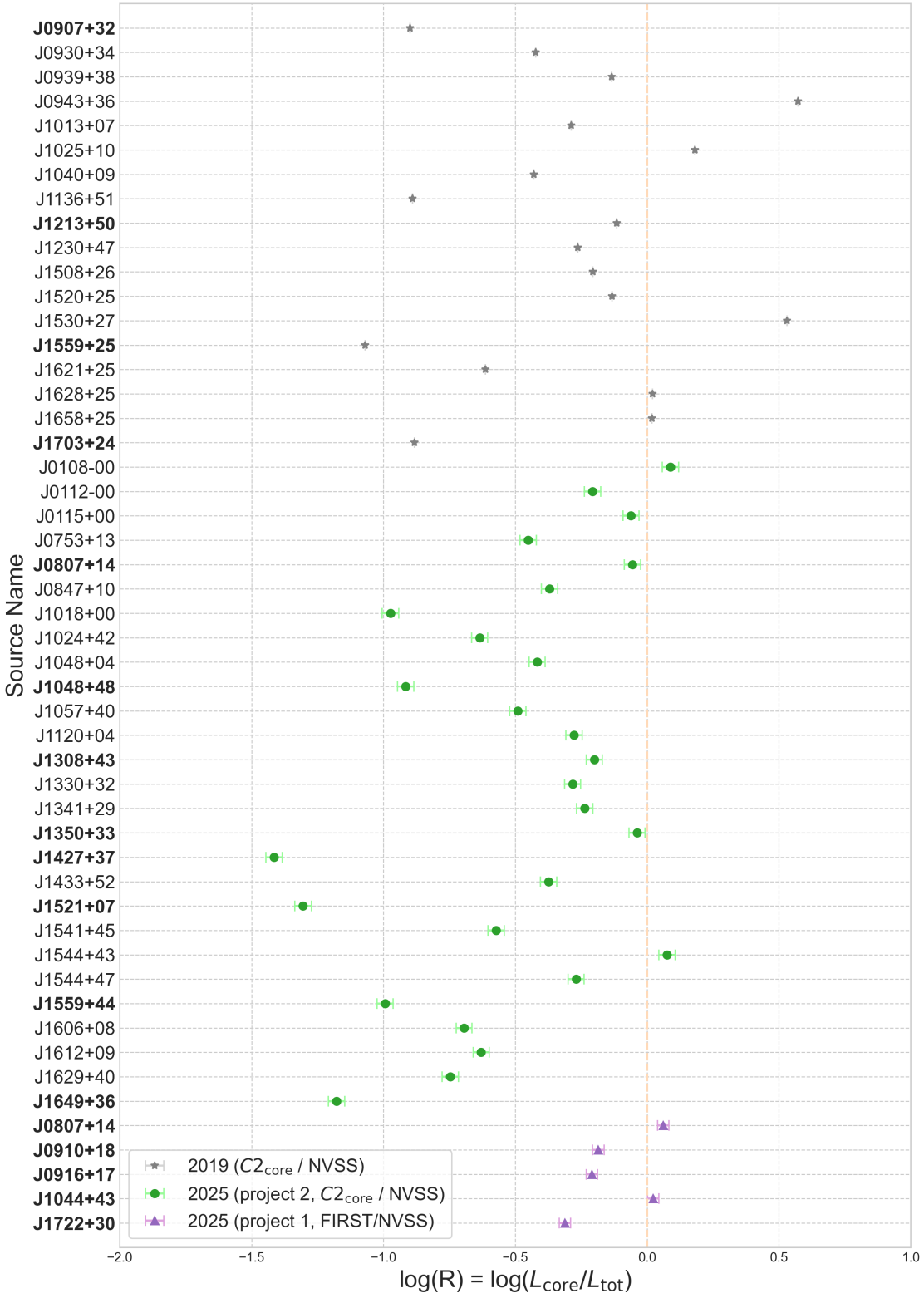

Figure 5.9: Core dominance R for the 32 sources of this thesis, separated in project 1 and project 2, plus the sample of 19 FR 0s of Baldi et al. (2019a). The log(R)=0 dashed line points the position of perfectly core-dominated objects $L_{\rm core}/L_{\rm tot} = 1$. In the x-axis is written the SDSS name (short form) of each point, the names in bold font represent the resolved sources (4 in 2019, 5 in Project 1, and 8 in Project 2).

6

Scientific discussion

This chapter summarises and discusses our findings in Chapter 5, presenting the relationships among the physical quantities of the AGN, jet and host properties that may be correlated. As mentioned when presenting the sample, this work is not the first subsample extracted from the 104 sources of the FR0CAT catalogue, thus it will also exploit the results of the works that gave life to this follow-up, Capetti et al. (2020a) and Baldi et al. (2019a). The structure will primarily focus on the following aspects: morphology, core emission, and extended emission. This framework allows us to investigate the behaviour of the individual emission components for the 32 FR 0s, assessing the nature of their compactness and jet structure.

6.1 Morphology

The inclusion of FR 0s in the Fanaroff-Riley classification allows a direct comparison with the canonical FR I and FR II radio galaxies. From an optical point of view, the differences between these populations are subtle, as all are predominantly hosted by red massive ETGs (Baldi 2023). In contrast, radio observations reveal marked distinctions, particularly at kiloparsec-scales. At parsec-scales, also the radio morphological differences are less pronounced, particularly from FR Is. However, on larger scales, FR 0s lack the defining structural features of their counterparts; namely, the edge-brightening morphology seen in FR IIs and the edge-darkening morphology in FR Is. Moreover, FR 0s typically do not exhibit extended jets or lobes at kpc scale; instead, they appear mostly unresolved in radio maps with arcsecond resolution.

The radio morphological characterization of the entire sample is provided in Table 5.3 of Chapter 5, which summarizes the general properties. Among the 32 FR 0s, the majority of sources remain unresolved on scales smaller than a few kiloparsecs. Thanks to the new high-resolution observations, 11 exhibit extended radio emission: three from Project 1 and eight from Project 2, with median linear sizes of 39.4 kpc and 6.9 kpc, respectively. Most FR 0s, when resolved, generally show radio structures that are collimated, often distorted, and rapidly declining in brightness as the distance from the core increases. This is typical of sources with low-power jets, and we observe this effect both in the VLA and LOFAR frequencies, with a higher tendency for the VLA maps to feature a two-jets structure ($\sim 67\%$) than the LOFAR maps ($\sim 50\%$). This trend of morphology change with frequency disfavours, as argued also by Capetti et al. (2020a), the scenario

where these extended structures are remnants from a prior activity phases, which instead usually show diffuse halos that form when the energy supply from the jet ceases (Brienza, M. et al. 2016). Interesting is the case of J1427+37, that shows extended emission seen at 0.150, 4.5, 7.5 GHz with an increase progression in the transition from a single jet (0.145-GHz) to a hint of double jet toward 7.5-GHz. This source is labelled as a single-jet, but higher frequency (or deeper) observations could unveil an even more pronounced double-jet structure. Instead, J0807+14, the source common to the two projects whose extended emission was observed at 0.150, 0.887, 1.5, 3.0, 4.5, 7.5 GHz, at lower resolutions (0.150, 0.887, and 3.0 GHz), appears one-sided, with extended emission only on the western side. When we look at it with high-resolution at 1.5 GHz, the eastern jet emerges, forming a two-sided structure that becomes increasingly dominated by the eastern jet at higher frequencies. By 7.5 GHz, the emission is entirely confined to the eastern side, making the source fully one-sided in that direction. Lastly, some sources—J1018+00, J1308+43, J1427+37, and J1521+07—exhibit very close unrelated radio components, which lack optical counterparts, except for J1018+00, whose two nearby sources are identified as stars.

The main result is that $\sim 60\%$ of the sample, still appear compact in the available images; however, this classification is strongly dependent on spatial resolution, sensitivity, and observing frequency. It is not uncommon for higher observational resolution with VLBI technique to reveal previously unresolved extended emission, which was initially interpreted as a flat-spectrum core. This is exemplified by the case studies of Cheng and An (2018); Chen et al. (2021); Giovannini et al. (2023), who found that approximately 80% of their FR 0 sources exhibit resolved jet structures that extend for a few parsecs. Therefore, due to the absence of a complete objective method for categorising a source as compact, we limited ourselves to assigning the 'compact' label to sources that appear unresolved in the given observation, setting an upper limit for the linear size based on the highest available resolution. In the second project this resulted in 19 ($\sim 70\%$) sources with a linear size of ~ 0.4 kpc at 7.5 GHz, which is consistent with Baldi et al. (2019a) at the same frequency, who found a ratio between unresolved-resolved FR 0s of two to one. In contrast, we have a surplus of three extended radio sources at 0.150 GHz, for a total of 11 ($\sim 40\%$) out of 27, which is almost the double with respect to the number found by Capetti et al. (2020a), where just $\sim 20\%$ of their sample, composed of 66-sources, showed extended emission at 0.150 GHz.

In Project 1, the five sources appeared extended in LOFAR, but only in three the extended emission was at least partially visible with the VLA observations. For the two unresolved cases, we used the resolution (beam) of the map to set upper limits on their core sizes at ~ 5 and ~ 7 kpc. One of these two, J0910+18, was also observed through VLBI by Cheng and An (2018), and appears unresolved also on the mas-scale. This source was the most bright and well documented object in the first project, displaying a bright central core embedded in a plateau of diffuse radio emission, identified by the low-resolution (20") LOFAR image as the central portion of a large and elongated radio structure, stretching over approximately $4'$ (about 150 kpc). The other source where the extended emission is not recovered by the VLA is J1722+30, which in LOFAR presents a pair of two rather symmetric S-shaped jets extending for about 20 kpc.

6.2 Exploring the FR 0 compactness

By combining the sources from Project 2 with the sample of Baldi et al. (2019a) and Capetti et al. (2020a), the fraction of unresolved sources is 75% in both VLA and LOFAR observations. Independently of the data used, FR 0s can therefore be defined quite safely as compact objects, with the high resolution VLA that constrain them to be resolved at less than 1 kpc.

This severe lack of extended radio emission in FR 0s does not seem to be supported by the scenario in which they represent an early evolutionary phase that would eventually develop into FR Is, given enough time to grow large-scale radio structures. This hypothesis was already tested and rejected by Baldi et al. (2018), and further examined with the high resolution VLA observations of Baldi et al. (2019a), who simulated the growth at a constant cosmological pace of the FR0CAT sample, setting the fraction of resolved to unresolved sources based on their sub-sample, giving them enough time to develop the $\sim$ 100 kpc radio structures seen in FR Is. However, even when accounting for selection biases (see Baldi et al. 2018 for more details), they still observed a factor $\sim$ 2 of discrepancy in their number densities, strongly suggesting that FR 0s are not simply young FR Is in formation—at least, not all of them— but rather a distinct population which dominates the local radio Universe. By adding the 27 newly observed FR 0s at high resolution from Project 2, the estimated ratio of resolved to unresolved sources in the whole FR0CAT sample changed by a factor of only +1.07, compared to the earlier estimate based on the 18 sources from Baldi et al. (2019a). We did not simulate the evolution of our sample, but this modest variation should at least support the assumption that the previously determined FR 0-to-FR I number ratio remains valid.

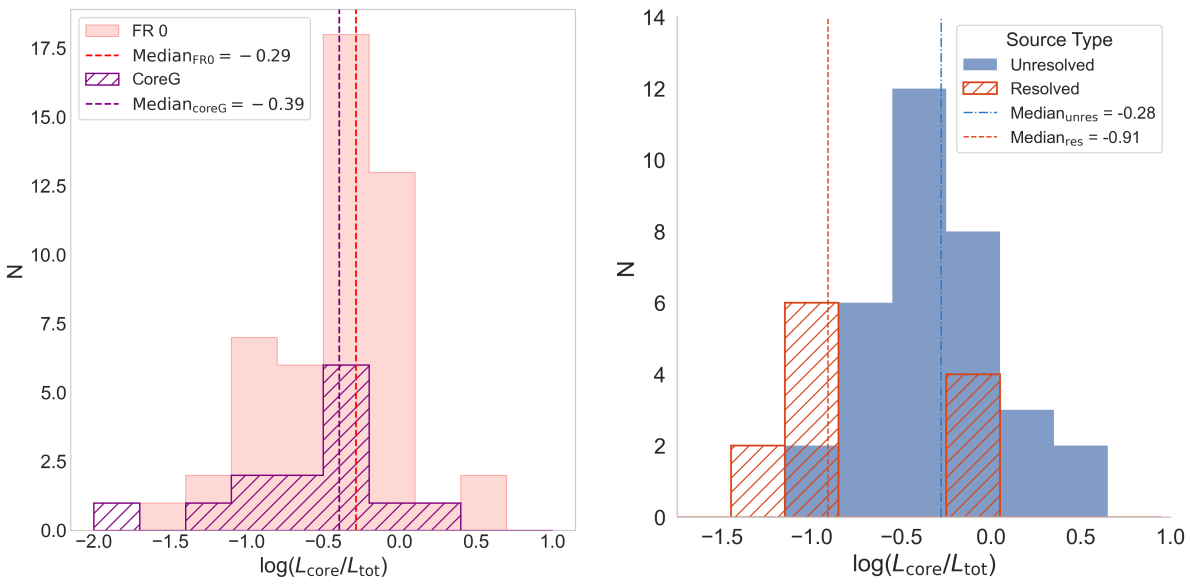

Figure 6.1: (Left) Core dominance of 49 FR 0s (Projects 1,2 and Baldi et al. 2019a) and coreG (Baldi and Capetti, 2009). (Right) Core dominance of the high resolution sample (Project 2 and Baldi et al. 2019a), dividing between resolved (hatched histogram) and unresolved (filled histogram) sources.

The size distribution of FR 0 radio galaxies also imposes significant constraints on the hypothesis that they are short-lived, recurrent sources. Shin et al. (2012) found that more massive galaxies tend to remain in active states for longer periods than their satellite counterparts. However, attributing the sharp peak observed in the size (< 1 kpc) distribution to this effect seems implausible and hard to test, given that the average mass difference between FR 0 and FR I host galaxies is relatively modest—only a factor of 1.6—with considerable overlap between the two populations (Baldi et al. 2018; Miraghaei and Best 2017). That said, the possibility of a recurrent state is not unlikely since some FR 0s have exhibited low to moderate radio flux density variability over multi-year timescales (Cheng and An 2018, Mikhailov and Sotnikova 2021). While this variability does not necessarily indicate recurrent nuclear activity, it is still an expected phenomenon in the evolutionary life of the radio source.

However, even if the cause for such compactness is not known, the consequence of their compactness is captured by the core dominance R, which is one of the founding features of FR 0s and clearly indicates the lack of extended radio structures. It was already shown in Figure 5.8, and now we represent it again alongside the observed distribution of CoreG sources. The left plot of Figure 6.1 show that the core dominance of FR 0s is very similar to that of the coreG. From other studies (Baldi and Capetti, 2009; Baldi et al., 2019a), we know that the core dominance of FR 0s can be as high as ~ 30 times that of FR Is, even when they share the same nuclear and host properties. If we look deeper at the core dominance using the sample of FR 0s at high resolution (right plot of Figure 6.1), we note a clear distinction between resolved and unresolved sources, with the former exhibiting a median core dominance approximately three times higher than that of the latter. However, since nearly 70% of FR 0s typically display a compact morphology, this simply highlights that while extended structures can contribute to the overall radio emission, the core dominance of the bulk of the FR 0s population is more reliably characterized by the unresolved sources, which show a median logarithmic value of approximately -0.28; nearly identical to the median core dominance of -0.29 of the total sample without distinctions (left plot in Figure 6.1).

One possible origin of the high core dominance is related to the environmental properties which can set the accretion onto the SMBH and/or contribute to confine the jet emission. For this purpose, we investigated potential correlations between the radio properties of the sources in our sample and the characteristics of their host galaxies, probing on the possibility that a combination between radio properties and black hole mass and host galaxy mass would return a positive connection. We plotted the core dominance against the available spectral indices/curvatures, the BH mass and the Eddington ratio, but no significant trends were found in these attempts.

Another aspect driving the compactness could be the Mpc-scale environment, which has a cosmological impact on the evolution of the radio galaxy population (since it can probe the dark matter halo). For this scope, we considered the number of cosmological neighbours[1] found in the surroundings of the Mpc scale. Using the cosmological neighbours computed by Capetti et al. (2020b) for the entire FR0CAT sample, we have confronted in Table 6.1 the number of cosmological neighbours for various datasets, to test if there is a statistical difference in clustering properties between the resolved and the

[1] Massaro et al. (2019) defined as 'cosmological neighbours', $N_{\rm cn}^{2000}$, all galaxies located within a region of a given projected radius (they mostly used a radius of 2 Mpc) and whose spectroscopic redshift z differed by less than 0.005 from the radio galaxy in the centre of the field they examined using SDSS data.

unresolved FR 0s with respect to the FR I which are keen to reside in richer environment.

		$N_{\rm cn}^{2000}$	
Sample	N	Median	Average
FR0CAT	104	13	21.95
FRICAT	219	38	40.11
Project 1,2 + B19	49	11	19.46

Table 6.1: Cosmological neighbours within 2 Mpc for different sample. Column description: (1) Sample corresponding to Baldi et al. (2018), Capetti et al. (2017b), the 49 FR 0s from the sample of this thesis (just 31 because one is shared between the projects) and Baldi et al. (2019a), here called B19; (2) number of sources in the sample; (3-4) median and average number of cosmological neighbours within 2 kpc $N_{\rm cn}^{2000}$.

In Table 6.1, we evaluated whether the sample selected for this thesis exhibits any significant deviation in behaviour compared to the entire FR0CAT sample. Our analysis indicates that this is not the case. We also investigated potential differences between resolved and unresolved sources. The resolved sources from the 49 FR 0s, comprised of the sample of this thesis and the one of Baldi et al. (2019a), have a median $N_{\rm cn}^{2000}$ of 12 (and average of 25.86), while the unresolved sources have a median value of 11 (and average of 16.68). These results demonstrate that our sources are well within the typical range of $N_{\rm cn}^{2000}$ observed for the complete FR0CAT sample. Consequently, we find no evidence suggesting that, for instance, resolved FR0s reside in denser environments comparable to those of FR Is.

The influence of the environment remains therefore uncertain, primarily due to the confinement of most FR 0s radio structures within their host cores, shielding them from the larger-scale environment. To probe a little more on the cause of this extended emission, which mostly manifest in the shape of low-power jets, we need to go back at the origin of this emission: the nuclear (core) region. Starting from the place where the jets are ejected at the sub-pc scale, we will walk through the emission regions that were resolved by the available observations; which will interest the 100-1000 pc scale of the core emission, and finally the extended resolved structures visible in the kpc scale.

6.3 Accretion-ejection mechanism

The place where the jet originates, the launch site, is probably the main reason behind the compactness of FR 0s; but could this trait be the result of a different accretion–ejection mechanism? Does the central engine work differently than the one in FR Is? What is the nature of the jets?

To investigate these questions, we employed the diagnostic plot in Figure 6.2, that compares the luminosity of the [O III] emission line, an isotropic proxy for the AGN radiative output (Heckman et al. 2004), with the core radio luminosity[2] produced by the

[2]Selected from the highest available resolution VLA band: 3.0 GHz (S-band) for Project 1 and 7.5 GHz (C2-band) for Project 2.

AGN. Although our sample includes sources from two different projects with notably different angular resolutions ($\sim 8''$ vs $\sim 0.4''$), we consider them together, with the caveat that Project 1 data may include a greater contribution from extended emission blended with the core, and therefore is better to consider its points as upper limits.

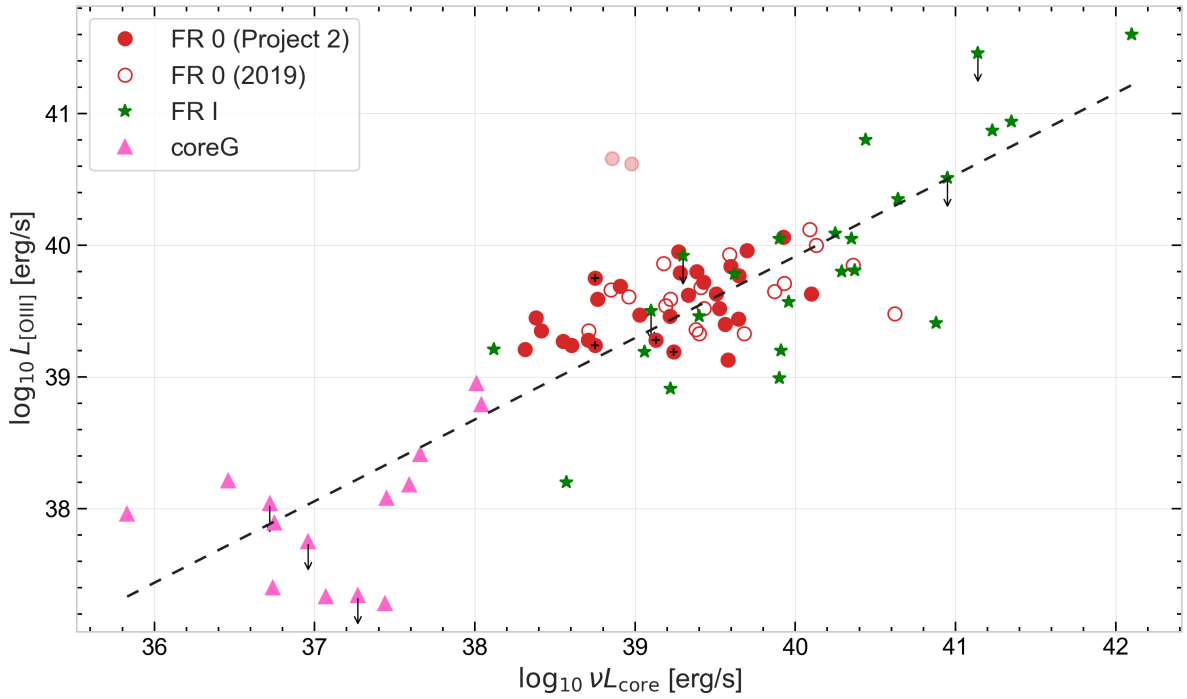

Figure 6.2: Core radio power at 7.5 GHz (Project 2) and 3.0 GHz (Project 1) versus [O III] line luminosity for 14 CoreGs (pink triangles) at 5.0 GHz, 24 3C/FRI (green asterisks) at 5.0 GHz, and 49 FR 0s (red dots) composed by the 19 of Baldi et al. (2019a) (open red cirles) and the 27 of Project 2 (filled red cirles) and 4 of the sources of Project 1 (filled red circles with cross inside). The two light red dots are RQ-AGN that were excluded. The dashed line indicates the linear fit of all the displayed points (minus the two RQ outliers), which has a Spearman and Pearson correlation coefficients of 0.77 and 0.88 with a p-value of $4.6 \cdot 10^{-18}$ and $3.7 \cdot 10^{-28}$, respectively.

Some considerations on Figure 6.2: for the source `J0807+14`, which is shared between the two Projects, we only plotted the high resolution value of Project 2. Additionally, two sources—`J1018+00` and `J1048+48`—are believed to be RQ-AGN based on their excess in [O III] luminosity with respect to the radio core luminosity. A posteriori, by checking their host properties, we can see that they also have host parameters more similar to late-type galaxies compared to the bulk of the FR0CAT sources, particularly `J1018+00`. These two are included in the plot for completeness in a light red color, but excluded from the statistical analysis.

Overall, Figure 6.2 shows that FR 0s occupy the same region as the low-luminosity tail of the FR Is distribution, following the same core-[O III] emission line correlation observed in FR Is and CoreGs. This continuity reinforces the similarity between the nuclear properties of FR 0s and FR Is, highlighting the subtle distinctions among AGN classes. Rather than forming discrete populations, these objects appear to span a continuous distribution in accretion power, with FR 0s representing the low-luminosity extension of

the FR I class and low Eddington ratios, consistent with a radiatively inefficient accretion disks (Heckman and Best, 2014).

However, we note that seven FR 0s in Baldi et al. (2019a) and eleven additional sources in Project 2 exhibit steep core spectral indices ($\alpha > 0.5$), suggesting the presence of unresolved extended emission. As a result, the constraint on the true core emission, and thus on the actual jet launching site, is less robust for these sources. The core luminosities for these sources can technically be considered as upper-limit measurements of the core component. Although the correlation becomes less precise due to these upper limits, the connection between the two populations remains statistically supported. This result supports the hypothesis that, in the region of the central engine (< 1 kpc), the launching of the jet must be similar to those of FR Is. However, since the resolved radio emission of most FR 0s fades rapidly beyond the core implies that, on larger scales (> 1 kpc), some mechanism inhibits the formation of extended jet structures. This possibility will be further investigated when studying the extended emission in Section 6.5.

The coupling between accretion and ejection can also be investigated by comparing the core dominance—a proxy for the jet brightness structure (i.e., how prominently the core outshines the extended jet emission)—and the Eddington ratio (Figure 6.3).

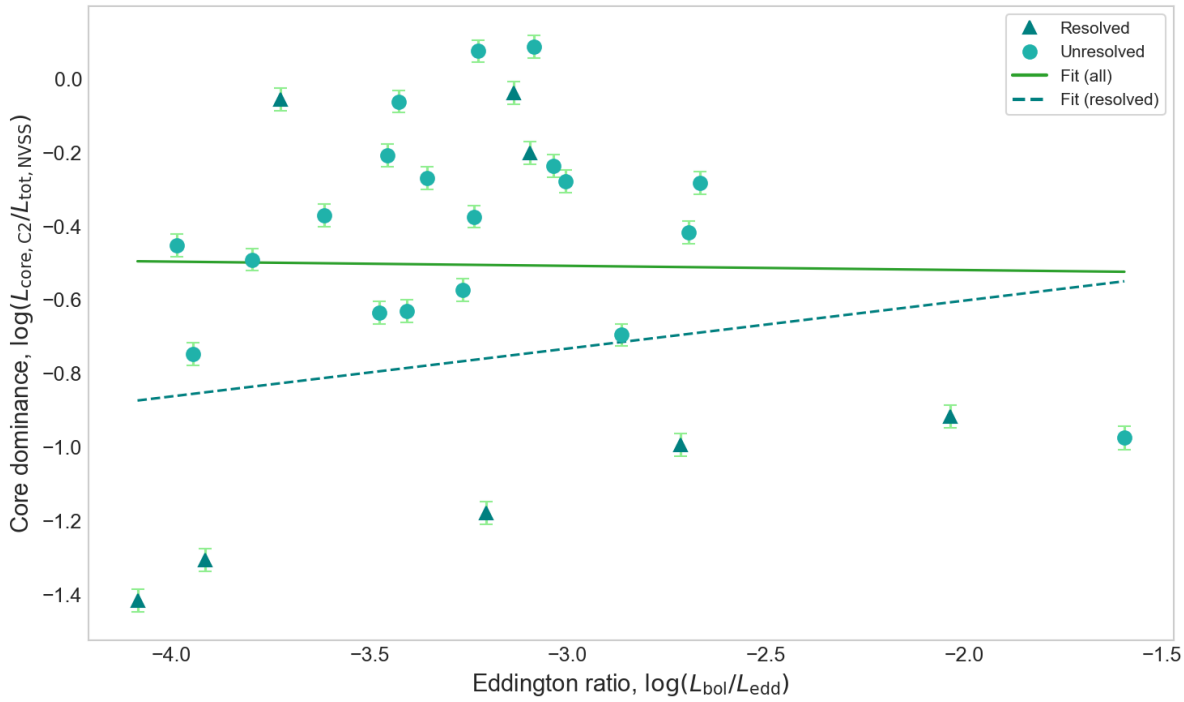

Figure 6.3: Eddington ratio vs core dominance, with the separation between resolved and unresolved 27 sources of project 2. All FR 0s are accreting at very low Eddington ratios, but the production of the compact jet does not seem to depend on the accretion, as the Spearman test provides < 0.5 for all three fits.

Figure 6.3 did not provide any significant correlation; therefore, we also tried to couple the Eddington ratio to other quantities (spectral indices/curvatures, BH mass, core radio luminosities) and it did not result in any significant connection, probably because the considered quantities have a very small spread ($\lesssim 1$ dex) and the properties

of FR 0s are better seen in a continuous distribution of radio galaxies, as was in Figure 6.2.

6.4 Radio core properties

The analysis derived from the $L_{[OIII]}$ - L_{core} luminosity points at the similarities in the nuclear region between FR 0s and FR Is, but does not answer the question of what kind of phenomena cause such similarities, for which a deeper study through VLBI is needed to resolve the milliarcsecond region ($\sim$ 0.001 kpc at z=0.05). As a result, a convincing explanation of the internal mechanisms governing FR 0s activity—especially those leading to such a reduced radio output compared to FR Is—remains largely debated. To gain further insight on the core region, we now shift our perspective toward spectral analysis, in particular to the sub-kpc flat-spectrum component that characterises the majority of FR0s.

From the spectral analysis presented in Section 5.2 it was revealed a tendency of the spectral index to steep up from the interval 0.145-1.5 and 1.5-4.5 GHz (see Figure 5.2, with a difference between median values of $\Delta\alpha_1 = \alpha_{1.5}^{4.5} - \alpha_{0.145}^{1.5} \sim 0.24$, but the result might be slightly hampered by the non beam-matched $\alpha_{0.145}^{1.5}$. Instead, there was no sign of further steepening for the spectral index defined between 4.5-7.5 GHz, consistent with Baldi et al. (2019a).

An additional tool to explore the spectral behaviour is the radio color-color plot in Figure 6.4, which compares the spectral index at low versus high frequencies. Inside this plot, the gray areas locate the region for a spectral index to be considered reasonably flat, in this case $|\alpha| \leq 0.4$ instead of $|\alpha| \leq 0.5$ to account for the bigger errors of the color-color plot with respect to a simple spectral index. The bisector is occupied by the sources that have similar spectral indices at low and high frequencies, exhibiting therefore a constant power-slope in that frequency range. Points below the bisector display the classic synchrotron steepening at higher frequencies, which may result from radiative ageing of the electron population or the superposition of multiple spectral components with decreasing intensity at higher frequencies.

In contrast, sources above the bisector show spectral flattening toward higher frequencies, suggesting the emergence of an optically thick component, possibly due to a self-absorbed or flat-spectrum core that dominates at higher frequency. However, most of the sources confirm the results already found: a steepening between 0.145-1.5-4.5 GHz (left plot), and a flat spectral slope between the VLA bands (right plot), especially in the range 4.5-7.5 GHz, resulting in a general convex radio SED. We also place, as reference, the color-color plot of the total component (Figure 6.5), and see that very few differences are present, particularly at higher frequencies.

As discussed before, not all FR 0s can be young RGs waiting to grow, but a fraction of these sources could be genuinely young, with a narrow-peaked spectrum that arises from the combination of a single optically thick component at low frequencies and an optically thin component at high frequencies. Eight sources exhibited sufficiently convex spectra to be fitted using a logarithmic parabola (Figure 6.6), to test whether they meet the criteria to be classified as GPS sources. The previous work by Capetti, A. et al. (2019) pointed out that $\lesssim 15\%$ of the FR 0s could present a genuine low-frequency cut-off, and consequently be interpreted as young compact objects. However, they selected only sources with a 1.4-GHz NVSS flux > 50 mJy; therefore, a statistical analysis on a

large sample of FR 0s is needed to assess the fraction of young radio galaxies among CRSs.

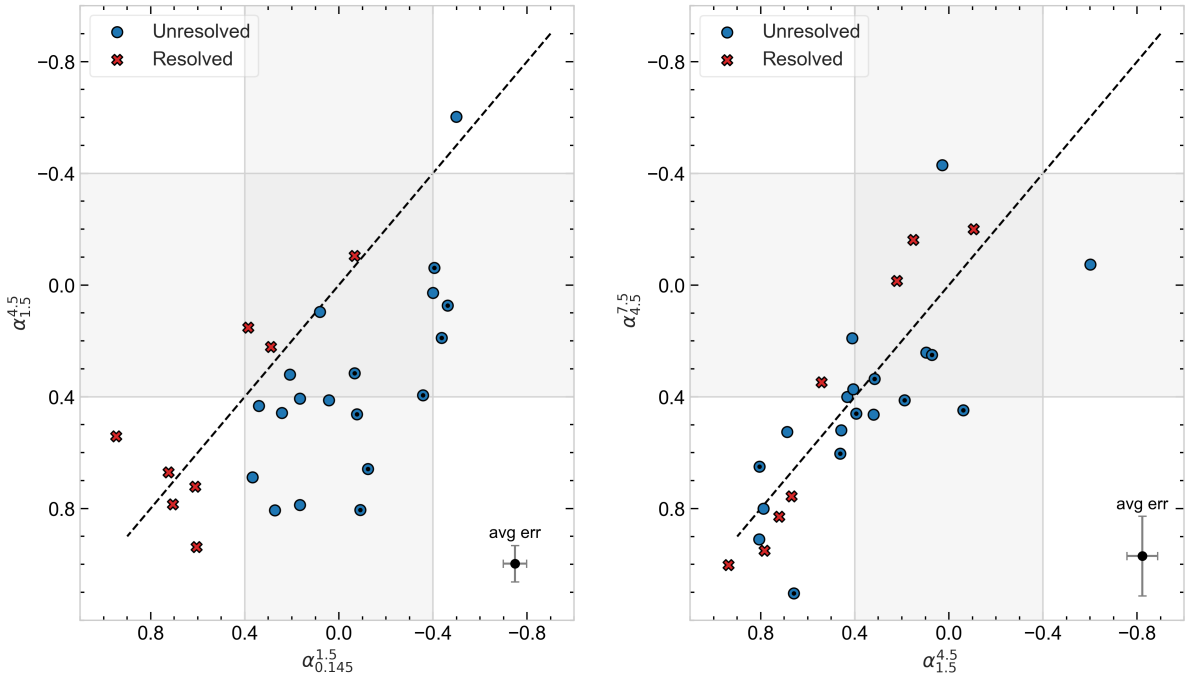

Figure 6.4: Color-color plot, of the core emission, using the LOFAR (0.145 GHz) and VLA bands (1.5,4.5,7.5 GHz). the points with a black dot inside are the convex spectrum sources.

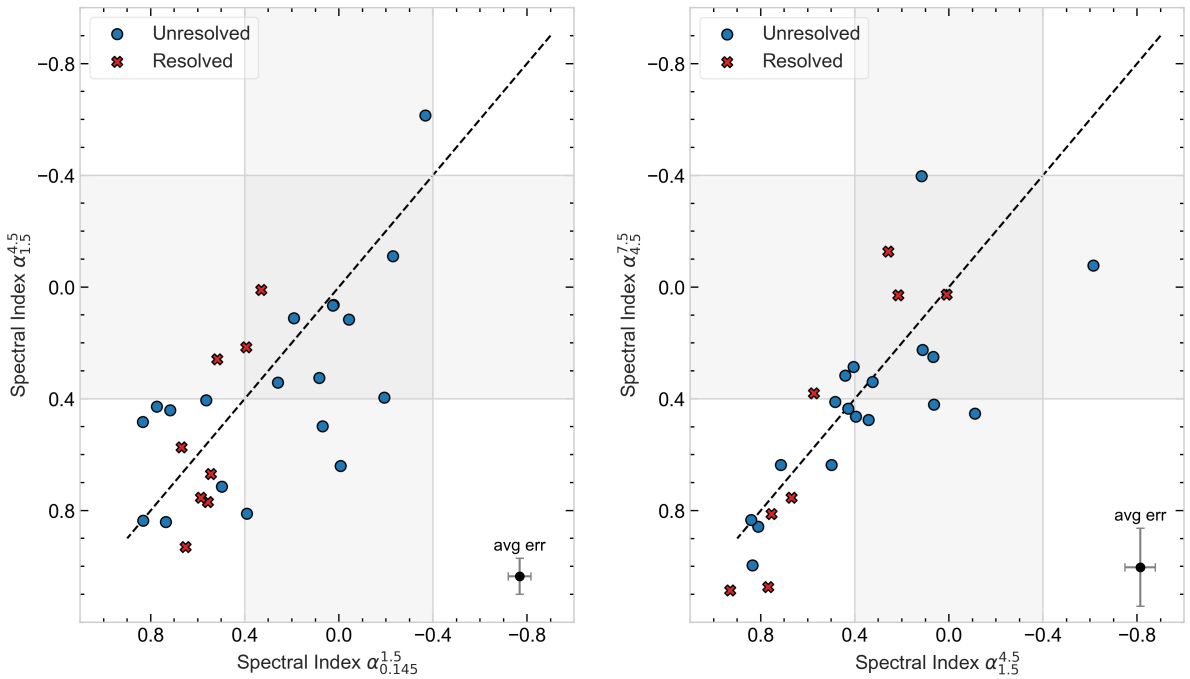

Figure 6.5: Color-color plot, of the total emission, using the LOFAR (0.145 GHz) and VLA bands (1.5,4.5,7.5 GHz).

The model we adopted is a first degree approximation of the one used in O'Dea et al. (1991), centred around the peak, and defined as:

$$\log S(\nu) = \log S_{\rm m} - b\,(\log \nu - \log \nu_{\rm m})^2$$

where $S(\nu)$ is the flux density at frequency ν, $S_{\rm m}$ is the maximum flux density, $\nu_{\rm m}$ is the turnover frequency at which the spectrum peaks and b is a curvature parameter that describes the width of the spectral peak. This model provides a good approximation of the synchrotron emission produced by a compact, homogeneous region undergoing self-absorption, as typically expected in GPS sources. From the curvature parameter b, we derived the full width at half maximum (FWHM) of the spectral peak using the relation:

$$\mathrm{FWHM} = 2\sqrt{\frac{1}{2b}}$$

The distribution of FWHM values for our eight sources was compared to that of the GPS sources analyzed by O'Dea (see Figure 6.7). Notably, our median FWHM of 2.32 is in excellent agreement with the value reported by Capetti, A. et al. (2019) ($\sim$2.32). Although our sample generally exhibits a median FWHM 1 dex larger than the typical one found by O'Dea at ~ 1.20, we still identify at least one source with FWHM<2 dex, and another one with a very close value to that threshold. This could then be considered consistent with the findings of Capetti, A. et al. (2019) and their estimate, which sees 10–15% of the FR 0s as probable GPS.

The low number of GPS candidates is not surprising, as the FR0CAT sample is selected from 1.4 GHz surveys, potentially excluding sources that peak at ~ 1 GHz, and therefore a more compelling argument—regarding the GPS-like nature of FR 0s—would come from a selected sample that also covers a possible peak at lower frequencies. Furthermore, We remind that complex spectral shapes may also be the result of variability of the source, given the fact that the data points used were collected at different times. Simultaneous observations should be performed to discern between genuine GPS candidates, from those that simply have spikes in variability. Overall, aside from the selection biases, we did not expect a large number of GPS because FR 0s typically lack the abrupt transition from an optically thick to thin state characteristic of GPS. Instead, their spectral features are better characterized by a gradual steepening toward higher frequencies, from 0.145 to 4.5 GHz in this work, as already shown in Figure 6.4).

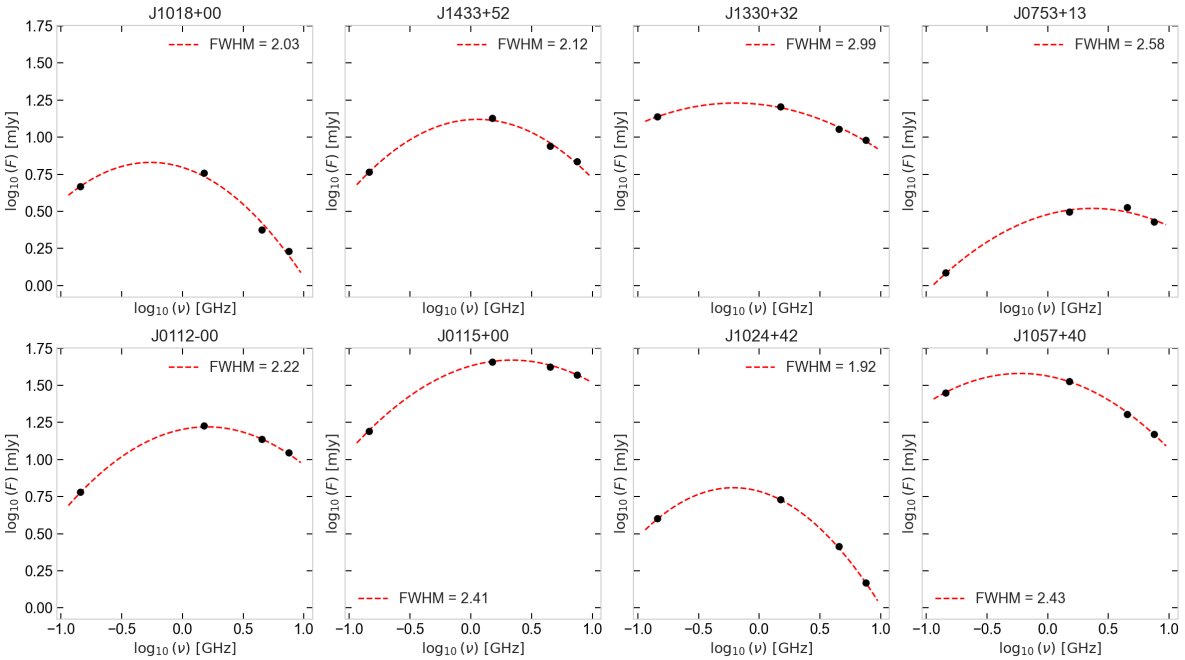

Figure 6.6: log-parabola fit of the eight convex-spectrum FR 0 sources.

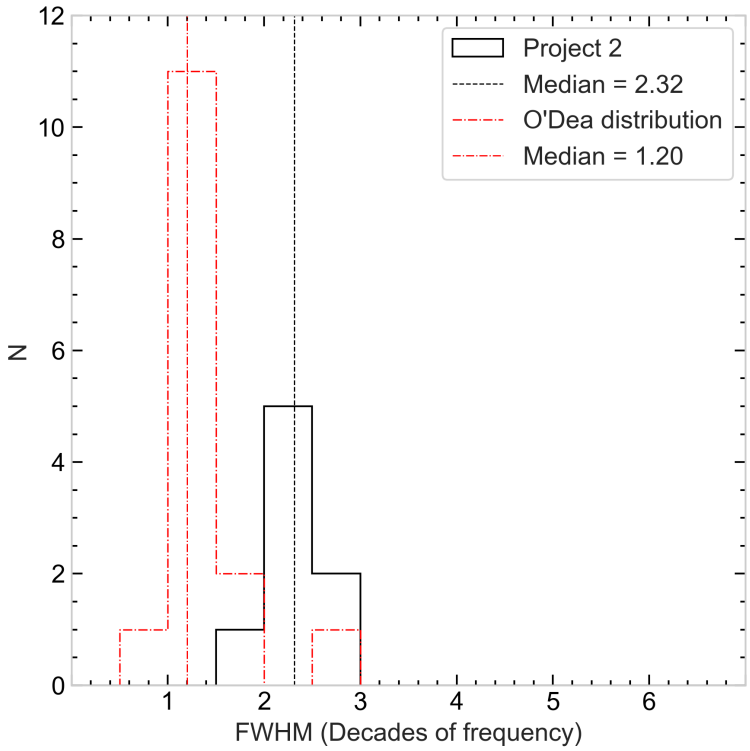

Figure 6.7: Histogram derived by the log-parabola fit for the eight slightly convex sources of Project 2, showing a median of 2.32. the dashed red histogram is the distribution of 15 GPS of O'Dea et al. (1991) with a median of 1.20.

6.5 The extended jet emission

Despite their compactness, the presence of components beyond the nuclear one is supported not only by morphological radio observations, but also by analysing the spectral emission. In fact, these radio-galaxies are still RL-AGN, and the resolved extended emission originates predominantly from optically thin synchrotron radiation, associated with their jets. The spectral analysis regarding the extended emission of the five sources of Project 1 (Table 5.5) provides therefore a powerful tool to investigate the radiative age of the plasma. The aim is to determine whether the emission is:

- *Steep* ($0.5 < \alpha \lesssim 1$), suggesting that it is not significantly aged emission, but instead reflects ongoing or recent jet activity that lacks the power to develop large-scale FR I or FR II morphologies.
- *Ultra-steep* ($\alpha \gtrsim 1$), indicative of radiatively old plasma. Such steep slopes are consistent with aged electron populations and may trace remnant emission from previous episodes of jet activity.

The spectral index of the extended emission has been derived using flux measurements between the 0.145 GHz LOFAR map and the 3.0 GHz S-band of the VLA, while all the other possible cases were prevented due to a substantial difference in resolution between maps. The spectral index relative to three sources of Project 1— `J0807+14`, `J0916+17`, `J1044+43`—spans in the interval $0.65 \leq \alpha \leq 0.83$, which qualifies them as steep-spectrum. In the VLA observations, the total flux density of these three sources decreases by approximately 25–85% compared to LOFAR. This drop reflects the loss of extended emission visible at 0.145 GHz, which is largely absent at 3.0 GHz. The radio structures detected at higher frequency span about 15–60 kpc, corresponding to a factor of 1.3 to 3.8 smaller than their linear size in the LOFAR maps.

The other two sources of Project 1, namely `J0910+18` and `J1722+30`, have extended emission characterized by a spectral index of 1.22 and 1.13, respectively. These spectral slopes may be considered ultra-steep here. Notably, these two sources appeared unresolved in the VLA observations, and so the flux density of the extended emission was estimated via upper limit (see Section 5.1), making the resulting spectral indices lower limits. In conclusion, only two sources of the five FR 0s in Project 1 show possibly evidence of an ageing activity from a previous ejection. A more statistically robust picture is still needed with a larger and complete sample of jetted FR 0s.

We extended our investigation into why some sources exhibit kiloparsec-scale emission while others do not, by searching for trends that might distinguish these two categories. As previously mentioned, Spearman and Pearson correlation analyses revealed no significant relationships across a range of parameters—including radio, host, and black hole properties—indicating that we currently lack sufficient information to properly address this issue.

Lastly, the high-frequency VLA observations offer sufficient resolution to isolate, in some cases, the core emission from the extended structure, allowing for the study of jet-sidedness and the derivation of jet bulk Lorentz factor Γ_{bulk}. To estimate the fraction of jetted FR0s, Capetti et al. (2020a) compared LOFAR, VLA, and VLBI data, focusing on sources whose spectral slopes indicate the dominance of an optically thin component

($\alpha > 0.5$). They inferred a lower limit of $\gtrsim 40\%$ for the fraction of jetted FR0s, a value that we find consistent with the LOFAR observations of Project 2; in comparison, the VLA C-band has approximately 65% of the extended sources that present a double-jet morphology at 4.5–7.5 GHz.

The study of jet-sidedness, when combined with other diagnostic plots related to accretion and ejection mechanisms (Figure 6.2) provides further insight into the nature of FR 0 jets. It also lays the groundwork for understanding how these jets interact with the surrounding medium, an essential aspect to quantify the feedback they may exert on the host galaxy.

From Table 5.2 we inferred an average jet-ratio of $\sim$ 1.45, for the six sources of Project 2 that allowed a calculation. This result is very similar to the $\sim$ 1.43 of Baldi et al. (2019a), except for our largest value of $\sim$ 2.61 found for `J0807+14` at 1.5 GHz, due to a very weak western jet that fades away at higher frequencies, as highlighted before. The lower resolution (6″) LOFAR maps, although less reliable when it comes to isolating the core component in compact sources such as FR 0s, reveal an average jet-ratio—inferred from eight sources—of $\sim$ 1.34, while Project 1 has just one source at 1.23.

To estimate the jet bulk Lorentz factor (Γ) from the observed jet-to-counterjet sidedness ratio (R), we adopt the standard Doppler boosting formalism for continuous jets assuming a randomly oriented sample of misaligned FR 0s. In this case, the observed flux density is enhanced according to

$$R = \left(\frac{1 + \beta \cos\theta}{1 - \beta \cos\theta} \right)^{p},$$

where $\beta = v/c$ is the intrinsic jet speed in units of the speed of light, θ is the angle between the jet and the line of sight, and $p = 2 + \alpha$ for continuous jets with spectral index α. This expression links the observed asymmetry in jet brightness to both the speed of the jet and the viewing geometry. Solving explicitly for β yields

$$\beta \cos\theta = \frac{R^{1/p} - 1}{R^{1/p} + 1},$$

but due to the coupling between β and Γ (via $\beta = \sqrt{1 - 1/\Gamma^2}$), the equation needs a numerical approach to be solved. However, as a representative example, we fixed a viewing angle of $\theta = 50°$, and considered a typical spectral index $\alpha = 0.6$. This simple approximation allowed us to constrain an upper limit for the jet bulk motion with reasonable assumptions. When we try to reproduce the jet-sidedness of $R \sim 1.5$, it results in $\Gamma_{bulk} \sim 1.01$ and $\beta \sim 0.14$ at kpc scale.

Although this result relies on several simplifications, the observed values of Γ_{bulk} in FR 0s consistently points to a mildly relativistic jet, rather than a fully relativistic one. On parsec scales as well, FR 0s predominantly exhibit mildly relativistic jets, with only about one-third showing $\Gamma_{\rm bulk} > 2$ (Giovannini et al., 2023). This further distinguishes them from FR Is, which typically launch relativistic jets with $\Gamma_{\rm bulk} > 3$ on parsec scales, before decelerating to sub-relativistic speeds at kiloparsec scales (Laing and Bridle, 2014). The potential causes underlying this behaviour, as well as its implications for the host galaxy, will be addressed in the final chapter.

7

Summary and Conclusions

A key process in the co-evolution of galaxies and their central supermassive black holes is the thermodynamic balance between the matter falling into the black hole (accretion) and the energy or material it releases back into its surroundings (feedback). The accretion–ejection mechanism powered by SMBHs is a key driver in galaxy evolution, injecting energy and momentum into the surrounding environment. However, the details of this process, especially in low luminosity sources—which are the most abundant in the Universe—remain poorly understood. Numerical simulations suggest that low-luminosity RGs predominantly channel their accretion power into compact galaxy-scale ($\lesssim$10-20 kpc) jets (Baldi, 2023). These jets, despite their lower power, may more efficiently couple with the interstellar medium and regulate star formation compared to powerful jets, which deposit much of their energy in the intergalactic medium.

Yet, our understanding of jet physics and the AGN–host galaxy connection at low luminosities is still limited, hindering a complete picture of the accretion-ejection paradigm and its feedback on galaxy evolution. Cross-matching high-sensitivity radio and optical surveys has revealed that the majority ($\sim$80%) of local RGs appear unresolved at arcsecond scales, highlighting the emergence of a distinct population of low-luminosity sources known as `FR 0s`. These objects are characterised by the absence of extended radio structures on kiloparsec scales; however, in some cases show evidence of mildly relativistic parsec-scale jets.

In this study, we conducted a multi-frequency radio analysis of a sub-sample of 32 FR 0 galaxies selected from the FR0CAT catalogue (Baldi et al., 2018). The main aim was to investigate their compactness and search for possible extended emission, in order to shed light on the physical nature of FR 0s. Specifically, to understand why these sources fail to develop large-scale radio jets like FR Is, despite sharing similar global host and nuclear properties. In particular, we analysed two groups of sources:

- The first group (Project 1) includes five sources selected by Capetti et al. (2020a) based on the presence of large-scale emission—from a few tens of kpc to $\gtrsim$ 140 kpc—in LOFAR images at 0.144 GHz. For these sources we analysed new dedicated VLA observations at 3.0 GHz to investigate the spectral index and infer the origin of this emission.

- The second group (Project 2) comprises 27 sources selected from the FR0CAT catalogue and focuses on investigating the nuclear (core) emission of FR 0 radio

galaxies. This is achieved through high-resolution VLA observations at 1.4, 4.5, and 7.5 GHz, which are capable of resolving the compact radio structures that appear unresolved in FIRST images and of detecting potential small-scale jets. This study builds upon and extends the preliminary characterization of FR 0 cores presented by Baldi et al. (2019a).

The VLA datasets at 1.5, 3.0, 4.5, and 7.5 GHz were reduced and complemented with archival public images from LoTSS (0.145 GHz), RACS (0.887 GHz), FIRST (1.4 GHz), and NVSS (1.4 GHz). This multi-frequency, multi-resolution approach enabled a comprehensive investigation of the morphological and spectral properties of the sample and led to the following main results:

1. The spectral index of the large scale emission of the five sources in the first group is in the range $0.65 < \alpha < 0.83$ for three sources and >1.1 for the other two sources between 0.145 and 3.0 GHz. This suggests that in the first three sources the observed outflows are still fuelled with freshly accelerated particles, while in the other two sources with $\alpha > 1.1$, the extended emission might instead be consistent with old plasma from a previous AGN outburst.

2. At subarcsec resolution (few hundreds parsec) the morphology of the 27 FR 0s analysed (Project 2) is mostly compact and core-dominated, with $\gtrsim 70\%$ of the total flux density originating from the core component. This strong core dominance is comparable to that of coreG sources, but significantly exceeds that observed in FR Is. Considering both Projects, the sources that display extended radio structures in the VLA observations never exceed ~ 50 kpc, and even when a relatively substantial resolved structure is present, the nuclear region dominates the radio output. Overall, linking the compactness of FR 0s to any specific property—whether radio, host, or black hole properties—has proven challenging. Our analysis found no evidence of a positive correlation in sources with extended emission, with respect to the unresolved ones. Further more, the presence of extended emission does not appear to be the result of a denser environment—more similar to that of FR Is—as they exhibit a analogous number of cosmological neighbours within a 2 Mpc radius as the unresolved sources.

3. When looking at high resolution, the spectral index of the cores are mostly flat ($\alpha < 0.5$) , as expected from nuclear emission produced by self-absorbed compact components. In fact, only five spectral index are steep ($\alpha > 0.5$) between 0.145-1.5 GHz, while eleven in the range 1.5-4.5 and 4.5-7.5 GHz. Additionally, at 7.5 GHz, four of these steep-spectrum sources have $\alpha > 1.0$ (including the uncertainties), which is indicative of an an optically thin component on scales within the beam, consistent with the presence of jets.

4. The broad-band (0.145-7.5 GHz) radio SEDs show eight objects with slightly convex spectra. The SEDs of these sources were fitted using a log-parabolic model, following the method described by O'Dea et al. (1991), to assess whether these sources could be interpreted as young radio galaxies: that is, sources that abruptly transition from the optically thick component at low frequencies to the optically thin component at high frequencies, resulting a convex spectrum that peaks in the GHz frequencies.No young sources are identified with this method, consistently with the results by Capetti, A. et al. (2019), confirming that the youth of the radio

source is not the major reason for the compact emission. However, it is possible that a small fraction is still a genuinely young RG, and the results leave open the possibility that approximately 10–15% of FR 0s may belong to the class of GPS sources, or at least exhibit spectral features consistent with that population.

5. We used the optical-band [O III] line luminosity, an isotropic proxy of the bolometric AGN power, to investigate the characteristics of jets in their early stages, proximal to the central engine. We examined the relationship between the radio core luminosity and the [O III] emission line across a continuous distribution of RL-AGN, including coreG and FR I sources. Our results confirm previous findings by Baldi et al. (2018) and Baldi et al. (2019a), demonstrating that the jet properties of FR 0s are consistent with the low-luminosity tail of the FR I population. Furthermore, by utilizing jet-sidedness measurements, we constrained an upper limit on the bulk Lorentz factor of the jet ($\Gamma_{\rm bulk} \sim 1.01$), reinforcing the scenario of a sub-relativistic jet velocity at kiloparsec scales.

As mentioned in Section 1.3.1, two main scenarios are typically invoked to explain the observed properties of FR 0s: the lack of extended emission and the presence of low-power, core-dominated jets. These characteristics can be interpreted within both non-evolutionary and evolutionary frameworks (Baldi, 2023).
In the non-evolutionary (static) scenario, intrinsic physical conditions, such as low prograde black hole spin (Garofalo et al., 2010), modest magnetic flux, or specific jet composition, are thought to act together to produce sub-relativistic, poorly collimated jets that fail to propagate beyond the host galaxy (Grandi et al., 2021). In contrast, evolutionary (dynamic) models suggest that FR 0s represent a transient or recurrent phase of radio-loud AGN activity. In this view, short-lived or intermittent jet episodes, driven by low or unstable accretion rates, prevent the development of large-scale radio structures (O'Dea and Saikia, 2021). Both scenarios are broadly consistent with current observations and our results, with the former favoured over the latter, and may co-exist, reflecting a diversity of jet-launching histories and feedback mechanisms across the FR 0 population.

7.1 Future work

To further validate and expand on the findings presented in this thesis, various follow-up observations can be undertaken. A priority would be to observe the remaining 59 FR 0s from the FR0CAT catalogue using the VLA in its A configuration. This would extend the analysis of kiloparsec-scale properties to the entire sample of 104 sources, enabling more robust statistical studies of their radio morphologies and spectral properties. A complete dataset would also allow for a more accurate assessment of their number density relative to other classes of radio galaxies, and provide deeper insight into the potential role of FR 0s in AGN mechanical feedback and host galaxy evolution. In this context, complementary X-ray observations would be highly valuable. Probing the keV energy regime could reveal whether the resolved extended radio structures in FR 0s produce significant large-scale effects, such as the X-ray cavities reported by Ubertosi et al. (2021), thus confirming their ability to inject energy into the surrounding medium. However, given that AGNs emit across the entire electromagnetic spectrum, a multi-wavelength

investigation of the FR0CAT sample would likely provide significant information at any chosen wavelength. For example, some FR 0s have been confirmed as gamma-ray emitters and may contribute to the population of low-power multi-messenger sources, offering valuable insights into particle acceleration mechanisms at low energies.

In terms of morphology, employing high-resolution VLBI (e.g. eMERLIN, EVN, VLBA) observations to obtain parsec-scale images, would be a valuable opportunity to better constrain the composition, velocity distribution and asymmetry of FR 0 jets, particularly in those sources that still exhibit mildly relativistic outflows on small scales (Baldi et al., 2024). Since most FR 0s lack extended jet structures at kiloparsec scales—or display only weak, short-lived jets that fail to propagate beyond a few kiloparsecs—it would be particularly insightful to quantify the fraction of sources that retain detectable jets when observed with the VLA, and to investigate the physical mechanisms responsible for the observed discrepancy between parsec- and kiloparsec-scale jet morphologies. Expanding the number of FR 0s observed with VLBI, or other multi-epoch campaigns, could also help resolve ongoing uncertainties regarding the variability and duty cycle of these compact radio galaxies.

Finally, to address the persistent issue of misclassification, combining radio observations across a broader MHz–GHz range is essential to constrain the spectral shapes of FR 0s, assess the presence of optically thin extended emission, and identify potential young radio sources that may be misclassified as FR 0s.

Acronyms and Abbreviations A

AGN	Active Galactic Nuclei
ASKAP	Australian Square Kilometre Array Pathfinder
BBP	Big Blue Bump
BLR	Broad Line Region
BLRG	Broad Line Radio Galaxy
BP	Blandford–Payne
BPA	Beam Position Angle
BZ	Blandford–Znajek
CMB	Cosmic Microwave Background
CSS	Compact Steep Spectrum
CRS	Compact Radio Source
DB	Dirty Beam
DM	Dirty Map
DR	Dynamic Range
ETG	Early Type Galaxy
EVLA	Expanded Very Large Array
EM	Electro-Magnetic
EW	Equivalent Width
FIR	Far Infra Red
FIRST	Faint Images of the Radio Sky at Twenty-Centimeters
FR	Fanaroff–Riley
FR	Fanaroff–Riley
FSRQ	Flat Spectrum Radio Quasars
FWHM	Full Width at Half Maximum
GPS	Gigahertz-Peaked Spectrum
HE(R)G	High Excitation (Radio) Galaxies
ISCO	Innermost Circular Stable Orbit
ISM	Interstellar Medium
JWST	James Webb Space Telescope
JVLA	Jansky Very Large Array

LAS	Largest Angular Scale
LE(R)G	Low Excitation (Radio) Galaxies
LLS	Largest Linear Size
LOFAR	LOw Frequency ARray
LOS	Line of Sight
LTG	Late Type Galaxy
MIR	Mid Infra Red
NIR	Near Infra Red
NLR	Narrow Line Region
NVSS	NRAO VLA Sky Survey
QSO	Quasi Stellar Object
RACS	Rapid Askap Continuum Survey
RFI	Radio Frequency Interference
RG	Radio Galaxy
RIAF	Radiatively Inefficient Accretion Flow
RL	Radio Loud
RMS	Root Mean Square
RQ	Radio Quiet
SDSS	Sloan Digital Sky Survey
SED	Spectral Energy Distribution
SMBH	Super Massive Black Hole
SpW	Spectral Window
SSA	Synchrotron Self-Absorption
SSRQ	Steep Spectrum Radio Quasar
UM	Unified Model
VLA	Very Large Array
VLBI	Very Large Baseline Interferometer
VLTI	Very Large Telescope Interferometer

B

Additional optical maps

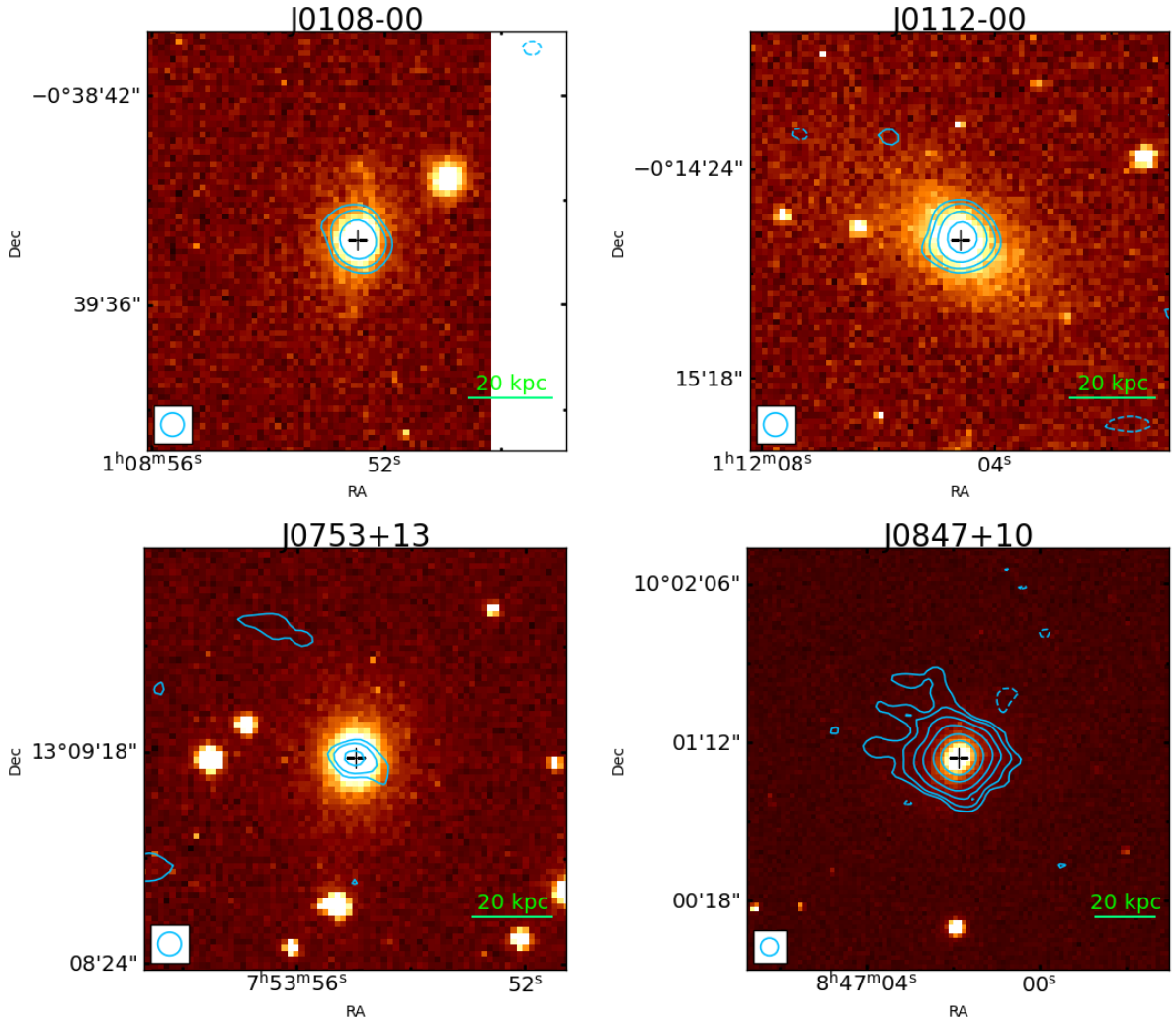

Figure B.1: Selection of SDSS optical images of the host galaxies associated with the 27 FR 0s of Project 2, overlaid with LOFAR radio contours at 0.145 GHz.The LOFAR beam of $6'' \times 6''$, is shown in the bottom-left corner of each panel, while the black cross marks the coordinate centre of the host galaxy. The contour levels and the local rms are displayed at the end of the selection, in Table B.1. A total of 26 out of 27 images are displayed, as `J0807+14` is shared between both projects and is therefore shown only once in Figure 2.2. In some cases, the optical maps do not fully cover the field of view, resulting in regions where only the white radio background is displayed. Continued on next page.

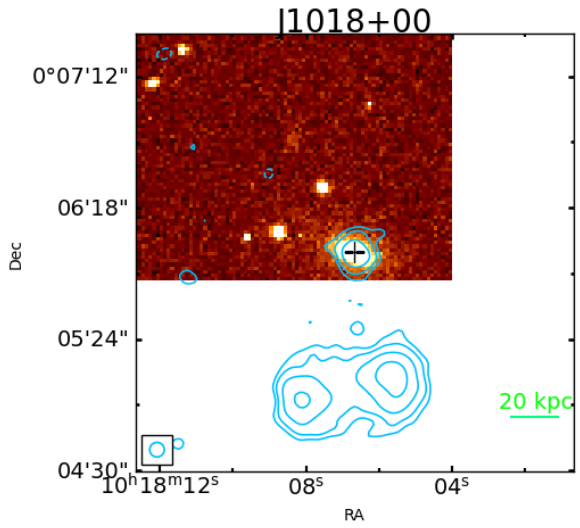
J1018+00
0°07'12"
06'18"
05'24"
04'30"
Dec
10h18m12s
08s
04s
RA
20 kpc

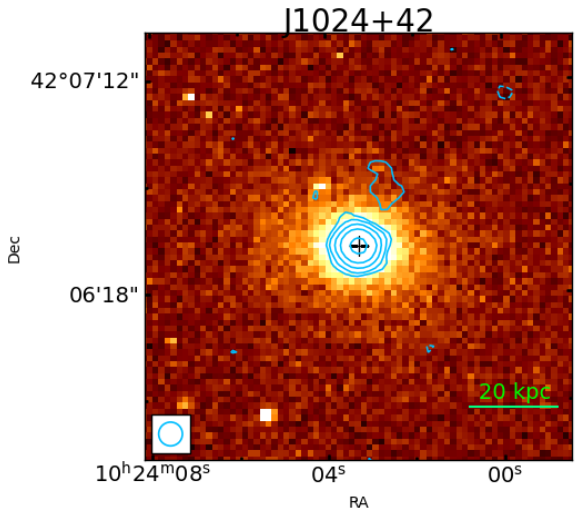
J1024+42
42°07'12"
06'18"
Dec
10h24m08s
04s
00s
RA
20 kpc

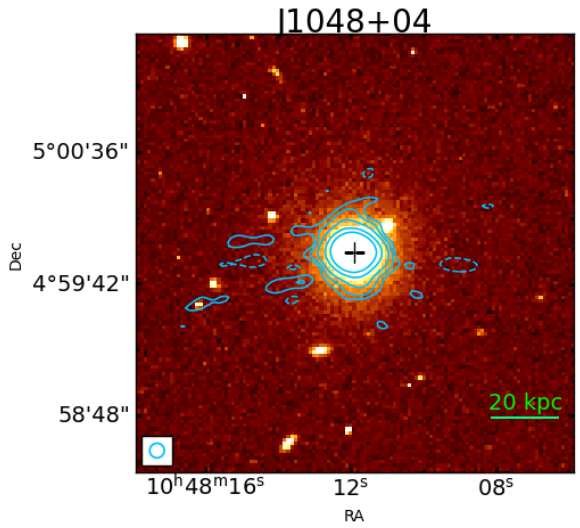
J1048+04
5°00'36"
4°59'42"
58'48"
Dec
10h48m16s
12s
08s
RA
20 kpc

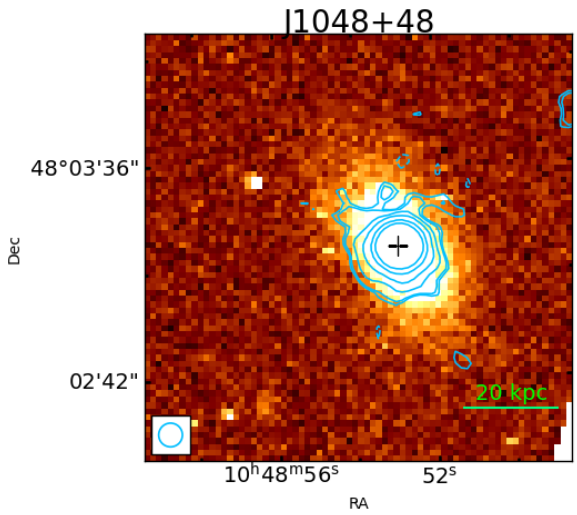
J1048+48
48°03'36"
02'42"
Dec
10h48m56s
52s
RA
20 kpc

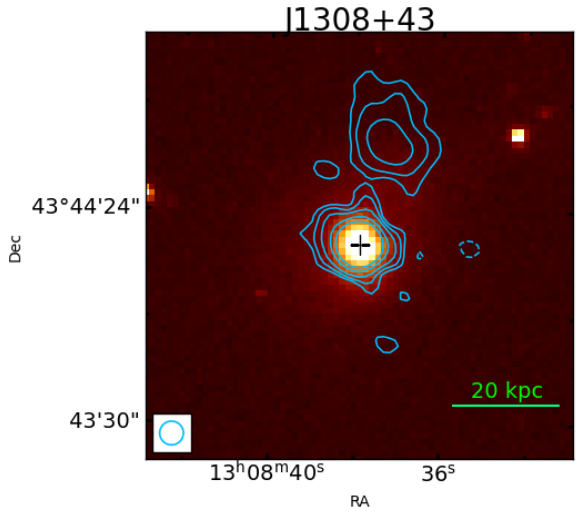
J1308+43
43°44'24"
43'30"
Dec
13h08m40s
36s
RA
20 kpc

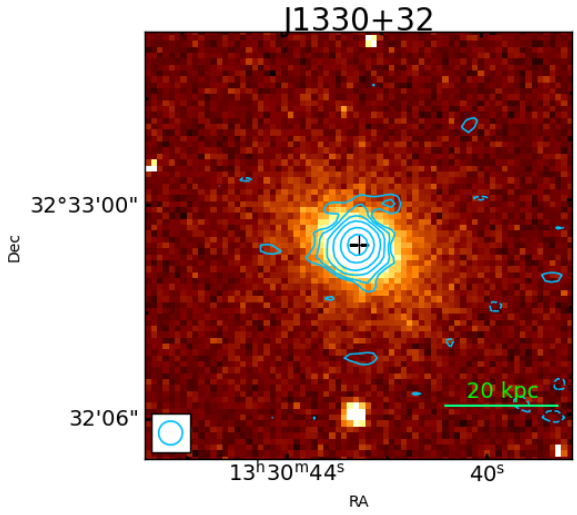
J1330+32
32°33'00"
32'06"
Dec
13h30m44s
40s
RA
20 kpc

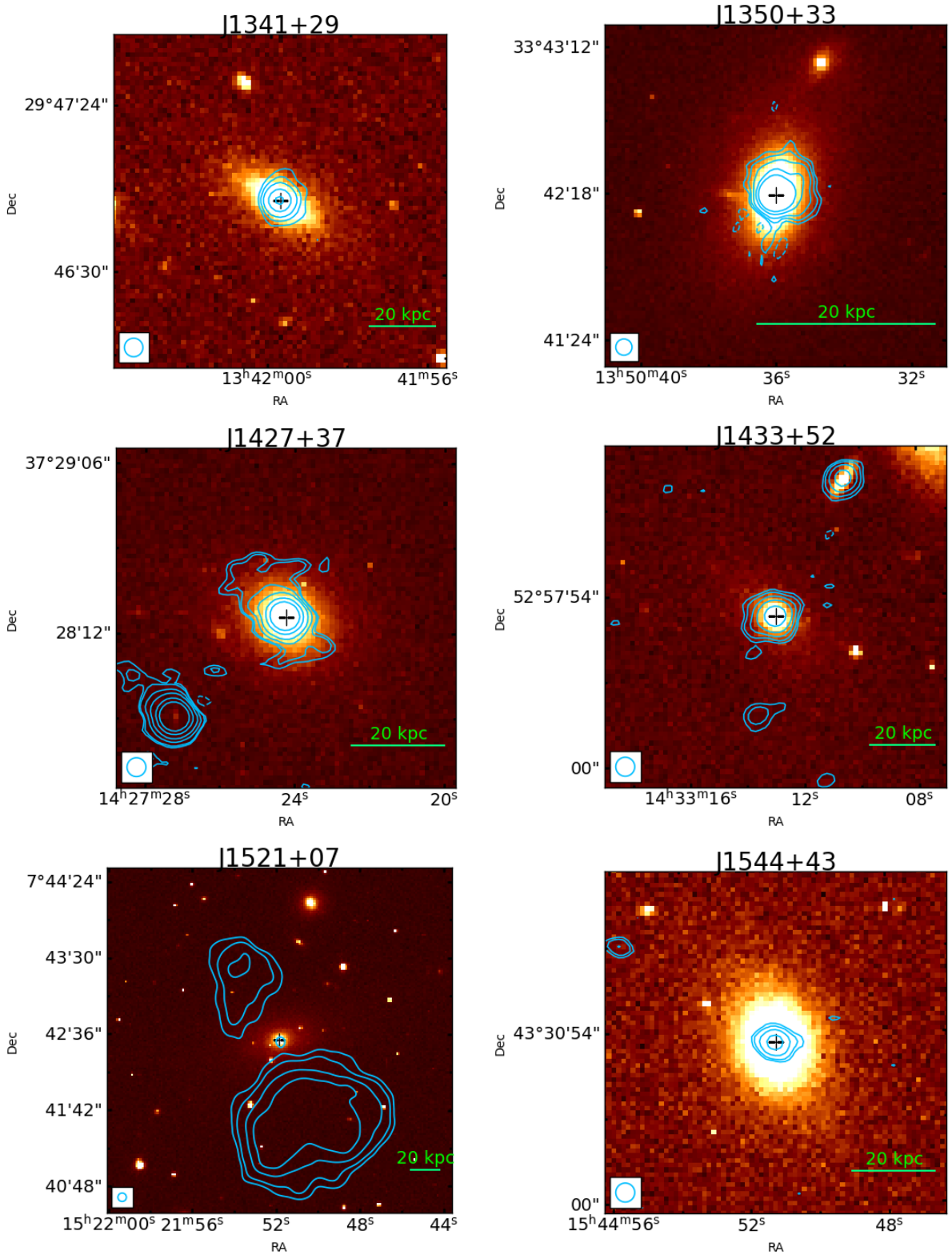
J1341+29
29°47'24"
46'30"
Dec
20 kpc
13h42m00s
41m56s
RA
J1350+33
33°43'12"
42'18"
41'24"
Dec
20 kpc
13h50m40s
36s
32s
RA
J1427+37
37°29'06"
28'12"
Dec
20 kpc
14h27m28s
24s
20s
RA
J1433+52
52°57'54"
00"
Dec
20 kpc
14h33m16s
12s
08s
RA
J1521+07
7°44'24"
43'30"
42'36"
41'42"
40'48"
Dec
20 kpc
15h22m00s
21m56s
52s
48s
44s
RA
J1544+43
43°30'54"
00"
Dec
20 kpc
15h44m56s
52s
48s
RA

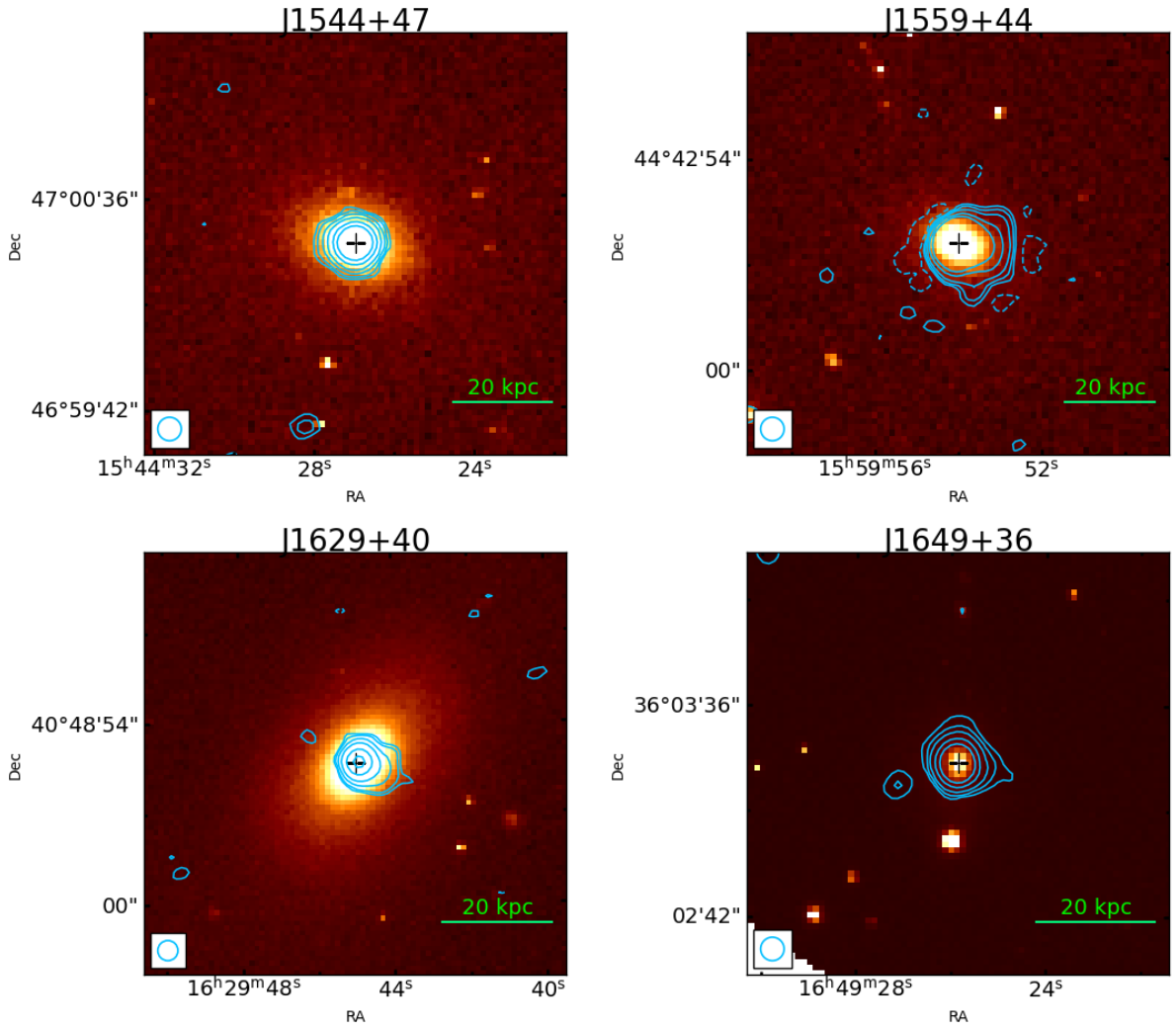

Name	RMS [mJy/beam]	Contours [×RMS]	Name	RMS [mJy/beam]	Contours [×RMS]
J0108–00	$23.4 \cdot 10^{-2}$	$-3, 3, 5, 10, 20, 50, 100$	J1341+29	$8.2 \cdot 10^{-2}$	$-5, 5, 10, 20, 50, 100$
J0112–00	$19.7 \cdot 10^{-2}$	$-3, 3, 5, 10, 20, 50, 100$	J1350+33	$25.0 \cdot 10^{-2}$	$-5, 5, 10, 20, 50, 100$
J0753+13	$9.6 \cdot 10^{-2}$	$-3, 3, 5, 10, 20, 50, 100$	J1427+37	$9.1 \cdot 10^{-2}$	$-4, 4, 5, 10, 20, 50, 100$
J0847+10	$12.6 \cdot 10^{-2}$	$-3, 3, 5, 10, 20, 50, 100$	J1433+52	$6.3 \cdot 10^{-2}$	$-3, 3, 5, 10, 20, 50, 100$
J1018+00	$22.8 \cdot 10^{-2}$	$-3, 3, 5, 10, 20, 50, 100$	J1521+07	$33.6 \cdot 10^{-2}$	$-50, 50, 100, 250, 500$
J1024+42	$6.1 \cdot 10^{-2}$	$-3, 3, 5, 10, 20, 50, 100$	J1544+43	$7.8 \cdot 10^{-2}$	$-3, 3, 5, 10, 20, 50, 100$
J1048+04	$17.5 \cdot 10^{-2}$	$-5, 5, 10, 20, 50, 100$	J1544+47	$7.6 \cdot 10^{-2}$	$-3, 3, 5, 10, 20, 50, 100$
J1048+48	$7.7 \cdot 10^{-2}$	$-4, 4, 5, 10, 20, 50, 100$	J1559+44	$7.8 \cdot 10^{-2}$	$-5, 5, 10, 20, 50, 100$
J1308+43	$11.8 \cdot 10^{-2}$	$-5, 5, 10, 20, 50, 100$	J1629+40	$7.7 \cdot 10^{-2}$	$-3, 3, 5, 10, 20, 50, 100$
J1330+32	$9.2 \cdot 10^{-2}$	$-3, 3, 5, 10, 20, 50, 100$	J1649+36	$8.3 \cdot 10^{-2}$	$-5, 5, 10, 20, 50, 100$

Table B.1: Imaging radio parameters for 20 FR 0s of Project 2. Column description: (1) source name; (2) RMS noise in the 0.145-GHz LOFAR map; (3) LOFAR radio contours superimposed on the optical maps of Figure B.1.

Additional radio maps

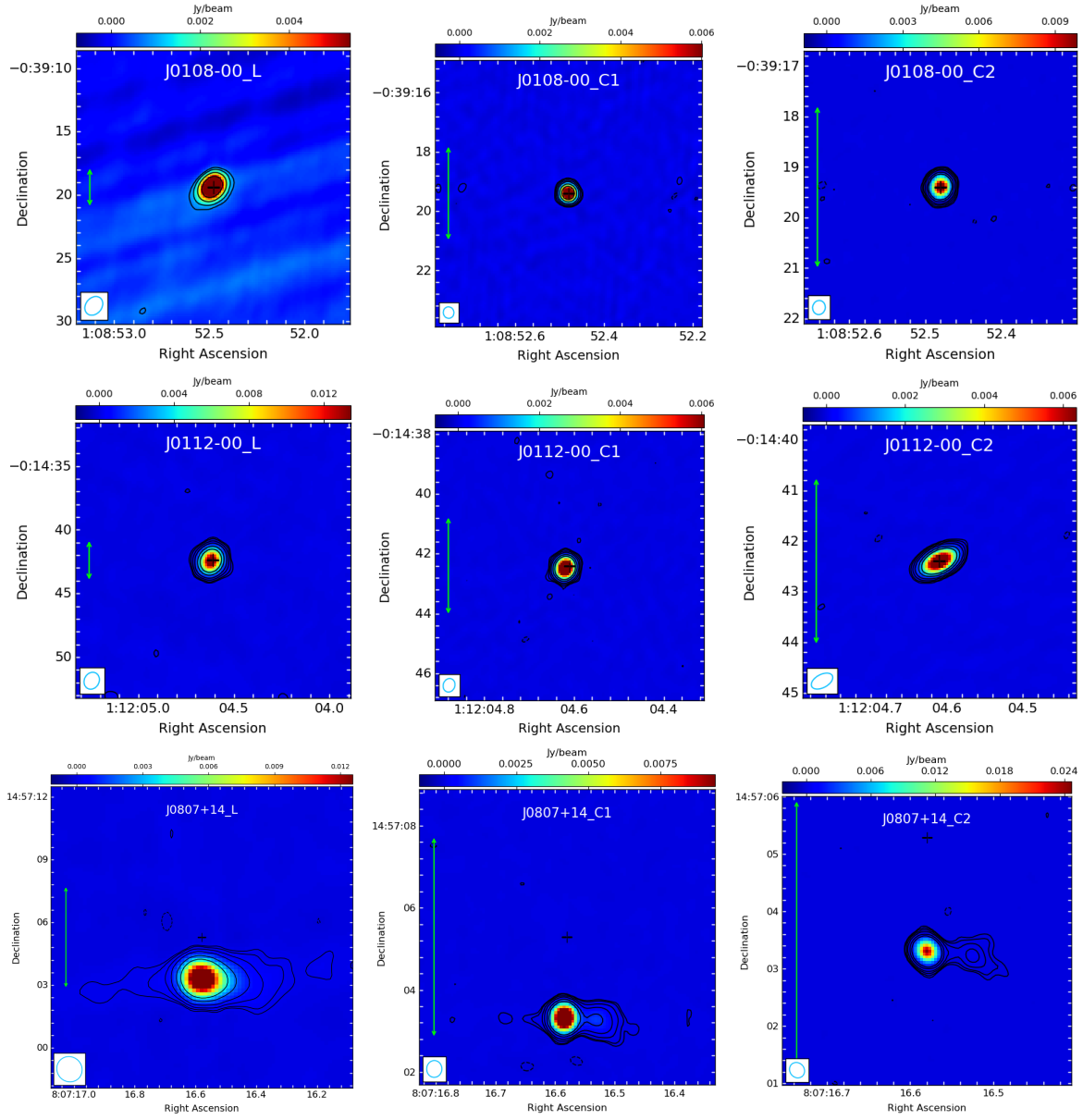

Figure C.1: Selection of VLA radio maps of Project 2 sources after self-calibration, imaged using Briggs weighting (robust = 0.5). The maps are obtained at 1.5 GHz (L-band), 4.5 GHz (C1-band), and 7.5 GHz (C2-band). The remaining images are shown in Figure 4.9, while the local rms and contour levels are listed in Table 4.3. The green arrow indicates a symbolic scale of 3 kpc, the beam is shown in the bottom-left corner, and the black cross marks the radio coordinate centre of each FR 0s. Continued on next page.

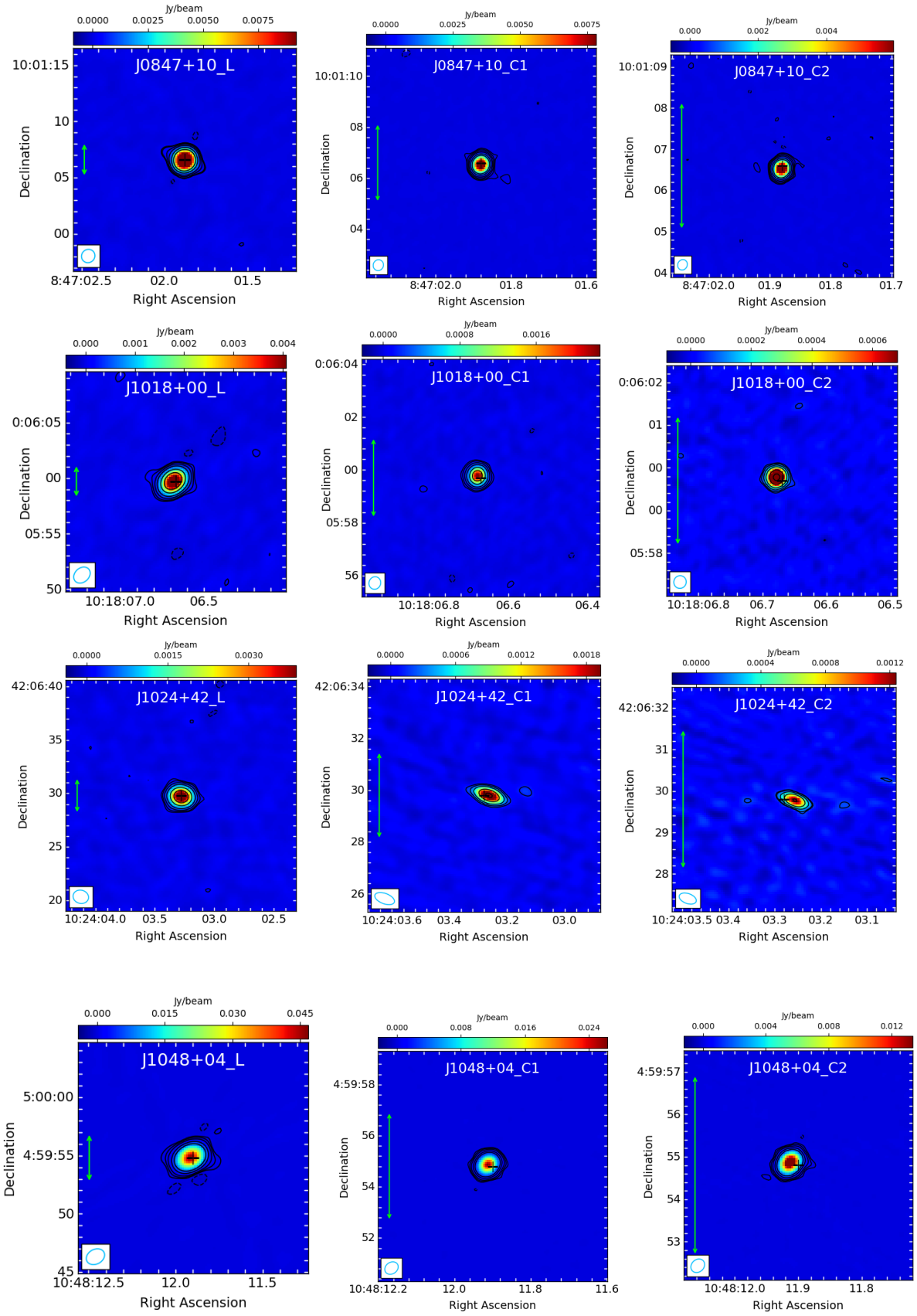
J0847+10_L
J0847+10_C1
J0847+10_C2
J1018+00_L
J1018+00_C1
J1018+00_C2
J1024+42_L
J1024+42_C1
J1024+42_C2
J1048+04_L
J1048+04_C1
J1048+04_C2
Jy/beam
Declination
Right Ascension

Figure C.1

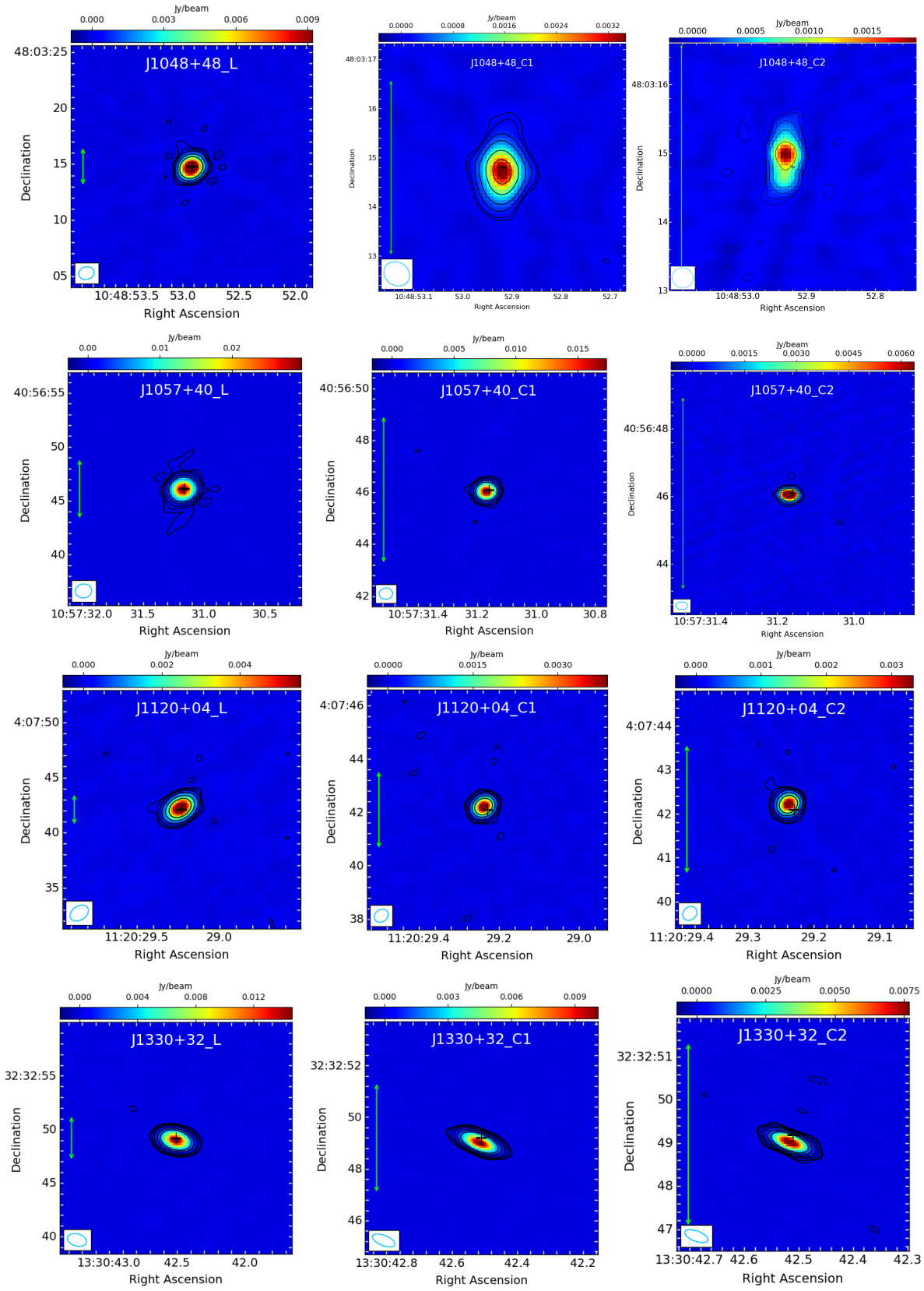
J1048+48_L
J1048+48_C1
J1048+48_C2
J1057+40_L
J1057+40_C1
J1057+40_C2
J1120+04_L
J1120+04_C1
J1120+04_C2
J1330+32_L
J1330+32_C1
J1330+32_C2
Jy/beam
Declination
Right Ascension

Figure C.1

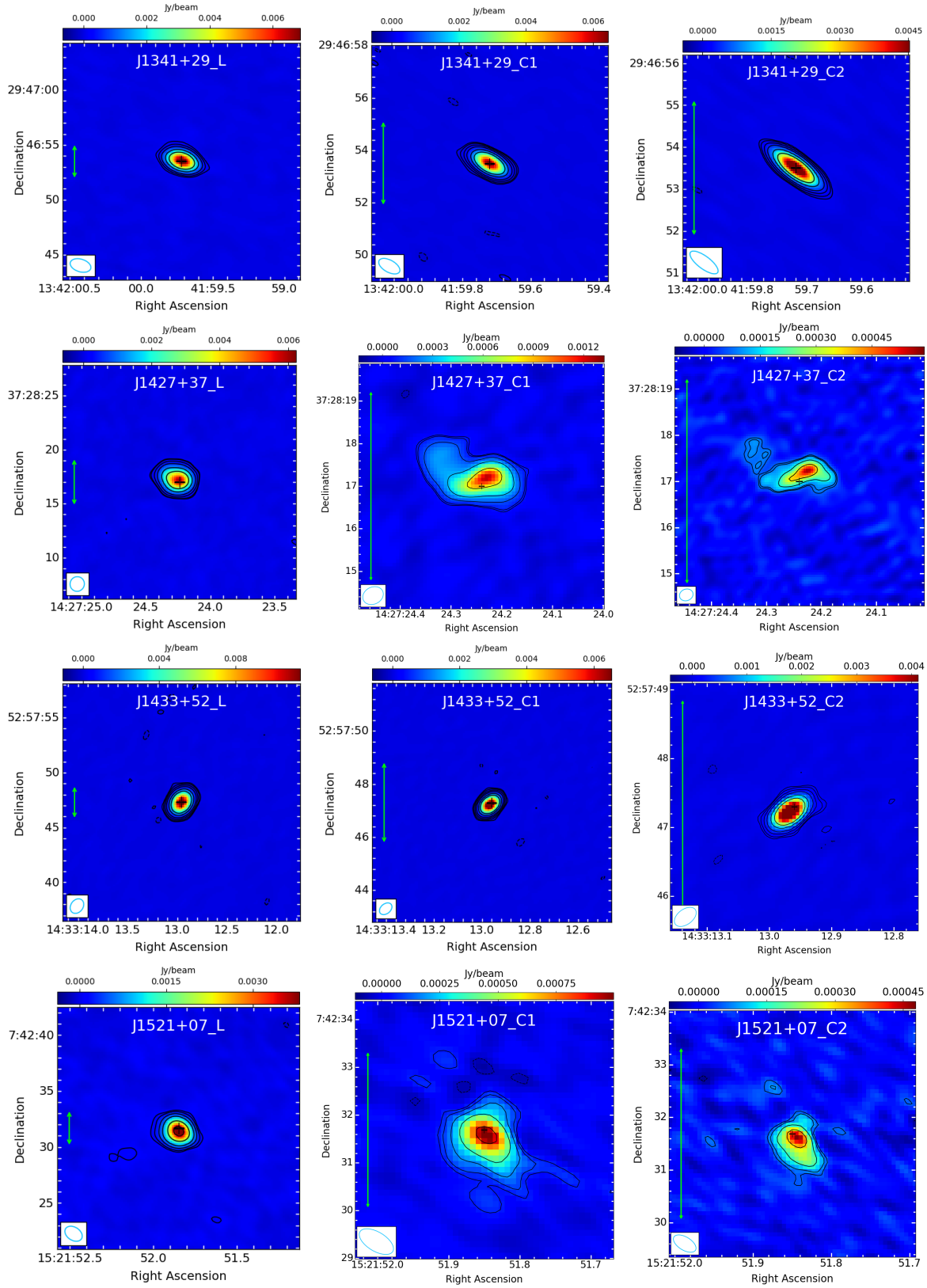
J1341+29_L
J1341+29_C1
J1341+29_C2
J1427+37_L
J1427+37_C1
J1427+37_C2
J1433+52_L
J1433+52_C1
J1433+52_C2
J1521+07_L
J1521+07_C1
J1521+07_C2
Jy/beam
Declination
Right Ascension

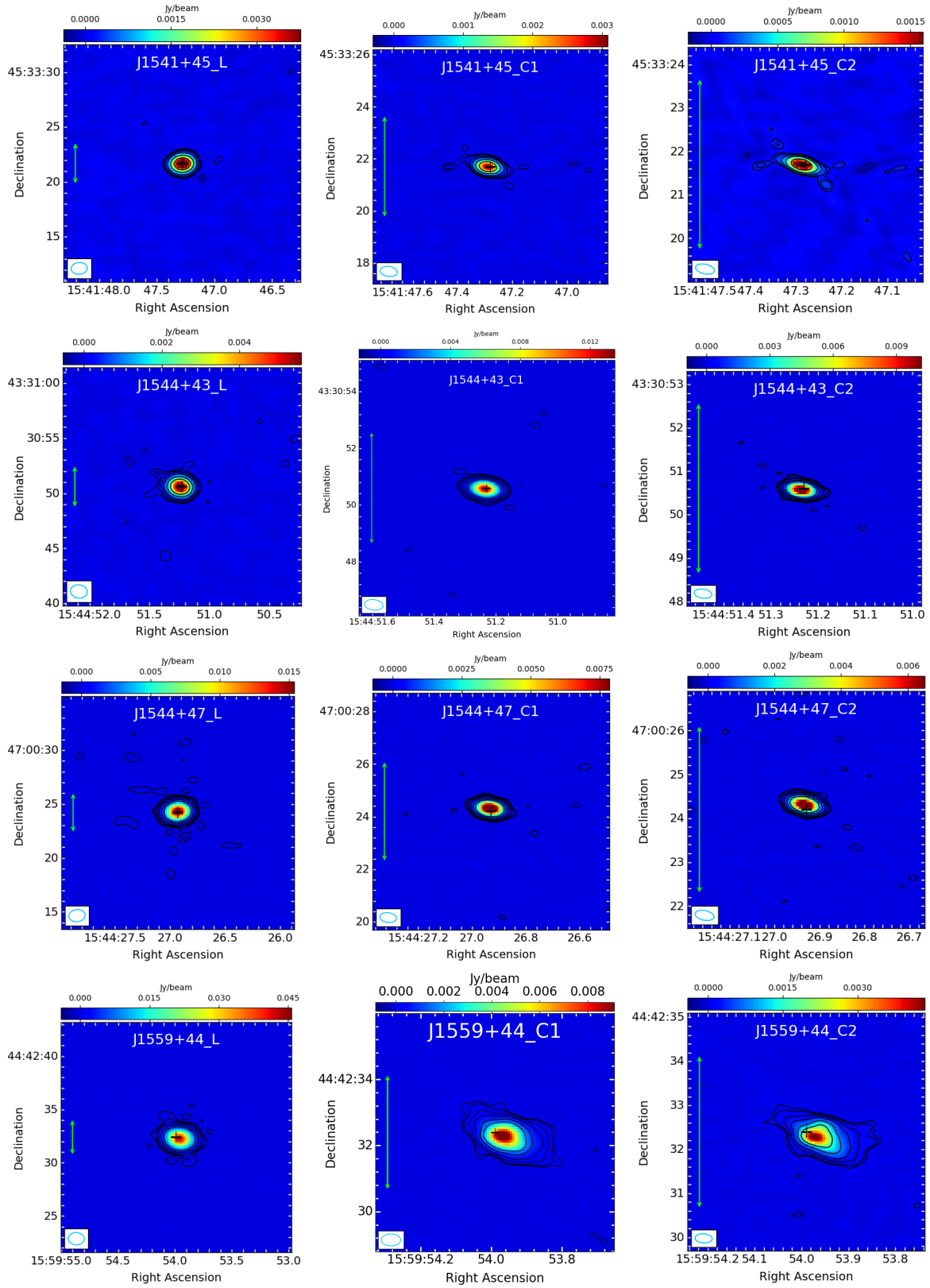
J1541+45_L
J1541+45_C1
J1541+45_C2
J1544+43_L
J1544+43_C1
J1544+43_C2
J1544+47_L
J1544+47_C1
J1544+47_C2
J1559+44_L
J1559+44_C1
J1559+44_C2
Jy/beam
Declination
Right Ascension

Figure C.1

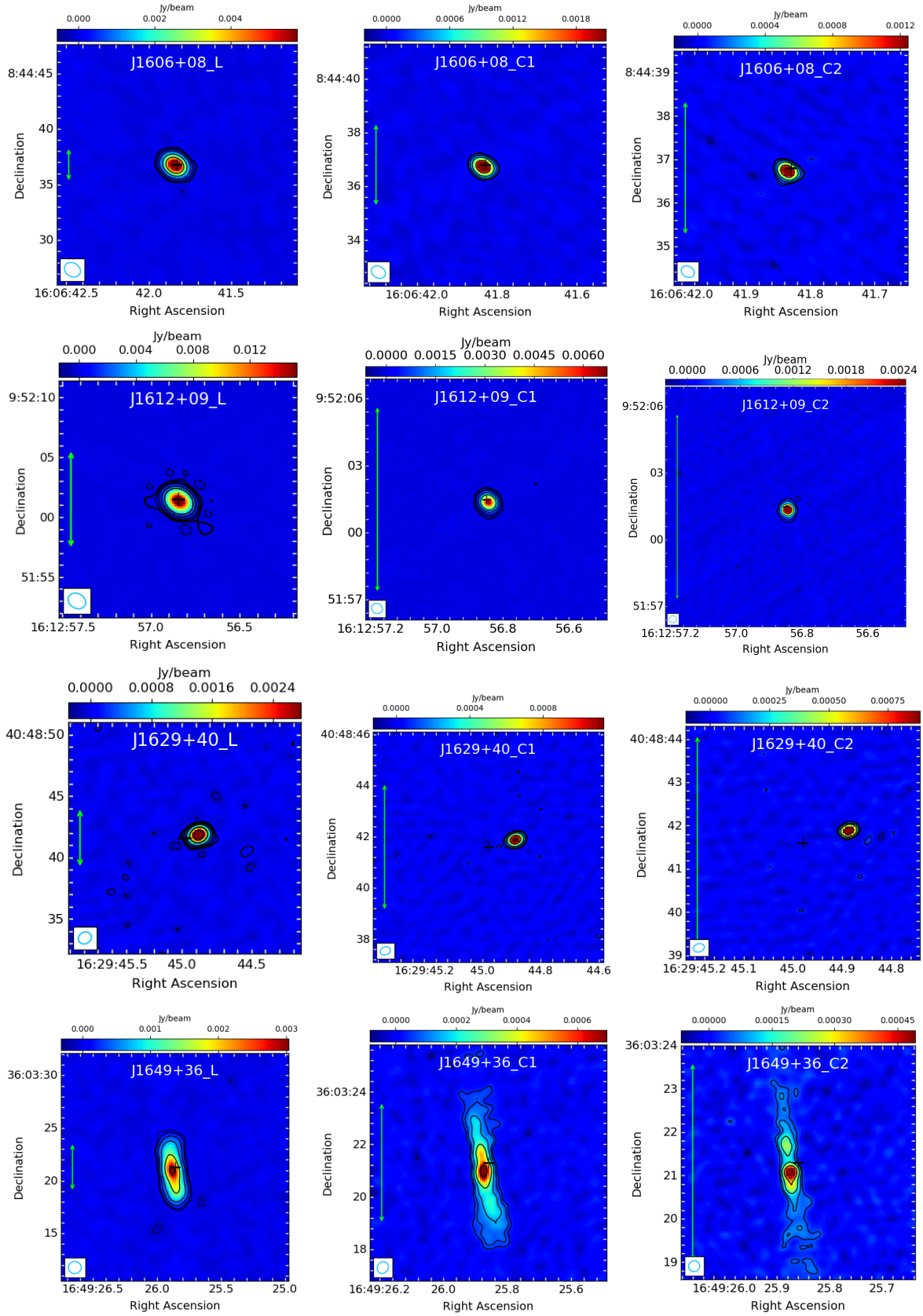
J1606+08_L
J1606+08_C1
J1606+08_C2
J1612+09_L
J1612+09_C1
J1612+09_C2
J1629+40_L
J1629+40_C1
J1629+40_C2
J1649+36_L
J1649+36_C1
J1649+36_C2
Jy/beam
Declination
Right Ascension

Figure C.1

D

Additional SED

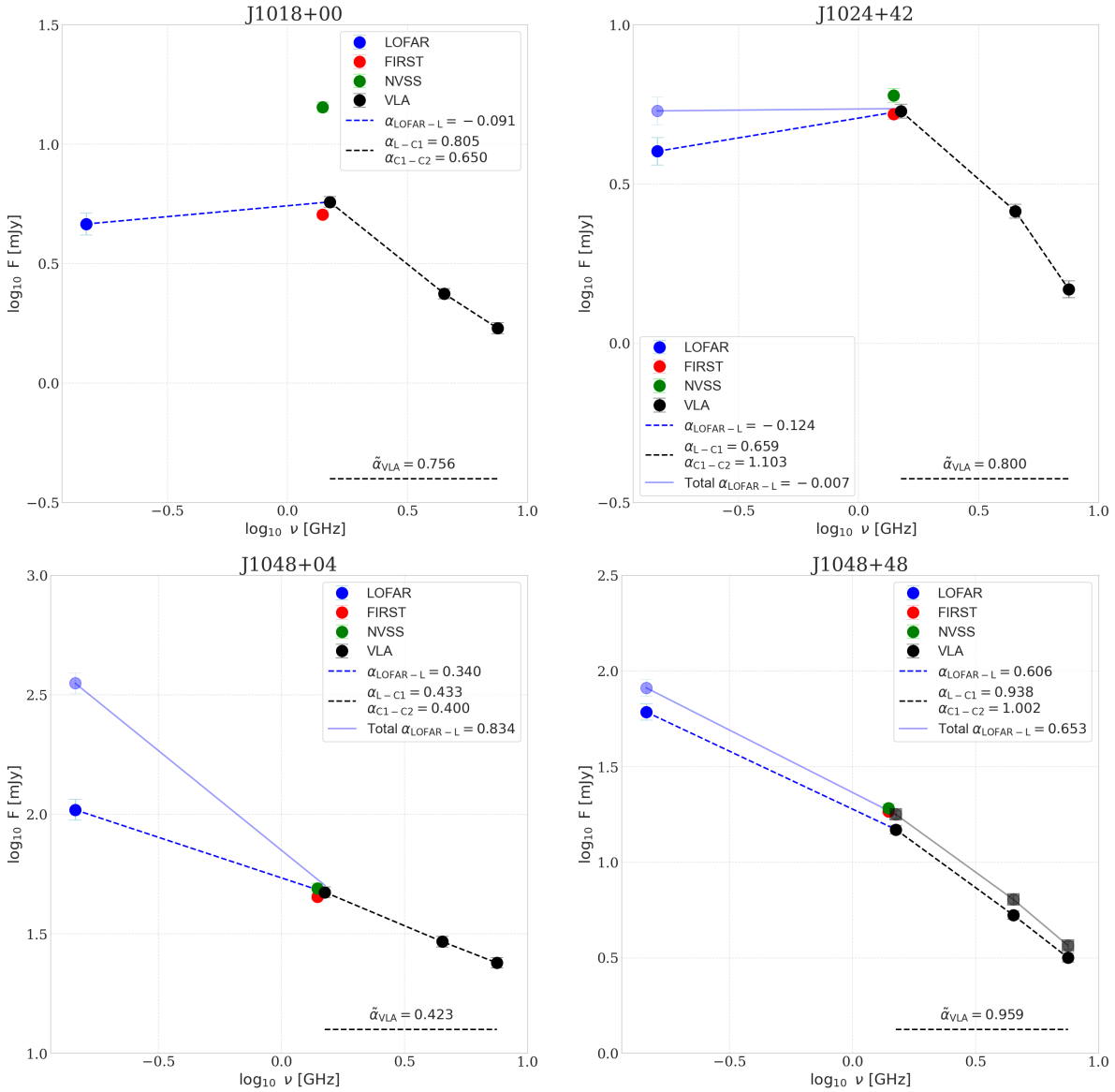

Figure D.1: Selection of the radio SED of the sources in project 2, the remaining images are shown in Figure 5.5. The dashed lines refers always to the nuclear (core) components, while the lighter continuous lines and points to the total components. The short dashed line in the bottom-right corner is the average core spectral index for the beam matched VLA maps, from 1.5 to 7.5 GHz.

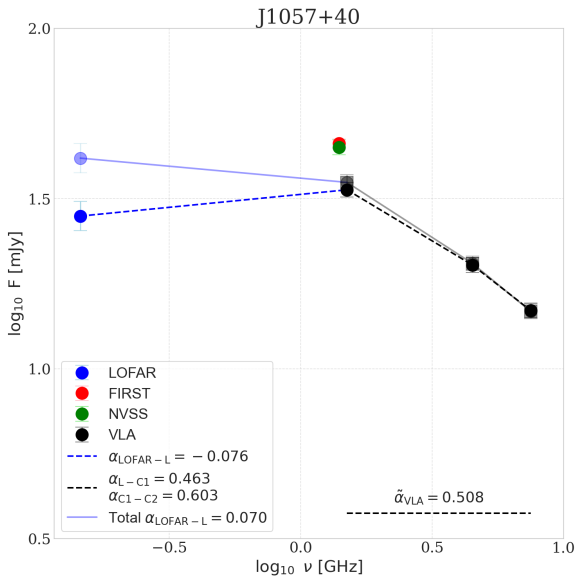
J1057+40
LOFAR
FIRST
NVSS
VLA
$\alpha_{\mathrm{LOFAR-L}} = -0.076$
$\alpha_{\mathrm{L-C1}} = 0.463$
$\alpha_{\mathrm{C1-C2}} = 0.603$
Total $\alpha_{\mathrm{LOFAR-L}} = 0.070$
$\tilde{\alpha}_{\mathrm{VLA}} = 0.508$
$\log_{10}$ F [mJy]
$\log_{10}$ ν [GHz]

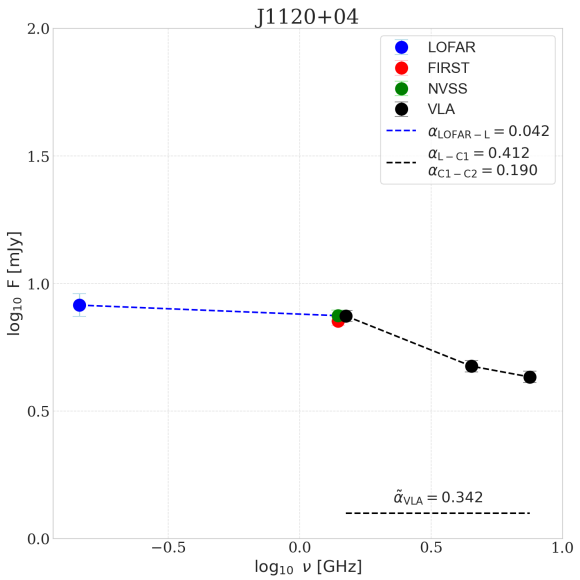
J1120+04
LOFAR
FIRST
NVSS
VLA
$\alpha_{\mathrm{LOFAR-L}} = 0.042$
$\alpha_{\mathrm{L-C1}} = 0.412$
$\alpha_{\mathrm{C1-C2}} = 0.190$
$\tilde{\alpha}_{\mathrm{VLA}} = 0.342$
$\log_{10}$ F [mJy]
$\log_{10}$ ν [GHz]

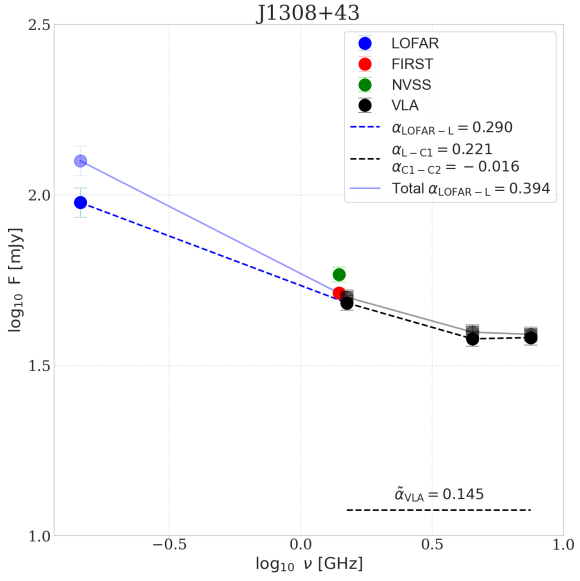
J1308+43
LOFAR
FIRST
NVSS
VLA
$\alpha_{\mathrm{LOFAR-L}} = 0.290$
$\alpha_{\mathrm{L-C1}} = 0.221$
$\alpha_{\mathrm{C1-C2}} = -0.016$
Total $\alpha_{\mathrm{LOFAR-L}} = 0.394$
$\tilde{\alpha}_{\mathrm{VLA}} = 0.145$
$\log_{10}$ F [mJy]
$\log_{10}$ ν [GHz]

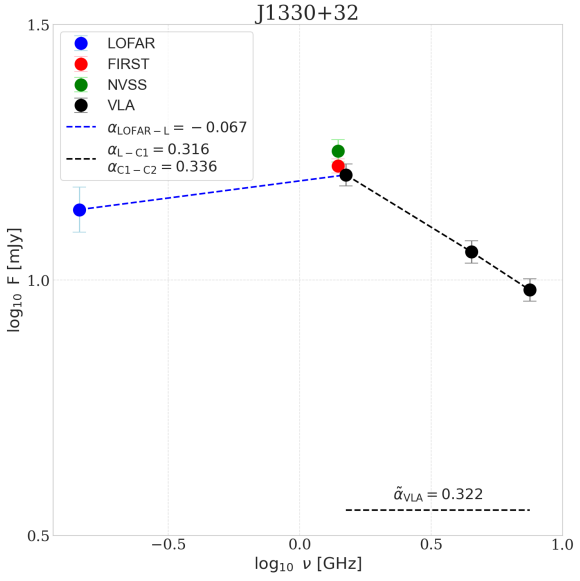
J1330+32
LOFAR
FIRST
NVSS
VLA
$\alpha_{\mathrm{LOFAR-L}} = -0.067$
$\alpha_{\mathrm{L-C1}} = 0.316$
$\alpha_{\mathrm{C1-C2}} = 0.336$
$\tilde{\alpha}_{\mathrm{VLA}} = 0.322$
$\log_{10}$ F [mJy]
$\log_{10}$ ν [GHz]

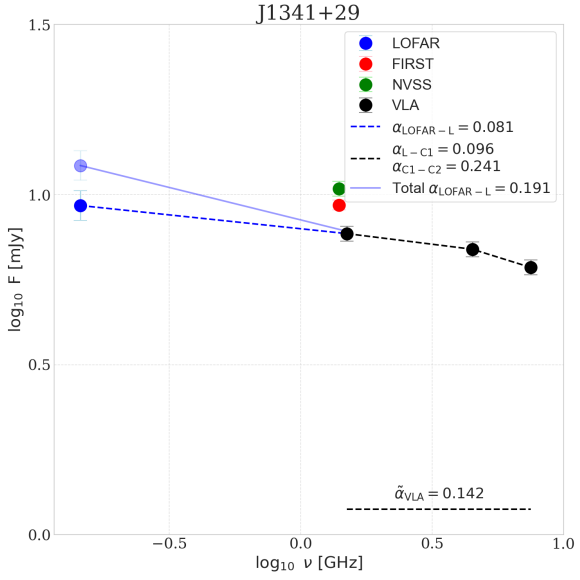
J1341+29
LOFAR
FIRST
NVSS
VLA
$\alpha_{\mathrm{LOFAR-L}} = 0.081$
$\alpha_{\mathrm{L-C1}} = 0.096$
$\alpha_{\mathrm{C1-C2}} = 0.241$
Total $\alpha_{\mathrm{LOFAR-L}} = 0.191$
$\tilde{\alpha}_{\mathrm{VLA}} = 0.142$
$\log_{10}$ F [mJy]
$\log_{10}$ ν [GHz]

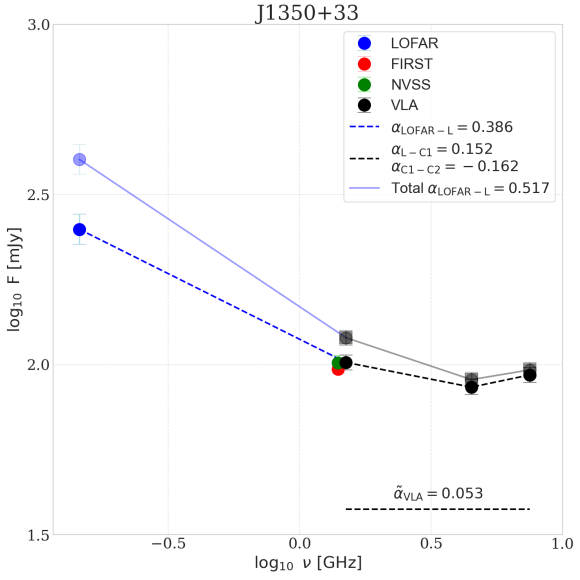
J1350+33
LOFAR
FIRST
NVSS
VLA
$\alpha_{\mathrm{LOFAR-L}} = 0.386$
$\alpha_{\mathrm{L-C1}} = 0.152$
$\alpha_{\mathrm{C1-C2}} = -0.162$
Total $\alpha_{\mathrm{LOFAR-L}} = 0.517$
$\tilde{\alpha}_{\mathrm{VLA}} = 0.053$
$\log_{10}$ F [mJy]
$\log_{10}$ ν [GHz]

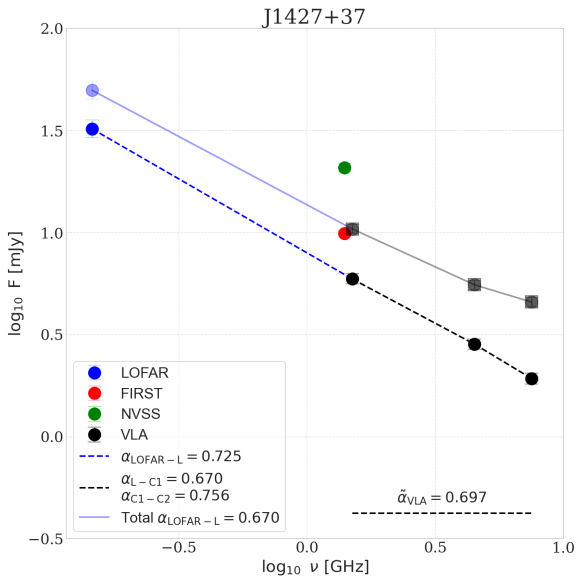
J1427+37
LOFAR
FIRST
NVSS
VLA
$\alpha_{\mathrm{LOFAR-L}} = 0.725$
$\alpha_{\mathrm{L-C1}} = 0.670$
$\alpha_{\mathrm{C1-C2}} = 0.756$
Total $\alpha_{\mathrm{LOFAR-L}} = 0.670$
$\tilde{\alpha}_{\mathrm{VLA}} = 0.697$
$\log_{10}$ F [mJy]
$\log_{10}$ ν [GHz]

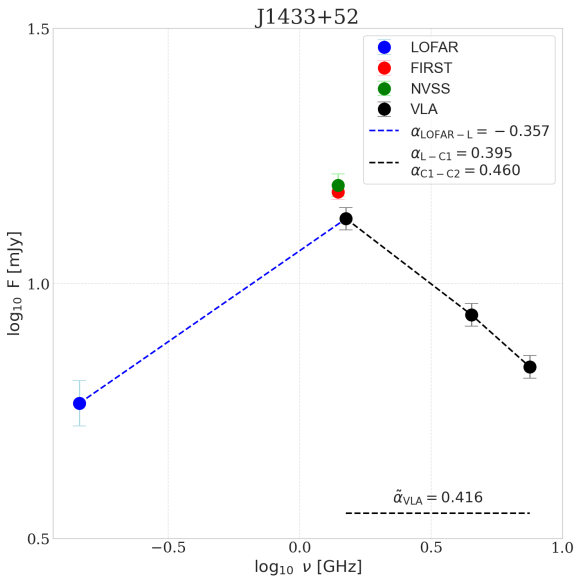
J1433+52
LOFAR
FIRST
NVSS
VLA
$\alpha_{\mathrm{LOFAR-L}} = -0.357$
$\alpha_{\mathrm{L-C1}} = 0.395$
$\alpha_{\mathrm{C1-C2}} = 0.460$
$\tilde{\alpha}_{\mathrm{VLA}} = 0.416$
$\log_{10}$ F [mJy]
$\log_{10}$ ν [GHz]

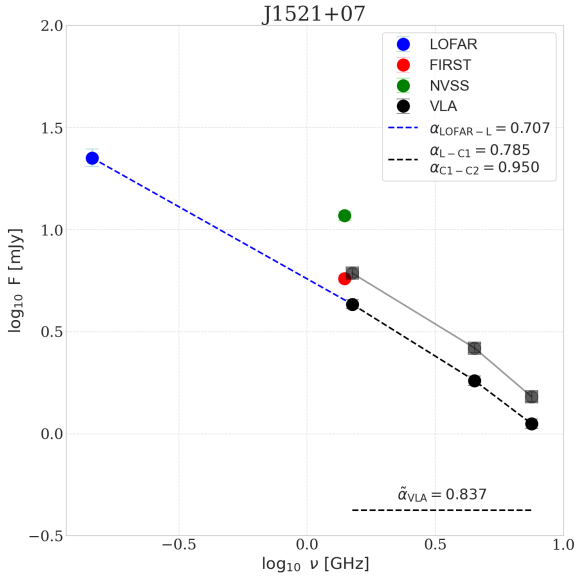
J1521+07
LOFAR
FIRST
NVSS
VLA
$\alpha_{\mathrm{LOFAR-L}} = 0.707$
$\alpha_{\mathrm{L-C1}} = 0.785$
$\alpha_{\mathrm{C1-C2}} = 0.950$
$\tilde{\alpha}_{\mathrm{VLA}} = 0.837$
$\log_{10}$ F [mJy]
$\log_{10}$ ν [GHz]

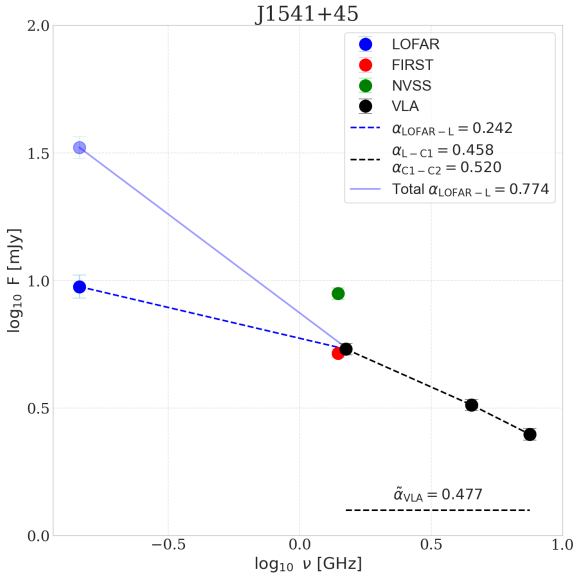
J1541+45
LOFAR
FIRST
NVSS
VLA
$\alpha_{\mathrm{LOFAR-L}} = 0.242$
$\alpha_{\mathrm{L-C1}} = 0.458$
$\alpha_{\mathrm{C1-C2}} = 0.520$
Total $\alpha_{\mathrm{LOFAR-L}} = 0.774$
$\tilde{\alpha}_{\mathrm{VLA}} = 0.477$
$\log_{10}$ F [mJy]
$\log_{10}$ ν [GHz]

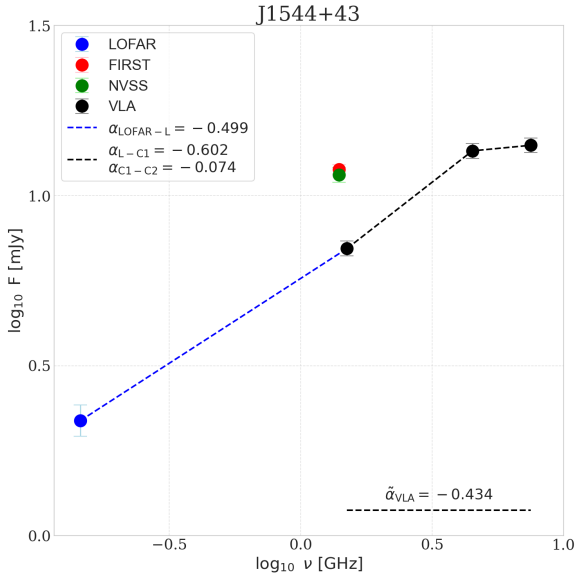
J1544+43
LOFAR
FIRST
NVSS
VLA
$\alpha_{\mathrm{LOFAR-L}} = -0.499$
$\alpha_{\mathrm{L-C1}} = -0.602$
$\alpha_{\mathrm{C1-C2}} = -0.074$
$\tilde{\alpha}_{\mathrm{VLA}} = -0.434$
$\log_{10}$ F [mJy]
$\log_{10}$ ν [GHz]

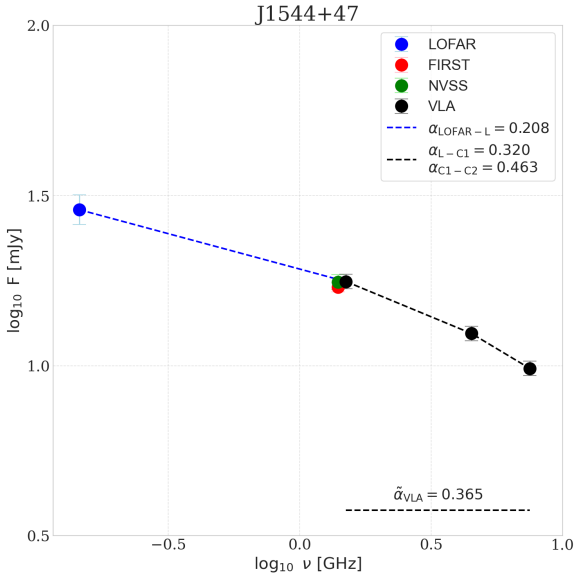
J1544+47
LOFAR
FIRST
NVSS
VLA
$\alpha_{\mathrm{LOFAR-L}} = 0.208$
$\alpha_{\mathrm{L-C1}} = 0.320$
$\alpha_{\mathrm{C1-C2}} = 0.463$
$\tilde{\alpha}_{\mathrm{VLA}} = 0.365$
$\log_{10}$ F [mJy]
$\log_{10}$ ν [GHz]

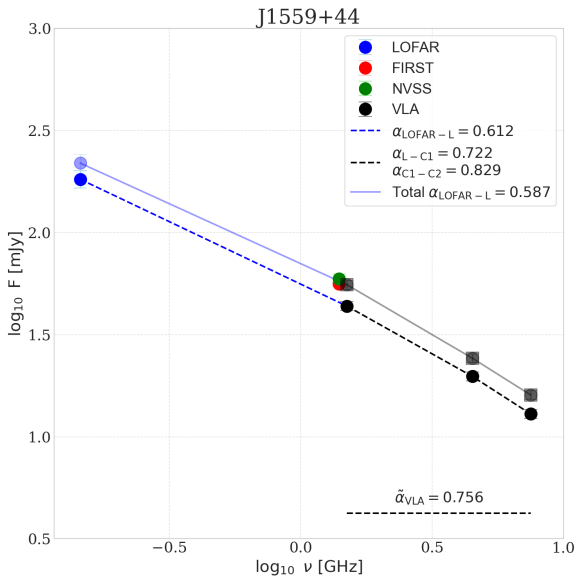
J1559+44
LOFAR
FIRST
NVSS
VLA
$\alpha_{\mathrm{LOFAR-L}} = 0.612$
$\alpha_{\mathrm{L-C1}} = 0.722$
$\alpha_{\mathrm{C1-C2}} = 0.829$
Total $\alpha_{\mathrm{LOFAR-L}} = 0.587$
$\tilde{\alpha}_{\mathrm{VLA}} = 0.756$
$\log_{10}$ F [mJy]
$\log_{10}$ ν [GHz]

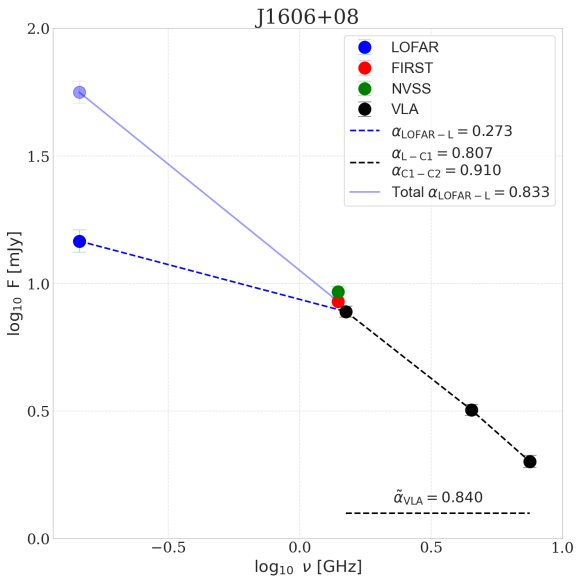
J1606+08
LOFAR
FIRST
NVSS
VLA
$\alpha_{\mathrm{LOFAR-L}} = 0.273$
$\alpha_{\mathrm{L-C1}} = 0.807$
$\alpha_{\mathrm{C1-C2}} = 0.910$
Total $\alpha_{\mathrm{LOFAR-L}} = 0.833$
$\tilde{\alpha}_{\mathrm{VLA}} = 0.840$
$\log_{10}$ F [mJy]
$\log_{10}$ ν [GHz]

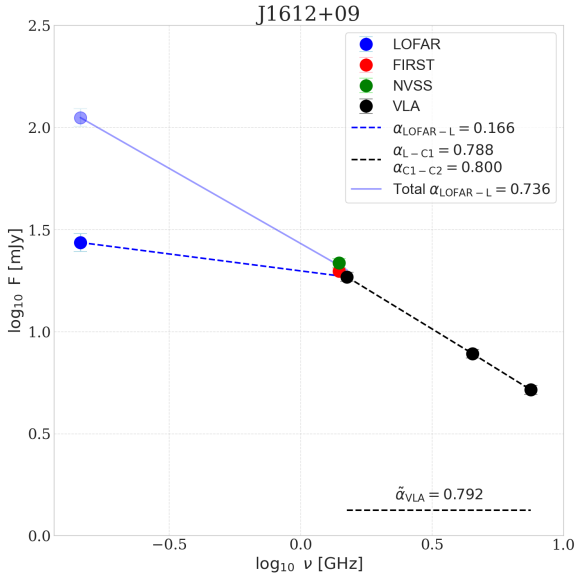
J1612+09
LOFAR
FIRST
NVSS
VLA
$\alpha_{\mathrm{LOFAR-L}} = 0.166$
$\alpha_{\mathrm{L-C1}} = 0.788$
$\alpha_{\mathrm{C1-C2}} = 0.800$
Total $\alpha_{\mathrm{LOFAR-L}} = 0.736$
$\tilde{\alpha}_{\mathrm{VLA}} = 0.792$
$\log_{10}$ F [mJy]
$\log_{10}$ ν [GHz]

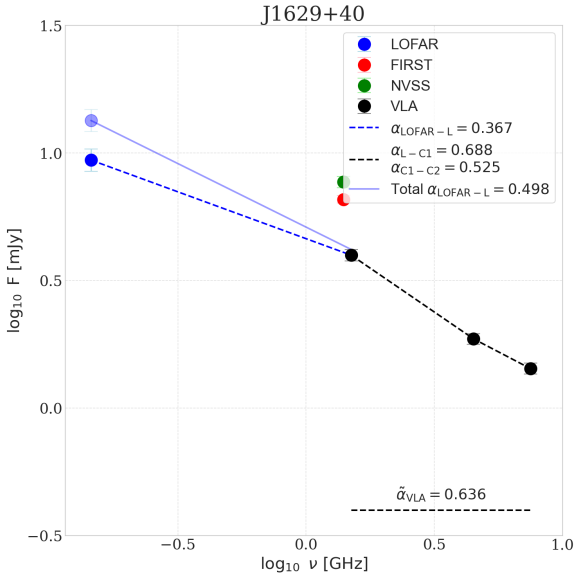
J1629+40
LOFAR
FIRST
NVSS
VLA
$\alpha_{\mathrm{LOFAR-L}} = 0.367$
$\alpha_{\mathrm{L-C1}} = 0.688$
$\alpha_{\mathrm{C1-C2}} = 0.525$
Total $\alpha_{\mathrm{LOFAR-L}} = 0.498$
$\tilde{\alpha}_{\mathrm{VLA}} = 0.636$
$\log_{10}$ F [mJy]
$\log_{10}$ ν [GHz]

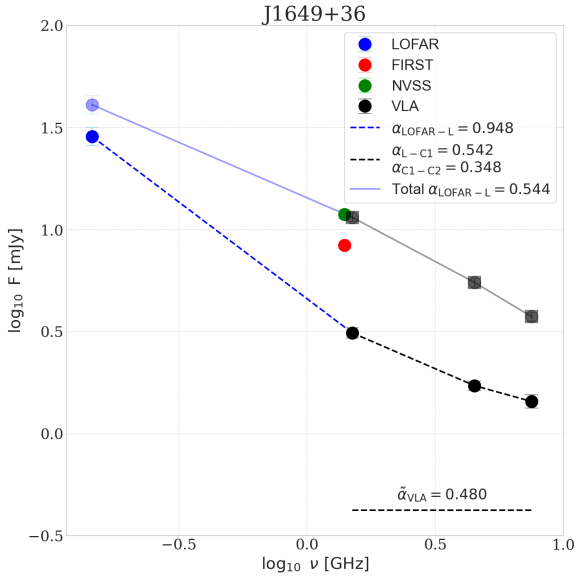
J1649+36
LOFAR
FIRST
NVSS
VLA
$\alpha_{\mathrm{LOFAR-L}} = 0.948$
$\alpha_{\mathrm{L-C1}} = 0.542$
$\alpha_{\mathrm{C1-C2}} = 0.348$
Total $\alpha_{\mathrm{LOFAR-L}} = 0.544$
$\tilde{\alpha}_{\mathrm{VLA}} = 0.480$
$\log_{10}$ F [mJy]
$\log_{10}$ ν [GHz]

Acknowledgements

Quest'ultimo anno di lavoro ha significato molto per me.
Il primo ringraziamento va ovviamente alla mia famiglia, che mi ha sempre supportato nelle mie scelte. Senza di loro, nulla di tutto questo sarebbe stato possibile, e spero che, anche solo in minima parte, questa tesi possa essere un modo per ripagarli.

Il periodo di tirocinio all'INAF di Bologna è stato un'esperienza intensa, fatta di emozioni contrastanti — come spesso accade — ma estremamente formativa. Le competenze acquisite mi hanno regalato piccole grandi soddisfazioni, legate al fatto di riuscire ad avanzare anche in autonomia, potendo sempre contare su solide guide: Ranieri e Marisa. Fin da subito si sono dimostrati eccellenti non solo sul piano professionale, ma anche su quello umano. A loro devo la ritrovata passione per questo campo, in un momento in cui la mia strada sembrava incerta. E anche se il cammino che mi attende sarà probabilmente in salita, avere un obiettivo da raggiungere in cima è sempre meglio che correre senza ostacoli lungo una discesa infinita.

Ringrazio anche le persone che ho conosciuto lungo il percorso universitario qui a Bologna, in particolare Alfonso e Francesco. Siamo molto diversi tra noi, ma uniti dalla stessa passione per l'astronomia.

Un sentito grazie va anche alla professoressa Gitti, che è stata una figura di riferimento importante, sempre disponibile e fondamentale per aiutarmi a fare chiarezza nelle scelte da intraprendere.

Potevo scrivere qualcosa di ancora più elaborato o solenne? Certamente. Lo farò? Assolutamente no. Queste parole esprimono perfettamente il messaggio che voglio lasciare: niente di troppo formale o complicato — dopotutto, stiamo già cercando di capire come funziona l'universo. ;)

Bibliography

P. Alexander and J. P. Leahy. Ageing and speeds in a representative sample of 21 classical double radio sources. , 225:1–26, Mar. 1987. doi: 10.1093/mnras/225.1.1.

H. Alfvén and N. Herlofson. Cosmic Radiation and Radio Stars. *Physical Review*, 78(5): 616–616, June 1950. doi: 10.1103/PhysRev.78.616.

R. Antonucci. Unified models for active galactic nuclei and quasars. , 31:473–521, Jan. 1993. doi: 10.1146/annurev.aa.31.090193.002353.

W. Baade and R. Minkowski. Identification of the Radio Sources in Cassiopeia, Cygnus A, and Puppis A. , 119:206, Jan. 1954. doi: 10.1086/145812.

R. D. Baldi. The nature of compact radio sources: the case of FR 0 radio galaxies. , 31 (1):3, Dec. 2023. doi: 10.1007/s00159-023-00148-3.

R. D. Baldi and A. Capetti. Radio and spectroscopic properties of miniature radio galaxies: revealing the bulk of the radio-loud AGN population. , 508(2):603–614, Dec. 2009. doi: 10.1051/0004-6361/200913021.

R. D. Baldi and A. Capetti. Spectro-photometric properties of the bulk of the radio-loud AGN population. , 519:A48, Sept. 2010. doi: 10.1051/0004-6361/201014446.

R. D. Baldi, A. Capetti, and F. Massaro. FR0CAT: a FIRST catalog of FR 0 radio galaxies. , 609:A1, Jan. 2018. doi: 10.1051/0004-6361/201731333.

R. D. Baldi, A. Capetti, and G. Giovannini. High-resolution VLA observations of FR0 radio galaxies: the properties and nature of compact radio sources. , 482(2):2294–2304, Jan. 2019a. doi: 10.1093/mnras/sty2703.

R. D. Baldi, E. Torresi, G. Migliori, and B. Balmaverde. The High Energy View of FR0 Radio Galaxies. *Galaxies*, 7(3):76, Sept. 2019b. doi: 10.3390/galaxies7030076.

R. D. Baldi, G. Giovannini, and A. Capetti. The eMERLIN and EVN View of FR 0 Radio Galaxies. *Galaxies*, 9(4):106, Nov. 2021. doi: 10.3390/galaxies9040106.

R. D. Baldi, G. Giovannini, A. Capetti, and R. Lico. Jet properties of FR0 radio galaxies: need for VLBI data. In E. Ros, P. Benke, S. A. Dzib, I. Rottmann, and J. A. Zensus, editors, *Proceedings of the 16th EVN Symposium*, pages 43–46, Sept. 2024.

B. Balmaverde and A. Capetti. The host galaxy/AGN connection in nearby early-type galaxies. Is there a miniature radio-galaxy in every "core" galaxy? , 447(1):97–112, Feb. 2006. doi: 10.1051/0004-6361:20054031.

R. H. Becker, R. L. White, and D. J. Helfand. The FIRST Survey: Faint Images of the Radio Sky at Twenty Centimeters. , 450:559, Sept. 1995. doi: 10.1086/176166.

V. Beckmann and C. R. Shrader. *Active Galactic Nuclei*. 2012.

A. S. Bennett. The revised 3C catalogue of radio sources. , 68:163, Jan. 1962a.

A. S. Bennett. The revised 3C catalogue of radio sources. , 68:163, Jan. 1962b.

P. N. Best and T. M. Heckman. On the fundamental dichotomy in the local radio-AGN population: accretion, evolution and host galaxy properties. , 421(2):1569–1582, Apr. 2012. doi: 10.1111/j.1365-2966.2012.20414.x.

P. N. Best, G. Kauffmann, T. M. Heckman, J. Brinchmann, S. Charlot, Ž. Ivezić, and S. D. M. White. The host galaxies of radio-loud active galactic nuclei: mass dependences, gas cooling and active galactic nuclei feedback. , 362(1):25–40, Sept. 2005. doi: 10.1111/j.1365-2966.2005.09192.x.

R. D. Blandford and A. Königl. Relativistic jets as compact radio sources. , 232:34–48, Aug. 1979. doi: 10.1086/157262.

R. D. Blandford and D. G. Payne. Hydromagnetic flows from accretion disks and the production of radio jets. , 199:883–903, June 1982. doi: 10.1093/mnras/199.4.883.

R. D. Blandford and M. J. Rees. A "twin-exhaust" model for double radio sources. , 169:395–415, Dec. 1974. doi: 10.1093/mnras/169.3.395.

R. D. Blandford and R. L. Znajek. Electromagnetic extraction of energy from Kerr black holes. , 179:433–456, May 1977. doi: 10.1093/mnras/179.3.433.

J. G. Bolton, G. J. Stanley, and O. B. Slee. Nature, 164, 101. *Nature*, 164:101–102, 1949.

J. G. Bolton, F. F. Gardner, and M. B. Mackey. The Parkes catalogue of radio sources, declination zone -20° to -60°. *Australian Journal of Physics*, 17:340, Sept. 1964. doi: 10.1071/PH640340.

M. Brienza, R. Morganti, J. Harwood, T. Duchet, K. Rajpurohit, A. Shulevski, M. J. Hardcastle, V. Mahatma, L. E. H. Godfrey, I. Prandoni, T. W. Shimwell, and H. Intema. Radio spectral properties and jet duty cycle in the restarted radio galaxy 3C388. , 638:A29, June 2020. doi: 10.1051/0004-6361/202037457.

Brienza, M., Godfrey, L., Morganti, R., Vilchez, N., Maddox, N., Murgia, M., Orru, E., Shulevski, A., Best, P. N., Brüggen, M., Harwood, J. J., Jamrozy, M., Jarvis, M. J., Mahony, E. K., McKean, J., and Röttgering, H. J. A. Lofar discovery of a 700-kpc remnant radio galaxy at low redshift. *AA*, 585:A29, 2016. doi: 10.1051/0004-6361/201526754. URL https://doi.org/10.1051/0004-6361/201526754.

J. O. Burns, E. D. Feigelson, and E. J. Schreier. The inner radio structure of Centaurus A : clues to the origin of thejet X-ray emission. , 273:128–153, Oct. 1983. doi: 10.1086/161353.

A. Capetti, F. Massaro, and R. D. Baldi. FRIICAT: A FIRST catalog of FR II radio galaxies. , 601:A81, May 2017a. doi: 10.1051/0004-6361/201630247.

A. Capetti, F. Massaro, and R. D. Baldi. FRICAT: A FIRST catalog of FR I radio galaxies. , 598:A49, Feb. 2017b. doi: 10.1051/0004-6361/201629287.

A. Capetti, M. Brienza, R. D. Baldi, G. Giovannini, R. Morganti, M. J. Hardcastle, H. J. A. Rottgering, G. F. Brunetti, P. N. Best, and G. Miley. The LOFAR view of FR 0 radio galaxies. , 642:A107, Oct. 2020a. doi: 10.1051/0004-6361/202038671.

A. Capetti, F. Massaro, and R. D. Baldi. Large-scale environment of FR 0 radio galaxies. , 633:A161, Jan. 2020b. doi: 10.1051/0004-6361/201935962.

Capetti, A., Baldi, R. D., Brienza, M., Morganti, R., and Giovannini, G. The low-frequency properties of fr 0 radio galaxies. *AA*, 631:A176, 2019. doi: 10.1051/0004-6361/201936254. URL https://doi.org/10.1051/0004-6361/201936254.

Capetti, A., Brienza, M., Balmaverde, B., Best, P. N., Baldi, R. D., Drabent, A., Gürkan, G., Rottgering, H. J. A., Tasse, C., and Webster, B. The lofar view of giant, early-type galaxies: Radio emission from active nuclei and star formation. *AA*, 660:A93, 2022. doi: 10.1051/0004-6361/202142911. URL https://doi.org/10.1051/0004-6361/202142911.

B. W. Carroll and D. A. Ostlie. *An introduction to modern astrophysics*. Cambridge University Press, 2017.

CASA Team, B. Bean, S. Bhatnagar, S. Castro, J. Donovan Meyer, B. Emonts, E. Garcia, Garwood, et al. CASA, the Common Astronomy Software Applications for Radio Astronomy. , 134(1041):114501, Nov. 2022. doi: 10.1088/1538-3873/ac9642.

Y. Chen, Q. Gu, J. Fan, H. Zhou, Y. Yuan, W. Gu, Q. Wu, D. Xiong, X. Guo, N. Ding, and X. Yu. The Powers of Relativistic Jets Depend on the Spin of Accreting Supermassive Black Holes. , 913(2):93, June 2021. doi: 10.3847/1538-4357/abf4ff.

X. Cheng, T. An, B. W. Sohn, X. Hong, and A. Wang. Parsec-scale properties of eight fanaroff-riley type 0 radio galaxies. *MNRAS*, 506(2):1609–1623, Sept. 2021. doi: 10.1093/mnras/stab1383.

X. P. Cheng and T. An. Parsec-scale Radio Structure of 14 Fanaroff-Riley Type 0 Radio Galaxies. , 863(2):155, Aug. 2018. doi: 10.3847/1538-4357/aad22c.

L. Ciotti, J. P. Ostriker, and D. Proga. Feedback from Central Black Holes in Elliptical Galaxies. I. Models with Either Radiative or Mechanical Feedback but not Both. , 699 (1):89–104, July 2009. doi: 10.1088/0004-637X/699/1/89.

L. Ciotti, J. P. Ostriker, and D. Proga. Feedback from Central Black Holes in Elliptical Galaxies. III. Models with Both Radiative and Mechanical Feedback. , 717(2):708–723, July 2010. doi: 10.1088/0004-637X/717/2/708.

G. Colla, C. Fanti, R. Fanti, I. Gioia, C. Lari, J. Lequeux, R. Lucas, and M. H. Ulrich. Radio and optical data on a complete sample of radio faint galaxies. , 20:1–36, Apr. 1975.

J. J. Condon and S. M. Ransom. *Essential Radio Astronomy*. 2016.

J. J. Condon, W. D. Cotton, E. W. Greisen, Q. F. Yin, R. A. Perley, G. B. Taylor, and J. J. Broderick. The NRAO VLA Sky Survey. , 115(5):1693–1716, May 1998. doi: 10.1086/300337.

D. R. DeBoer, R. G. Gough, J. D. Bunton, T. J. Cornwell, R. J. Beresford, S. Johnston, I. J. Feain, A. E. Schinckel, Jackson, et al. Australian SKA Pathfinder: A High-Dynamic Range Wide-Field of View Survey Telescope. *IEEE Proceedings*, 97(8):1507–1521, Aug. 2009. doi: 10.1109/JPROC.2009.2016516.

V. A. Dombrovsky. On the nature of the radiation from the crab nebula. In *Dokl. Akad. Nauk. SSSR*, volume 94, page 1021, 1954.

S. M. Faber, S. Tremaine, E. A. Ajhar, Y.-I. Byun, A. Dressler, K. Gebhardt, C. Grillmair, J. Kormendy, T. R. Lauer, and D. Richstone. The Centers of Early-Type Galaxies with HST. IV. Central Parameter Relations. , 114:1771, Nov. 1997. doi: 10.1086/118606.

A. C. Fabian. Observational Evidence of Active Galactic Nuclei Feedback. , 50:455–489, Sept. 2012. doi: 10.1146/annurev-astro-081811-125521.

B. L. Fanaroff and J. M. Riley. The morphology of extragalactic radio sources of high and low luminosity. , 167:31P–36P, May 1974. doi: 10.1093/mnras/167.1.31P.

C. Fanti. Radio telescope antennas: from single dish to multielement interferometer. In *Proceedings of the First MCCT-SKADS Training School*, page 1, Jan. 2007. doi: 10.22323/1.059.0001. Licensed under CC BY-NC-SA 1.0, see https://creativecommons.org/licenses/by-nc-sa/1.0/. A more recent version (CC BY-NC-SA 4.0) is available at https://creativecommons.org/licenses/by-nc-sa/4.0/.

C. Fanti and R. Fanti. Una finestra sull'universo" invisibile". *Lezioni di radioastronomia*, 2012.

L. Ferrarese and D. Merritt. A Fundamental Relation between Supermassive Black Holes and Their Host Galaxies. , 539(1):L9–L12, Aug. 2000. doi: 10.1086/312838.

D. Garofalo, D. A. Evans, and R. M. Sambruna. The evolution of radio-loud active galactic nuclei as a function of black hole spin. , 406(2):975–986, Aug. 2010. doi: 10.1111/j.1365-2966.2010.16797.x.

K. Gebhardt, R. Bender, G. Bower, A. Dressler, S. M. Faber, A. V. Filippenko, R. Green, C. Grillmair, L. C. Ho, J. Kormendy, T. R. Lauer, J. Magorrian, J. Pinkney, D. Richstone, and S. Tremaine. A Relationship between Nuclear Black Hole Mass and Galaxy Velocity Dispersion. , 539(1):L13–L16, Aug. 2000. doi: 10.1086/312840.

G. Ghisellini. Extragalactic relativistic jets. In F. A. Aharonian, W. Hofmann, and F. M. Rieger, editors, *25th Texas Symposium on Relativistic AstroPhysics (Texas 2010)*, volume 1381 of *American Institute of Physics Conference Series*, pages 180–198. AIP, Sept. 2011. doi: 10.1063/1.3635832.

G. Ghisellini, F. Tavecchio, and M. Chiaberge. Structured jets in TeV BL Lac objects and radiogalaxies. Implications for the observed properties. , 432(2):401–410, Mar. 2005. doi: 10.1051/0004-6361:20041404.

G. Giovannini, R. D. Baldi, A. Capetti, M. Giroletti, and R. Lico. Jets in FR0 radio galaxies. , 672:A104, Apr. 2023. doi: 10.1051/0004-6361/202245395.

P. Grandi, A. Capetti, and R. D. Baldi. Discovery of a Fanaroff-Riley type 0 radio galaxy emitting at γ-ray energies. , 457(1):2–8, Mar. 2016. doi: 10.1093/mnras/stv2846.

P. Grandi, E. Torresi, D. Macconi, B. Boccardi, and A. Capetti. Jet-Accretion System in the Nearby mJy Radio Galaxies. , 911(1):17, Apr. 2021. doi: 10.3847/1538-4357/abe776.

T. Grandsaert. Master thesis, division of synchrotron radiation. Department of Physics, Lund University, Jan. 2021. Supervisors: Andrey Shavorskiy, Hamed Tarawneh, Sverker Werin.

M. J. Hardcastle, G. Gürkan, R. J. van Weeren, W. L. Williams, P. N. Best, F. de Gasperin, D. A. Rafferty, S. C. Read, J. Sabater, Shimwell, et al. LOFAR/H-ATLAS: a deep low-frequency survey of the Herschel-ATLAS North Galactic Pole field. , 462 (2):1910–1936, Oct. 2016. doi: 10.1093/mnras/stw1763.

T. M. Heckman and P. N. Best. The Coevolution of Galaxies and Supermassive Black Holes: Insights from Surveys of the Contemporary Universe. , 52:589–660, Aug. 2014. doi: 10.1146/annurev-astro-081913-035722.

T. M. Heckman, G. Kauffmann, J. Brinchmann, S. Charlot, C. Tremonti, and S. D. M. White. Present-Day Growth of Black Holes and Bulges: The Sloan Digital Sky Survey Perspective. , 613(1):109–118, Sept. 2004. doi: 10.1086/422872.

L. C. Ho. Nuclear activity in nearby galaxies. , 46:475–539, Sept. 2008. doi: 10.1146/annurev.astro.45.051806.110546.

J. A. Högbom. Aperture Synthesis with a Non-Regular Distribution of Interferometer Baselines. , 15:417, June 1974.

A. W. Hotan, J. D. Bunton, A. P. Chippendale, M. Whiting, J. Tuthill, V. A. Moss, D. McConnell, S. W. Amy, M. T. Huynh, Allison, et al. Australian square kilometre array pathfinder: I. system description. , 38:e009, Mar. 2021. doi: 10.1017/pasa.2021.1.

Z. Igo and A. Merloni. The global energetics of radio AGN kinetic feedback in the local Universe. , 697:A196, May 2025. doi: 10.1051/0004-6361/202452888.

John McKean. Modern interferometers. Presentation at ERIS 2015 Workshop, 2015. URL https://www.eso.org/sci/meetings/2015/eris2015/L3_ModernInterferometers.pdf. Accessed: 2025-02-12.

K. I. Kellermann, R. Sramek, M. Schmidt, D. B. Shaffer, and R. Green. VLA Observations of Objects in the Palomar Bright Quasar Survey. , 98:1195, Oct. 1989. doi: 10.1086/115207.

E. Y. Khachikian and D. W. Weedman. An atlas of Seyfert galaxies. , 192:581–589, Sept. 1974. doi: 10.1086/153093.

J. Kormendy and L. C. Ho. Coevolution (Or Not) of Supermassive Black Holes and Host Galaxies. , 51(1):511–653, Aug. 2013. doi: 10.1146/annurev-astro-082708-101811.

D. Kozieł-Wierzbowska, N. Vale Asari, G. Stasińska, M. Sikora, E. I. Goettems, and A. Wójtowicz. What Distinguishes the Host Galaxies of Radio-loud and Radio-quiet AGNs? , 846(1):42, Sept. 2017. doi: 10.3847/1538-4357/aa8326.

S. Laha, C. Ricci, J. C. Mather, E. Behar, L. Gallo, F. Marin, R. Mbarek, and A. Hankla. X-ray properties of coronal emission in radio quiet active galactic nuclei. *Frontiers in Astronomy and Space Sciences*, 11:1530392, Mar. 2025. doi: 10.3389/fspas.2024.1530392.

R. Laing, C. Jenkins, J. Wall, S. Unger, G. Bicknell, M. Dopita, and P. Quinn. Asp conf. ser. vol. 54, the physics of active galaxies. 1994.

R. A. Laing and A. H. Bridle. Systematic properties of decelerating relativistic jets in low-luminosity radio galaxies. , 437(4):3405–3441, Feb. 2014. doi: 10.1093/mnras/stt2138.

M. Magliocchetti. Hosts and environments: a (large-scale) radio history of agn and star-forming galaxies. *The Astronomy and Astrophysics Review*, 30(1):6, 2022.

J. Magorrian, S. Tremaine, D. Richstone, R. Bender, G. Bower, A. Dressler, S. M. Faber, K. Gebhardt, R. Green, C. Grillmair, Kormendy, et al. The Demography of Massive Dark Objects in Galaxy Centers. , 115(6):2285–2305, June 1998. doi: 10.1086/300353.

A. P. Marscher. Multiband Impressions of Active Galactic Nuclei. , 76:168, Jan. 2005.

F. Massaro, N. Álvarez-Crespo, A. Capetti, R. D. Baldi, I. Pillitteri, R. Campana, and A. Paggi. Deciphering the Large-scale Environment of Radio Galaxies in the Local Universe: Where Are They Born? Where Do They Grow? Where Do They Die? , 240(2):20, Feb. 2019. doi: 10.3847/1538-4365/aaf1c7.

D. McConnell, C. L. Hale, E. Lenc, J. K. Banfield, G. Heald, A. W. Hotan, J. K. Leung, Moss, et al. The Rapid ASKAP Continuum Survey I: Design and first results. , 37:e048, Nov. 2020a. doi: 10.1017/pasa.2020.41.

D. McConnell, C. L. Hale, E. Lenc, J. K. Banfield, G. Heald, A. W. Hotan, J. K. Leung, V. A. Moss, T. Murphy, O'Brien, et al. The Rapid ASKAP Continuum Survey I: Design and first results. , 37:e048, Nov. 2020b. doi: 10.1017/pasa.2020.41.

S. N. X. Medina, J. S. Urquhart, S. A. Dzib, A. Brunthaler, B. Cotton, K. M. Menten, F. Wyrowski, H. Beuther, S. J. Billington, C. Carrasco-Gonzalez, T. Csengeri, Y. Gong, Hofner, and others. GLOSTAR: Radio Source Catalog I. 28° ¡ ℓ ¡ 36° and —b— ¡ 1°. , 627:A175, July 2019. doi: 10.1051/0004-6361/201935249.

A. Mikhailov and Y. Sotnikova. The relationship between FR0 radio galaxies and gigahertz-peaked spectrum sources. *Astronomische Nachrichten*, 342(1130):1130–1134, Nov. 2021. doi: 10.1002/asna.20210050.

H. Miraghaei and P. N. Best. The nuclear properties and extended morphologies of powerful radio galaxies: the roles of host galaxy and environment. , 466(4):4346–4363, Apr. 2017. doi: 10.1093/mnras/stx007.

Moldón, J., Deller, A. T., Wucknitz, O., Jackson, N., Drabent, A., Carozzi, T., Conway, J., Kapińska, A. D., McKean, J. P., Morabito, L., et al. The lofar long baseline snapshot calibrator survey. *AA*, 574:A73, 2015. doi: 10.1051/0004-6361/201425042. URL https://doi.org/10.1051/0004-6361/201425042.

NASA Science. Massive black holes dwell in most galaxies, according to hubble census, 2022. URL https://science.nasa.gov/missions/hubble/massive-black-holes-dwell-in-most-galaxies-according-to-hubble-census/.

National Radio Astronomy Observatory (NRAO). Images and Data from the NRAO. URL https://public.nrao.edu/. Images and information from the NRAO website.

R. P. Norris, A. M. Hopkins, J. Afonso, S. Brown, J. J. Condon, L. Dunne, I. Feain, R. Hollow, Jarvis, et al. EMU: Evolutionary Map of the Universe. , 28(3):215–248, Aug. 2011. doi: 10.1071/AS11021.

C. P. O'Dea and D. J. Saikia. Compact steep-spectrum and peaked-spectrum radio sources. , 29(1):3, Dec. 2021. doi: 10.1007/s00159-021-00131-w.

C. P. O'Dea, S. A. Baum, and C. Stanghellini. What Are the Gigahertz Peaked-Spectrum Radio Sources? , 380:66, Oct. 1991. doi: 10.1086/170562.

P. Padovani. The faint radio sky: radio astronomy becomes mainstream. , 24(1):13, Sept. 2016. doi: 10.1007/s00159-016-0098-6.

P. Padovani, D. M. Alexander, R. J. Assef, B. De Marco, P. Giommi, R. C. Hickox, G. T. Richards, V. Smolčić, E. Hatziminaoglou, V. Mainieri, and M. Salvato. Active galactic nuclei: what's in a name? , 25(1):2, Aug. 2017. doi: 10.1007/s00159-017-0102-9.

V. S. Paliya. A New Gamma-Ray-emitting Population of FR0 Radio Galaxies. , 918(2): L39, Sept. 2021. doi: 10.3847/2041-8213/ac2143.

R. A. Perley and B. J. Butler. An Accurate Flux Density Scale from 50 MHz to 50 GHz. , 230(1):7, May 2017. doi: 10.3847/1538-4365/aa6df9.

R. A. Perley, C. J. Chandler, B. J. Butler, and J. M. Wrobel. The Expanded Very Large Array: A New Telescope for New Science. , 739(1):L1, Sept. 2011. doi: 10.1088/2041-8205/739/1/L1.

P. O. Petrucci, F. Ursini, A. De Rosa, S. Bianchi, M. Cappi, G. Matt, M. Dadina, and J. Malzac. Testing warm Comptonization models for the origin of the soft X-ray excess in AGNs. , 611:A59, Mar. 2018. doi: 10.1051/0004-6361/201731580.

Planck Collaboration, N. Aghanim, Y. Akrami, M. Ashdown, J. Aumont, C. Baccigalupi, M. Ballardini, A. J. Banday, et al. Planck 2018 results. VI. Cosmological parameters. , 641:A6, Sept. 2020. doi: 10.1051/0004-6361/201833910.

I. Raginski and A. Laor. AGN coronal emission models - I. The predicted radio emission. , 459(2):2082–2096, June 2016. doi: 10.1093/mnras/stw772.

A. Rubén. Do sensors "outresolve" lenses' capabilities? *Research Gate*, 06 2009.

M. Schmidt. 3C 273 : A Star-Like Object with Large Red-Shift. , 197(4872):1040, Mar. 1963. doi: 10.1038/1971040a0.

C. K. Seyfert. Nuclear Emission in Spiral Nebulae. , 97:28, Jan. 1943. doi: 10.1086/144488.

N. I. Shakura and R. A. Sunyaev. Black holes in binary systems. Observational appearance. , 24:337–355, Jan. 1973.

Shimwell, T. W., Tasse, C., Hardcastle, M. J., Mechev, A. P., Williams, W. L., Best, P. N., Röttgering, H. J. A., Callingham, J. R., et al. The lofar two-metre sky survey - ii. first data release. *AA*, 622:A1, 2019. doi: 10.1051/0004-6361/201833559. URL https://doi.org/10.1051/0004-6361/201833559.

Shimwell, T. W., Hardcastle, M. J., Tasse, C., Best, P. N., Röttgering, H. J. A., Williams, W. L., Botteon, A., Drabent, A., Mechev, A., Shulevski, A., et al. The lofar two-metre sky survey - v. second data release. *AA*, 659:A1, 2022. doi: 10.1051/0004-6361/202142484. URL https://doi.org/10.1051/0004-6361/202142484.

M.-S. Shin, J. P. Ostriker, and L. Ciotti. Environmental Effects on the Growth of Supermassive Black Holes and Active Galactic Nucleus Feedback. , 745(1):13, Jan. 2012. doi: 10.1088/0004-637X/745/1/13.

O. B. Slee, A. L. Roy, M. Murgia, H. Andernach, and M. Ehle. Four Extreme Relic Radio Sources in Clusters of Galaxies. , 122(3):1172–1193, Sept. 2001. doi: 10.1086/322105.

E. Torresi, P. Grandi, A. Capetti, R. D. Baldi, and G. Giovannini. X-ray study of a sample of FR0 radio galaxies: unveiling the nature of the central engine. , 476(4): 5535–5547, June 2018. doi: 10.1093/mnras/sty520.

S. Tremaine, K. Gebhardt, R. Bender, G. Bower, A. Dressler, S. M. Faber, Filippenko, et al. The Slope of the Black Hole Mass versus Velocity Dispersion Correlation. , 574 (2):740–753, Aug. 2002. doi: 10.1086/341002.

F. Ubertosi, M. Gitti, E. Torresi, F. Brighenti, and P. Grandi. The central FR0 in the sloshing cluster Abell 795: Indications of mechanical feedback from Chandra data. *Astronomische Nachrichten*, 342(1207):1207–1211, Nov. 2021. doi: 10.1002/asna.20210055.

C. M. Urry and P. Padovani. Unified Schemes for Radio-Loud Active Galactic Nuclei. , 107:803, Sept. 1995. doi: 10.1086/133630.

M. P. van Haarlem, M. W. Wise, A. W. Gunst, G. Heald, J. P. McKean, J. W. T. Hessels, A. G. de Bruyn, R. Nijboer, Swinbank, et al. LOFAR: The LOw-Frequency ARray. , 556:A2, Aug. 2013. doi: 10.1051/0004-6361/201220873.

M. Vashakidze. On the degree of polarization of the radiation of nearby extragalactic nebulae and of the crab nebula. *Astr. Cir*, 147(11), 1954.

J. V. Wall and J. A. Peacock. Bright extragalactic radio sources at 2.7 GHz- III. The all-sky catalogue. , 216:173–192, Sept. 1985. doi: 10.1093/mnras/216.2.173.

R. L. White, R. H. Becker, D. J. Helfand, and M. D. Gregg. The first survey: Faint images of the radio sky at twenty-centimeters, 1994. URL https://sundog.stsci.edu/.

R. L. White, R. H. Becker, D. J. Helfand, and M. D. Gregg. A Catalog of 1.4 GHz Radio Sources from the FIRST Survey. , 475(2):479–493, Feb. 1997. doi: 10.1086/303564.

L. Woltjer. Emission Nuclei in Galaxies. , 130:38, July 1959. doi: 10.1086/146694.